Università degli Studi di Padova

Dipartimento di Fisica e Astronomia
Corso di Laurea in Fisica

Development of the Infrared Quantum Counter concept for low-threshold particle detection

Laureando:
Federico Chiossi

Relatore:
Ch.mo Prof. A. F. Borghesani

Anno accademico 2015/2016

Contents

List of Figures

List of abbreviation

CT	Charge Transfer
cw	continuos wave
ESA	Excited State Absorption
IRQC	Infrared Quantum Counter
LDR	Laser Double Resonance
LY	Light Yield
RE	Rare-earth
UP	Upconversion

Introduction

The interest in the development of devices for the detection of low rate, low energy deposition events is motivated by the axionic dark matter searches and by the study of coherent neutrino-nucleous scattering as well as by the possibility to decrease the energy threshold for soft X-ray detection. An investigation on the feasibility of a new class of low-threshold, high efficiency particle detectors is carried out within the Axioma Project at the Laboratori Nazionali INFN in Legnaro.

The detection process is mainly based on the Infrared Quantum Counter concept (IRQC) applied to rare-earth (RE) doped crystals, as proposed by the Nobel prize Bloembergen in 1959. An energetic particle excites the rare-earth ions from the ground state to a low-lying ($< 1 <$eV), metastable (lifetime $\geq 1\,$ms) state. Then, a tuned pump laser promotes the excited ions to a higher lever (upconversion), that relaxes to the ground state or to some other lower lying states by emitting a visible fluorescence photon. A very high detection efficiency can be reached depending on several factors, including the energy level scheme of the specific combination of RE ion and crystal matrix that may lead to excitation recycling induced light amplification processes.

The most important requirement is that the energy deposition released by an energetic particle in the crystal leads to a high production of excited ions in the lowest metastable level above the ground state. A second important requirement is a high upconversion efficiency that depends on the laser light absorption cross section and lifetime of the excited levels of the ions. Finally, a third requirement is that the crystal is as transparent as possible to the laser if the ions are in the ground state.

Owing to the scant number of studies on these subjects that can be found in literature, the best crystal-RE ion combination has to be sought by direct investigation in our lab. To this goal we have started a systematic investigation campaign of the properties of several combinations of single crystal hosts doped with different RE ions of selected concentrations.

The first chapter deals with the unique optical properties of RE doped crystals that make them a suitable active medium for the realization of the detector. Starting from RE electronic configuration, it is shown how to calculate the energy, lifetime and transition probability of the RE levels. It is also discussed the RE ions interaction with the environment, such as vibrational coupling, and with themselves via processes of energy transfer. In particular, a very careful study of light absorption processes is presented because if is of crucial importance for our purposes, as well as the application of RE in inorganic scintillator and in the IRQC technique.

In the second chapter it is proposed a model in order to simulate and estimate the main detection features such as the number of photon released per energy unit of the particle or ionizing radiation (LY), the detector time response, and its noise features.

We have built two experimental setups in order to investigate the different properties of the crystals. The third chapter discusses the measurement carried out with the first setup whereas the measurements performed with the second one are reported in the fourth chapter.

The efficiency of the production of excited ion levels is studied by exciting crystals by either electron impact or X-rays irradiation with a home-made electron gun. The emission spectrum can be recorded in the range $200\,\mathrm{nm} < \lambda < 5000\,\mathrm{nm}$ by suitably merging the spectra recorded with different spectrometers, including a FT-IR (Fourier Transform-InfraRed) one. The outcome of these measurements is the light yield in both the visible and infrared ranges. In particular, light yields as high as 5×10^4 photons/MeV can be obtained. From the spectra we are also able to identify the levels involved in the excitation by both the position of the emitted wavelengths and by their time evolution. We have also excited the crystals with different lasers (diode, tunable dye and Ti:Sa laser, Nd:YAG higher harmonics) in order to shed light on possible different excitation mechanisms with respect to particle excitation. At the end of the third chapter it is proved how the laser excitation can improve the scintillation due to electron impact even if the high noise must be reduced in order to realize a viable detector.

For these reasons, a second type of measurements has been carried out in order to study upconversion efficiency and crystal transparency by irradiating the crystals with finely tunable lasers at low temperature. The upconversion efficiency is measured by simulating the particle excitation with an infrared source of selected wavelength band and using a Ti:Sa or a dye laser tunable with picometer accuracy to promote the excited ions to the even higher excited levels whose decay produces the visible fluorescence light collected by a photomultiplier. In the future we will also use a small γ-source in order to detect its crystal excitation by applying the IRQC technique.

All these studies allow us to define the optimum characteristics of the crystal-dopant system to select the optimum crystal for low-threshold particle detection.

Chapter 1

Theoretical Background on Rare Earths

Rare earths (RE), as defined by IUPAC, are a series of chemical elements ranging in atomic number from Lanthanum (Z=57) to Lutetium (Z=71). They are named Lantanoids or Lantanides. Scandium (Z=21) and Yttrium (Z=39) are also counted to them. They are widely used in modern technology for their unique magnetic and optical properties due to their particular electronic configuration. The similarity of their electronic structure, $[\mathrm{Xe}]4f^n6s^2$ or $[\mathrm{Xe}]4f^n5d6s^2$ ($[\mathrm{Xe}] = 1s^22s^22p^63s^23p^63d^{10}4s^24p^64d^{10}5s^25p^6$), give the neutral Lantanides analogous electrochemical properties. Actually, starting from Lantanium (Z=57), as the atomic number increases, the additional electrons fill the inner $4f$ subshell whereby preserving the same number of valence electrons. For this reason, rare earths atoms in compounds are interchangeable, provided the limitation imposed by the lattice tolerance with respect to the atomic radius of different atoms is enforced. Since all Lantanides may have an oxidation number as large as 3+, they can usually dope matrices in form of a trivalen ion, $[\mathrm{Xe}]4f^n$.

The wavefunctions of the $4f$ electrons are shielded and compressed by the outer and less localized $5s^2 - 5d^6$ shells. As a consequence, they are weakly coupled to their surrounding. For example, the luminescence spectra are generally dominated by sharp zero-phonon lines. However, many important processes, such as multiphonon processes or interaction between RE ions, still occur. Although Actinides have similar properties, this work is devoted only to Lantanides and, in particular, to their optical properties. Actually, Actinides are characterized by the filling of $5f$ subshell but, in contrast to the localized Lantanides $4f$ shell, they can get strongly hybridized in compounds.

1.1. Energy levels of trivalent Rare Earth ions

This section is devoted to coarsely describe the energy level structure of RE^{3+} ions in solids by considering the several occurring interactions. A detailed theoretical approach to the precise calculation of the energy levels can be found in literature [1–3].

Since the $4f$ electrons of RE^{3+} ions are weakly coupled to the environment and their polarization effect can be neglected to first order, the free-ion model is a quite good approximation in order to calculated the $4f$ energy levels. The electronic closed shells can be considered spherically symmetric so it can be proved that they have no effect on the relative energy levels of $4f$ electrons. In other words, the effect of the electrons of the [Xe] configuration appears in the free Hamiltonian only as a term that shields the nucleus. Hence, the free-ion Hamiltonian takes only in account the n electrons in the $4f$ states.

The most relevant contributions to the Hamiltonian for a RE^{3+} ion with nuclear charge Ze in absence of an external field may be written as[1]

$$\begin{aligned} H_{\text{free}} &= H_0 + H_{\text{e}-\text{e}} + H_{\text{SO}} = \\ &= \left[-\frac{\hbar^2}{2m_e}\sum_{i=1}^{n}\nabla_i - \frac{1}{4\pi\epsilon_0}\sum_{i=1}^{n}\frac{Z^*e}{r_i}\right] + \frac{1}{4\pi\epsilon_0}\sum_{i,i<j}\frac{e^2}{r_{ij}} + \sum_{i=1}^{n}\frac{1}{2m^2c^2r_i}\frac{d\mathrm{U}(r_i)}{dr_i}(\mathbf{s}_i\cdot\mathbf{l}_i) \end{aligned} \tag{1.1}$$

where e, m_e, n are the charge, the mass and the number of the $4f$ electrons, respectively. Z^*e is an effective nuclear charge that takes into account the shielding of the closed shells. r_i, $\mathbf{s}_i$ and $\mathbf{l}_i$ are the radial coordinate, the spin, and the orbital angular momentum of the i-th electron, respectively. $r_{ij} = |r_i - r_j|$ is the position of the i-th electron relative to the j-th one. $\mathrm{U}(r_i)$ is the potential in which the ith-electron is moving. The first term H_0 is the sum of the kinetic and potential energies of the electrons in the field of the nucleus, the second $H_{\text{e}-\text{e}}$ describes the mutual repulsive Coulomb interaction between each electron pair, and the third H_{SO} is the energy associated with spin-orbit interactions.

The H_0 term has a spherical symmetry and separates in energy the different configurations ($4f$,$5d$...) by $\approx 10^5\ \text{cm}^{-1}$ but it does not remove its degenerancy.

Let us neglect, for a while, the spin-orbit term. It is not possible to calculate exact solutions for the Hamiltonian $H = H_0 + H_{\text{e}-\text{e}}$, when more than one electron is involved. However, good approximations can be obtained with the well-known Hartree-Fock method [4]. The term $H_{\text{e}-\text{e}}$ can be divided into: a spherically symmetric component $H_{\text{e}-\text{e}}^{\text{SS}}$, that added to H_0 is known as Hamiltonian of central field, and into a second component $H_{\text{e}-\text{e}}^{\text{NSS}}$ that is small enough to be treated as a perturbation. In the central field approximation, each electron experiences an average radial potential due to the interaction with other electrons and with the nucleus, but it moves independently of the coordinates of the other electrons. Likewise in the Hydrogen atom, the exact solution of the Schrodinger equation for one electron can be expressed as product of three components, characterized by four quantum numbers n, l, m_l, m_s

$$\Psi = \frac{1}{r}R_{nl}(r)Y_{lm_l}(\theta,\phi)\sigma(m_s) \tag{1.2}$$

where (r,θ,ϕ) are the spherical coordinates. The radial function R_{nl} depends on the central field potential, Y_{lm_l} are the spherical harmonic functions and $\sigma(m_s)$ takes in account the electron spin. Linear combinations of these solutions that satisfy the Pauli exclusion

---

[1] Assuming that the nuclear mass is infinite.

principle and provide an eigenfunction set for a N electrons system, are obtained by using Slater determinants.

The Hamiltonian $H = H_0 + H_{\mathrm{e-e}}$ commutes with the total spin angular momentum ($\mathbf{S}$), the total orbital angular momentum ($\mathbf{L}$), the total angular momentum ($\mathbf{J}$) and its projection on z-axis (J_z). The relative quantum numbers S, L, J, M are considered good quantum numbers. This situation is known as LS-coupling o Russel-Saunders coupling: the spin and orbital angular momenta of each electron are independent and the total angular momentum $\mathbf{J}$ is the sum of the total orbital angular momentum $\mathbf{L} = \sum \mathbf{l}_i$ and total spin angular momentum $\mathbf{S} = \sum \mathbf{s}_i$. A basis set of electronic states for a system described by the hamiltonian $H_0 + H_{\mathrm{e-e}}$ can be expressed as

$$\Psi = |nl\gamma\mathrm{LSJM}\rangle \tag{1.3}$$

where nl for RE^{3+} are the principal and azimuthal quantum numbers, respectively, that are associated with the radial part of the wavefunction. The quantum number γ, called seniority number, is required to distinguish among states with the same LSJM numbers.

The terms with the same nl and different LS numbers are separated in energy by about $10^4\,\mathrm{cm}^{-1}$. Another common notation for Eq. (1.3) is $(nl)\ ^{2\mathrm{S}+1}\mathrm{L}(\gamma)_{\mathrm{JM}}$. This basis is applied to calculate the matrix elements of additional perturbation terms, such as the electron-electron Coulomb interaction and even the spin-orbit interaction [1]. Actually, in RE, they are comparable in magnitude and cannot be both neglected. Contrary to J and M, L and S are not good quantum numbers for the spin-orbit term. Hence, the $|nl\gamma\mathrm{LSJM}\rangle$ wavefunctions are not eigenfunctions of the free Hamiltonian in Eq. (1.1). The eigenfunctions that can diagonalize the spin-orbit and the electron-electron Hamiltonian terms are expressed as a linear combinations of pure LS-coupling wavefunctions $|nl\gamma\mathrm{LSJM}\rangle$ with the same JM numbers

$$|nl\gamma[\mathrm{LS}]\mathrm{JM}\rangle = \sum_{\alpha,\mathrm{L},\mathrm{S}} a_{\alpha LS}\,|nl\alpha\mathrm{LSJM}\rangle \tag{1.4}$$

The new wavefunctions, as they have been constructed, are a complete set of eigenfunctions for H_0 and also for the Hamiltonian in Eq. (1.1). This basis, calculated in the so-called "intermediate coupling", is normally written with the predominant pure Russell-Saunders state $(4f)\ ^{2\mathrm{S}+1}\mathrm{L}(\gamma)_{\mathrm{JM}}$ or with $|(4f)\gamma[\mathrm{LS}]\mathrm{JM}\rangle$ where LS in the square parenthesis indicate the quantum numbers of the predominant pure Russell-Saunders state. The problem is now how to find the coefficients $a_{\alpha LS}$, that are determinated by the matrix elements [2]:

$$a_{\alpha\mathrm{LS}} = \sum_{\gamma,\mathrm{L},\mathrm{S}} \langle nl\alpha\mathrm{LSJM}|H_{\mathrm{e-e}} + H_{\mathrm{SO}}|nl\gamma[\mathrm{LS}]\mathrm{JM}\rangle \tag{1.5}$$

In general, the more energetic are the $4f$ levels to be described, the more relevant are the contributions in Eq. (1.4) of other levels with the same J. Since the $5d$-levels components are very small, it is common practice to neglect them in the sum and write then the basis by implying only the numbers $nl = 4f$. The free-ion Hamiltonian Eq. (1.1) is independent of M, so each $|nl\gamma[\mathrm{LS}]\mathrm{JM}\rangle$ eigenfunction is $(2\mathrm{J}+1)$ times degenerate.

An efficient way to simplify the computation required to solve Eq. (1.5) is to represent the $H_{\mathrm{e-e}}$ and H_{SO} operators in tensorial form. By so doing, five effective tensorial operators are needed. Each of them is coupled with a parameter, that is adjusted to give agreement with the experimentally measured energy levels, that estimate the integral of the radial component of the Slater determinants that depends on the central field potential.

According to the Wigner-Eckart theorem, Eq. (1.5) can be replaced by the sum of expectation values of reduced matrix element properly weighed by the Clebsch-Gordan coefficients. In this way, it is possible to obtain the eigenfunctions and the relative energies of the free-ion Hamiltonian in Eq. (1.1). Nevertheless, in order to find a good agreement with the experimental values we must take into account second order corrections, such as relativistic effects and configurational interactions. Additionally, the Hamiltonian must account for more interactions, including spin-spin, spin-other-orbit, and, for $4f^n$ configurations with $n > 2$ also electron triplet interactions and, even, electrostatically correlated magnetic interactions.

By including fifteen more tensor operators, needed to described these interactions, with fifteen more parameters, for a total of twenty parameters to be experimentally determined, it is possible to calculate the $a_{\alpha\mathrm{LS}}$ coefficients with a good accuracy [2, 3]. For example, the ground state of Pr^{3+} ($^3\mathrm{H}_4, |[51]4\mathrm{M}\rangle$) can be expressed as [5]:

$$|[51]4\mathrm{M}\rangle = 0.9879\,|^3\mathrm{H}_4\rangle + 0.1523\,|^1\mathrm{G}_4\rangle - 0.0282\,|^3\mathrm{F}_4\rangle + ... \tag{1.6}$$

where the terms in the r.h.s belong to the Russel-Saunders basis given by Eq. (1.3). The deviation between measured and calculated values of the energy could be less than few cm^{-1}. The spin-orbit interaction removes the degeneracy of the states with same $nl\gamma[\mathrm{LS}]$ numbers bur with different J, separating them by $\approx 10^3\,\mathrm{cm}^{-1}$ [1].

Upon doping a dielectric crystal with a RE ion, the ion spherical symmetry is broken and the energy levels split by $\approx 10^2\,\mathrm{cm}^{-1}$ under the influence of the strong crystalline electric field according to the crystal group symmetry. The difference between the energies of the same RE ion level in different host matrices is of the same order of magnitude or less. As a consequence of the shielding due to the $5s^2$ and $5p^6$ electrons, the crystal-field term in the Hamiltonian can be regarded as a perturbation of the free ion Hamiltonian and can also be calculated introducing several more tensor operators and adjustable parameters.

Although the energy levels are mixed even with respect to the quantum number J, the Russell-Saunders notation ($^{2\mathrm{S}+1}\mathrm{L}_{\mathrm{JM}}$, $|4f\gamma[\mathrm{LS}]\mathrm{JM}\rangle$), is being normally used, thereby indicating the dominant components described by the four quantum numbers LSJM. The more than twenty parameters related to the tensor operators can be estimated by measuring several $4f^n$ level energies. This is possible by studying the absorption of narrow linewidth tunable lasers or the emission spectrum with high resolution.

It has been proved by Kramers [6] that each level of a RE ion with an odd number of electrons in the 4f shell, i.e., with semi-integer J value, retains at least a double degeneracy under the action of the crystal- or of any other electric field in such a way that the multiplets split in, at least, (J + 1/2) sublevels. This degeneracy, however, can be removed by applying an external magnetic field. In Fig. (1.1) the energy levels upon $50\,000\,\mathrm{cm}^{-1}$ calculated by Carnall [7] for different RE^{3+} doped LaF_3 are shown.

Recently, the complete $4f^n$ level energies of RE^{3+}:LaF_3 have been calculated, thereby obtaining values up to $200\,000\,\mathrm{cm}^{-1}$ [8].

Lantanium and Lutetium do not show any transition between $4f$ states because they have the $4f$ shell completely empty and full, respectevely. For this reason, they are not represented in the figure. However, they are exploited in the composition of host matrix [9] because they are spectroscopically inert, as are Sc and Y.

We have considered only trivalent RE, but this discussion is correct even for divalent RE. The additional electron in $4f$ shell in the divalent ions compared to the trivalent RE ones causes an enlargement of the atomic radius that reduces the energy separation between the $4f$ and $5d$ levels, as one can see in Fig. (1.6) on page 30.

Thanks to their narrow lines, it is possible to observe even the hyperfine interactions. As an example, we consider the Zeeman effect in presence of an externally applied magnetic field. If the field is directed along $\hat{z}$ direction with strength B_z, a Zeeman term has to be added to the Hamiltonian in the form

$$H_{\mathrm{mag}} = \frac{\mu_B}{\hbar} B_z [L_z + g_s S_z] \tag{1.7}$$

Here, μ_B is the Bohr magneton and $g_s \approx 2$. In the case of a weak magnetic field field this term can be considered as a perturbation and the energy splitting in LS-coupling can be expressed as:

$$\langle nl\gamma\mathrm{LSJM}|\, H_{mag}\, |nl\gamma\mathrm{LSJM}\rangle = \mu_B B_z \mathrm{M} g(\mathrm{SLJ}) \tag{1.8}$$

where $g(\mathrm{SLJ})$ is the so-called Landé factor

$$g(\mathrm{SLJ}) = 1 + (g_s - 1)\frac{\mathrm{J}(\mathrm{J}+1) - \mathrm{L}(\mathrm{L}+1) + \mathrm{S}(\mathrm{S}+1)}{2\mathrm{J}(\mathrm{J}+1)} \tag{1.9}$$

In the case of RE^{3+}, the eigenfunctions cannot well described by a unique set of quantum numbers SL. Thus, the Landè factor has to be weighted by the square modulus of the relative component in the basis of SL-coupling:

$$\begin{aligned}\langle\gamma[\mathrm{LS}]\mathrm{JM}|\, H_{\mathrm{mag}}\, |\gamma[\mathrm{LS}]\mathrm{JM}\rangle &= \sum_{\alpha,\mathrm{S},\mathrm{L}} |\, \langle\gamma[\mathrm{LS}]\mathrm{JM}|\alpha\mathrm{LSJM}\rangle\, |^2\, \langle\alpha\mathrm{LSJM}|\, H_{\mathrm{mag}}\, |\alpha\mathrm{LSJM}\rangle \\ &= \mu_B B_z \mathrm{M} \sum_{\alpha,\mathrm{S},\mathrm{L}} |\, \langle\gamma[\mathrm{LS}]\mathrm{JM}|\alpha\mathrm{LSJM}\rangle\, |^2 g(\mathrm{SLJ}) \qquad (1.10)\end{aligned}$$

All remaining hyperfine and superhyperfine interactions are not important in this work and can be neglected. In Fig. (1.2) the contributions of the different terms in the Hamiltonian

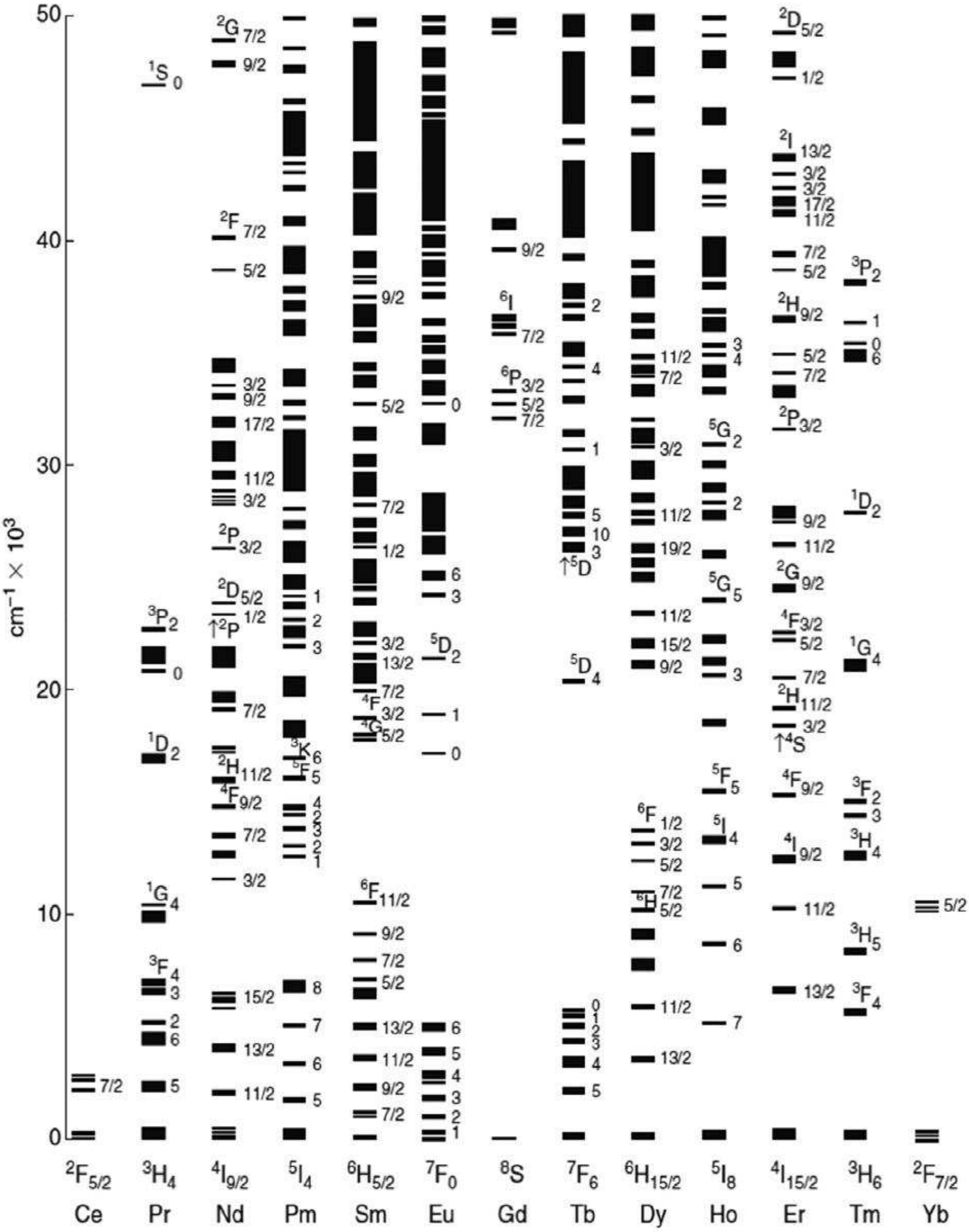

Figure 1.1: Energy level structure of RE^{+3}:LaF_3 calculated by Carnall [7].

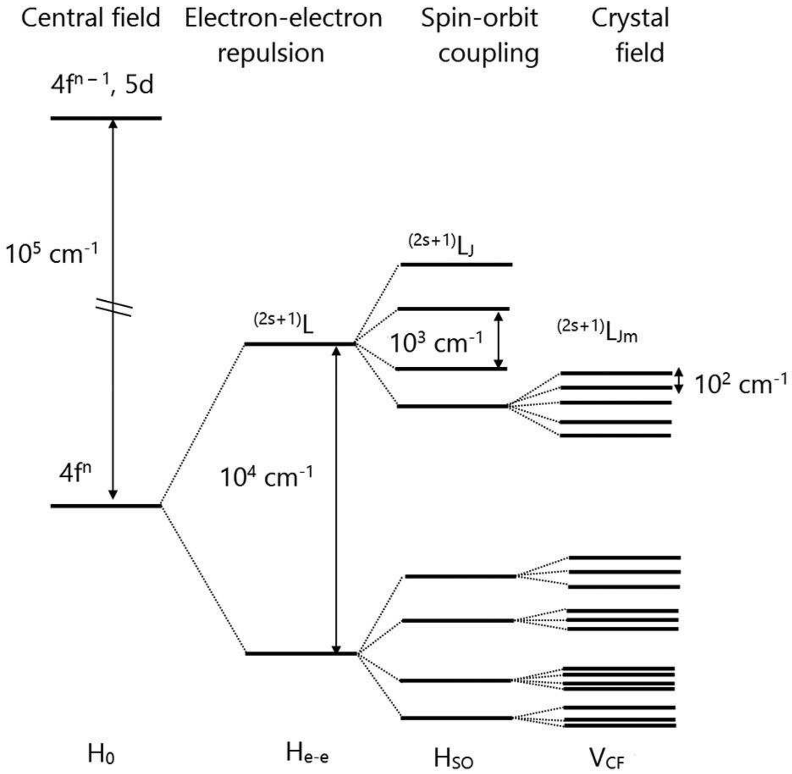

Figure 1.2: Scheme of the energy levels splitting due to the different types of interactions. [9].

to the energy level splitting is summarized.

The influence of crystal-field and, more generally, the coupling with the crystal environment, is much stronger for the $5d$ energy levels than for the $4f$ ones. As a consequence, the crystal field interaction cannot be treated as a perturbation term and the previuos estimations can be applied only to $4f^n$ levels. In spite of this, from experimentally estimated parameters by Dorenbos [10] it is possible to predict the $5d$ energy levels for the twelve Lantanides in hundreds of different host materials with an accuracy of $\pm 600\,\mathrm{cm}^{-1}$.

1.2. Line broadening and vibronic side bands

The several factors that determine the linewidth and the line profile of absorption and fluorescence of optically active centers can be divided into two types: homogeneous and inhomogeneous. The former broadens the line of each atom in the same way and the line profile is generally close to a Lorentzian function, whereas the latter distributes the resonance frequencies of the atom over a given band and the line profile is close to a Gaussian function [2, 11].

Highly disordered crystalline structure can be an important inhomogeneous factor, especially at low temperature: each rare earth ion experiences a quite different local environment which influences the energy of the ion level. As a consequence, inhomogeneous linewidth as large as $100\,\mathrm{cm}^{-1}$ may be occur. For the same reason, the narrowest lines have been observed in ultrapure RE doped single-crystals at extremely low dopant concentration.

Whereas the linewidth due to the natural radiative lifetimes is almost always negligible, the vibrational coupling is the most important cause of homogeneous broadening of absorption and emission lines in the spectrum of many systems, even in $4f$-$4f$ transition in RE^{3+} doped crystals in spite of the weakness of electron-phonon coupling. McCumber and Sturge [12] have theoretically shown that line width Γ and shift δE of a transition can be expressed as a function of the temperature T as:

$$\Gamma(T) = \Gamma(0) + \alpha_1 \left(\frac{T}{T_D}\right)^7 \int_0^{T/T_D} \frac{x^6 e^x}{(e^x - 1)^2} dx \tag{1.11}$$

$$\delta E = \alpha_2 \left(\frac{T}{T_D}\right)^4 \int_0^{T/T_D} \frac{x^3}{e^x - 1} dx \tag{1.12}$$

where T_D is the Debye temperature. The temperature independent term $\Gamma(0)$ arises from inhomogeneous line broadening. α_1, α_2 are constants that are related to the electron-phonon coupling.

The lattice vibrational coupling, even if its effects on the line broadening can be strongly reduced by cooling the system according to Eq. (1.11), deserves a more detailed discussion for its role in important processes like side-band absorption and non-radiative relaxation.

Small ion deviations from the equilibrium position in the lattice are associated to an energy well described to a first approximation by a harmonic oscillator model. It is known that the energy level are given by $(m + \frac{1}{2})\hbar\omega$ where m is the vibrational quantum numbers and ω is the angular frequency of vibration. Each ion electronic transition may even involve different vibronic state and the resulting spectrum exhibits several corresponding lines. The relative intensity of these transitions is given by the Franck-Condon factor $F_w^v = |\int \Psi_v^* \Psi_w \, \mathrm{d}Q|^2$[2], where w and v are the vibrational numbers of the initial and the final vibrational states Ψ_w and Ψ_v, respectevely, and Q is the coordinate of the nucleus relative to the lattice.

It is possible to find an analytical form for the Franck-Condon factor. In the approximation that the transition takes place only from the vibrational ground state $w = 0$, it can be expressed as [13]:

$$F_v^0 = e^{-S} \frac{S^v}{v!} \tag{1.13}$$

where S is the dimensionless Huang-Rhys parameter. Eq. (1.13) describes F_v^0 as a Poisson distribution with variable v and expectance value S. A number of phonons equal to S is also released on average in the electronic transitions. A microscopic point of view can be given by referring to the Fig. (1.5) on page 30. Let E_t be the energy difference between the ground state and the excited state of the atom in the equilibrium position. When the atom is excited, the different electronic configuration leads a displacement ΔQ of its nucleus in

---

[2] Actually, the Franck-Condon factor is dependent also by the fourth power of the transition energy. Because in this case the different transition are little separated in energy, this dependence is neglected.

relation to its previous position in the lattice. The maximum peak of the absorption spectrum ia observed at the energy[3]

$$E_a = E_t + \frac{1}{2}M\omega^2(\Delta Q)^2 \tag{1.14}$$

where the second term in r.h.s corrisponds to the displacement energy. M and ω are the reduced mass and the frequency of the vibration of the system, respectively. S is defined as the number of phonons that can be created with this displacement energy [14]

$$S = \frac{1}{\hbar\omega}\frac{1}{2}M\omega^2(\Delta Q)^2 \tag{1.15}$$

The photon emitted in the radiative relaxation of the atom has an energy less than E_t because, after the electron transition that occurs slower than the lattice relaxation, the atom is in a non-equilibrium position with an averaged energy equal to $\frac{1}{2}M\omega^2(\Delta Q)^2$. Then an average number of S phonons are released[4]. The maximum peak of the emission spectrum is observed at the energy:

$$E_e = E_t - \frac{1}{2}M\omega^2(\Delta Q)^2 \tag{1.16}$$

The difference $E_a - E_e$ called Stokes shift, can be expressed as[5]

$$\Delta E_{\text{Stokes}} = E_{\text{a}} - E_{\text{e}} \approx 2(\frac{1}{2}M\omega^2(\Delta Q)^2) - 2(\frac{1}{2}\hbar\omega) = 2(S-1)\hbar\omega \tag{1.17}$$

In this way, the Huang-Rhys parameter can be experimentally estimated[6], linking the theoretical calculation to the experimental value.

It should be noted that the Huang-Rhys parameter, as it is a measure of the electron-phonon coupling strength, can be different for different ion excited states. Actually, in RE^{3+} S lies in the range $10^{-2} \leq S \leq 10^{-1}$ for the lowest $4f$ levels whereas $S \approx 1$ for the $5d$ levels.

The Huang-Rhys parameter can also be experimentally estimated. In the case of the $4f$-$4f$ transitions, both the absorption and the emission spectrum are also dominated by narrow zero-phonon line[7],[8].

---

[3] The Poisson distribution takes on its maximum value for $w = S$.

[4] We have assumed that frequency and reduced mass for the vibronic system relative to the two states are the same, but it is not always a good approximation.

[5] Recalling that the zero point energy is $\hbar\omega/2$.

[6] Actually, Eq. (1.17) is an approximation. Other researchers use $\Delta E_{\text{Stokes}} = 2S\hbar\omega$. This ambiguity is explained in [13] and is solved by assuming for S low accuracy.

[7] Almost zero phonons are averaged involved.

[8] There may still be a relevant Stokes shift, but it is due to the splitting of the Stark levels in the manifolds.

1.3. Relaxation processes

Typically, three different mechanisms determine the lifetimes and the kinetics of the level population of the excited states of the ions. These are radiative relaxation, multi-phonon relaxation, and interaction between rare earth ions.

1.3.1 Radiative relaxation

Radiative transitions between $4f$ levels are characterized by long lifetimes, up to some tens of milliseconds. The lifetimes are so long because the electric-dipole transition between pure $4f$ levels is parity-forbidden whereas only the small $5d$ contribution to the wavefunction or the coupling with the lattice vibrations give origin to a non-zero transition probability. This kind of transitions is usually referred to as forced (or, induced) electric dipole transitions. In addition, also magnetic-dipole have to be taken into account that are typically about 10^5 less probable than the allowed electric-dipole transitions[9].

The theory developed by Judd [16] and Ofelt [17] allows the researchers to calculate the transition probabilities from three parameters Ω_t ($t = 2,4,6$) that are commonly determined in an empirical way. According to this theory, the electric dipole (ED) line strength involving the initial multiplet $|4f^n\gamma[\mathrm{SL}]\mathrm{J}\rangle$[10] and the final one $|4f^n\gamma[\mathrm{S'L'}]\mathrm{J'}\rangle$ can be expressed as follows:

$$S^{\mathrm{ED}} = \sum_t \Omega_t |\, \langle 4f^n\gamma[\mathrm{SL}]\mathrm{J}|\, \mathbf{U}^t \,|4f^n\gamma[\mathrm{S'L'}]\mathrm{J'}\rangle \,|^2 \qquad (t = 2,4,6) \tag{1.18}$$

where $\mathbf{U}^t$ is a tensor operator of rank t related to the dipole moment operator. A similar expression can be written for the magnetic dipole (MD) transition:

$$S^{\mathrm{MD}} = \left(\frac{\hbar}{2mc}\right)^2 \left|\langle 4f^n\gamma[\mathrm{SL}]\mathrm{J}|\, \mathbf{L} + 2\mathbf{S} \,|4f^n\gamma[\mathrm{S'L'}]\mathrm{J'}\rangle\right|^2 \tag{1.19}$$

In addition, the integrated cross section σ_{abs} of this transition can be theoretically demostrated to be related to S^{ED} and $^{\mathrm{MD}}$ by:

$$\int \sigma_{\mathrm{abs}} \frac{d\lambda}{\lambda} = \frac{4\pi^2 e^2}{3\hbar c} \frac{1}{(2\mathrm{J}+1)} \left[\frac{(n^2+2)^2}{9n} S^{\mathrm{ED}} + n S^{\mathrm{MD}}\right] \tag{1.20}$$

where $(2\mathrm{J}+1)$ is the degeneracy of the initial manifold and n the refractive index. S^{ED} can be alsoevaluated once the term S^{MD} is calculated with Eq. (1.19) and then subtracted.

By fitting the theoretical S^{ED} value computed by means of Eq. (1.18) to the experimentally determined one given by Eq. (1.20) for, at least, three transitions, the Judd-Ofelt

---

[9] Some transitions follow the selection rules of the electric quadrupole Tab. (1.1) but as they are too strong relative to the weak quadrupole transition, they are called pseudo-quadrupole transitions but are not considered here. More detail are given elsewhere [15].

[10] In this theory the splitting due to crystal field is neglected. The quantum number M is also omitted in this notation.

parameters can be obtained in such a way that all other electric dipole strengths can be computed.

The radiative transition rate for spontaneous emission involving electric and magnetic dipole interactions between the $|4f^n\gamma[\mathrm{SL}]\mathrm{J}\rangle$ and $|4f^n\gamma[\mathrm{S'L'}]\mathrm{J'}\rangle$ manifolds (indicated by LSJ and (LSJ)′ quantum numbers) is given by

$$A^{\mathrm{LSJ}}_{(\mathrm{LSJ})'} = \frac{32\pi^3 e^2}{3\hbar c} \cdot \frac{n^2 c}{\lambda^3(2\mathrm{J}+1)} \left[\frac{(n^2+2)^2}{9n} S^{\mathrm{ED}} + n S^{\mathrm{MD}} \right] \tag{1.21}$$

The radiative lifetime $\tau^{\mathrm{rad}}_{\mathrm{LSJ}}$ of upper level and its branching ratio $\beta^{\mathrm{LSJ}}_{(\mathrm{LSJ})'}$, i.e the probability of the manifold LSJ to radiatively relax to the (LSJ)′ one, follow straightforward

$$\frac{1}{\tau^{rad}_{\mathrm{LSJ}}} = \sum_{(\mathrm{LSJ})'} A^{\mathrm{LSJ}}_{(\mathrm{LSJ})'} \qquad \beta^{\mathrm{LSJ}}_{(\mathrm{LSJ})'} = \frac{A^{\mathrm{LSJ}}_{(\mathrm{LSJ})'}}{\sum_{(\mathrm{LSJ})''} A^{\mathrm{LSJ}}_{(\mathrm{LSJ})''}} \tag{1.22}$$

The selection rules for forced electric dipole transitions, derived by the Judd-Ofelt theory, are reported in Tab. (1.1). However, there are many cases, in which they are not satisfied.

In case the crystal is birefringent, the situation is more complicated but, for our purposes, it suffices to know that the absorption cross section depends on the light polarization and the lifetime of the excited states depends on the crystal-dipole moment orientation.

The emission cross section between LSJ and (LSJ)′ can be estimated from the measured emission spectrum $I(\lambda)$ by using the Fűchtbauer-Ladenburg equation [15, 18], known also as $\beta - \tau$ method:

$$\sigma^{\mathrm{LSJ}}_{(\mathrm{LSJ})'}(\lambda) = \frac{\lambda^5 \beta^{\mathrm{LSJ}}_{(\mathrm{LSJ})'} I(\lambda)}{8\pi c n^2 \tau^{\mathrm{rad}}_{\mathrm{LSJ}} \int^{\mathrm{LSJ}}_{(\mathrm{LSJ})'} I(\lambda)\lambda\, \mathrm{d}\lambda} \tag{1.23}$$

where the integral is limited to the wavelegth range of the emission due to the transition from LSJ to (LSJ)′. The branching ratio $\beta^{\mathrm{LSJ}}_{(\mathrm{LSJ})'}$ is experimentally estimated by

$$\beta^{\mathrm{LSJ}}_{(\mathrm{LSJ})'} = \frac{\int^{\mathrm{LSJ}}_{(\mathrm{LSJ})'} I(\lambda)\lambda\, \mathrm{d}\lambda}{\sum_{(\mathrm{LSJ})''} \int^{\mathrm{LSJ}}_{(\mathrm{LSJ})''} I(\lambda)\lambda\, \mathrm{d}\lambda} \tag{1.24}$$

Table 1.1: Selection rules of different electric and magnetic transitions [9]

Forced electric dipole	**Magnetic dipole**	**Electric quadrupole**
$\Delta l = \pm 1$	$\Delta l = 0$	$\Delta l = 0, \pm 2$
$\Delta S = 0$	$\Delta S = 0, \pm 1$	$\Delta S = 0$
$\lvert\Delta L\rvert \leq 6$	$\Delta L = 0, \pm 1$	$\lvert\Delta L\rvert \leq 2$
$\lvert\Delta J\rvert \leq 6$ if J and $\mathrm{J}' \neq 0$	$\Delta J = 0, \pm 1$	$\lvert\Delta J\rvert \leq 2$
$\lvert\Delta J\rvert = 2, 4, 6$ if J or $\mathrm{J}' = 0$		
$\pi_f = -\pi_i$	$\pi_f = \pi_i$	$\pi_f = \pi_i$

1.3.2 Multiphonon relaxation

Although the electrons in the $4f$ shell are shielded by those in the $5s$ and $5d$ shells, intra-ionic processes can frequently occur. The most common of them is the non-radiative decay of the excited RE ions due to the emission of phonons. The larger is the energy gap between the populated excited state and the next lower lying energy level, the more phonons are needed to bridge the gap and the smaller is the multi-phonon decay rate W^{MP}. In Tab. (1.2) the maximum phonon energies of some common crystals are reported. In particular, the non-radiative decay is described in this system by the so called "energy gap law"

$$W^{\mathrm{MP}} = C\exp(-\alpha_{\mathrm{nr}}\Delta E)[1-\exp(-\hbar\omega_{\mathrm{eff}}/kT)]^{-p} \tag{1.25}$$

where C and the Stokes parameter α_{nr} relative to the excited state are empirically fitted parameters. $\hbar\omega_{\mathrm{eff}}$ is the effective phonon energy of the host medium, ΔE is the energy gap and $p = \Delta E/\hbar\omega_{\mathrm{eff}}$ is the number of phonons involved in the process. This equation can be rewritten as [20]

$$W^{\mathrm{MP}} = C\exp(-\alpha_{\mathrm{nr}}\Delta E)\,[n(T)+1]^{p} \tag{1.26}$$

in which

$$n(T) = [\exp(\hbar\omega_{\mathrm{eff}}/kT)-1]^{-1} \tag{1.27}$$

It is possible to prove a relation between α_{nr} and the Huang-Rhys parameter [21]:

$$\alpha_{nr} = (\hbar\omega_{\mathrm{eff}})^{-1}\left[\left(1-\frac{2}{p}\right)\ln\frac{p}{S_0} - 1 - \ln(n+1)\right] \tag{1.28}$$

The multiphonon relaxation takes the ions to the next lower lying manifold with a rate

Table 1.2: Properties of various host crystals [19]

Host	$\hbar\omega_{\mathbf{max}}$ $[cm^{-1}]$	**Trasparency** $[\mu m]$	**Hygroscopic**	**Structure**
YVO (YVO_4)	880-980	0.35-4.8	no	tetragonal
YAG ($Y_3Al_5O_{12}$)	700-850	0.21-5.2	no	cubic
YAP ($YAlO_3$)	550-600	0.20-7.0	no	cubic
YLF ($YLiF_4$)	400-560	0.12-8.0	no	tetragonal
$CaGa_2S_4$	350-400	0.34-12	no	orthorhombic
BYF (BaY_2F_8)	350-415	0.15-9.0	no	monoclinic
KYF (KYF_4)	350-400	0.20-10	no	hexagonal
LaF_3	300-350	0.20-10	no	trigonal
$LaCl_3$	240-260	0.30-25	highly	hexagonal
$LaBr_3$	175	0.30-20	highly	hexagonal
$CsCdBr_3$	150-160	0.40-25	no	cubic
KPB (KPb_2Br_5)	140	0.40-25	no	monoclinic

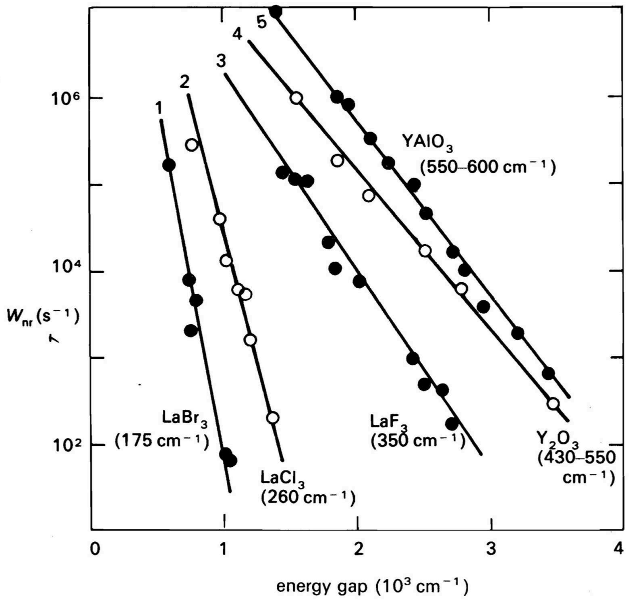

Figure 1.3: Multiphonon relaxation rate at low T as function of the energy gap between the one manifold and the next lower one for five different phonon energyy [3].

that depends roughly in an exponential way on the effective phonon energy of the host matrix (Fig. (1.3)). In Eq. (1.26) it is possible to distinguish two components. The first one depends on the temperature and is related to the Bose-Einstein distribution function $n(T)$ of phonons. It describes the stimulated emission of phonons. The second component, represented by the term 1, describes the spontaneous emission of phonons. This model is derived by assuming that all phonons share the same energy, called effective phonon energy, that is the average of the energy phonon spectrum. In general, oxides have large phonon energy, followed by fluorides, chlorides, iodides, and bromides.The multiphonon relaxation and the radiative emission are competitive process. When $\Delta E < 5\hbar\omega_{\mathrm{eff}}$, the non-radiative transitions generally quench the upper manifold.

Let us consider a manifold $^{2S+1}L_J$ that it is separated from the next lower one by an energy $\lesssim 3\hbar\omega_{\mathrm{eff}}$. In this situation, the measured lifetime of the lowest level is generally more than $1\,\mu s$. It must be noted that the relaxation between the Stark levels in the manifold can also be assisted by acoustical phonons. This kind of relaxation has a characteristic time shorter by several orders of magnitude than the multiphonon relaxation of the lowest level. In this case, one can deduce that the ions excited to the manifold very quickly establish an equilibrium Boltzmann population distribution. Thus, radiative emission from these populated Stark levels occur to those of the lower manifolds and the spectrum consists of several lines. By contrast, at low temperature only the lowest level of the manifold is populated and the number of lines decreaseas.

1.3.3 Interaction between rare earth ions

The long lifetime of the $4f$ excited states gives some quenching mechanisms, such as energy transfer between RE ions, the possibility to occur. One type of excited state, called donor or sensitizer (D), transfers energy to a nearby ion, called acceptor or activator (A). In rare earths doped crystals, energy transfer may occur between ions of the same element or also between ions of different elements. This mechanism has been extensively applied for the development of lasers and many more optical devices.
According to the Fermi's Golden Rule, the energy transfer rate W^{DA} can be expressed as [22]:

$$W^{\mathrm{AD}} = \frac{2\pi}{\hbar} | \langle \Psi_f^{\mathrm{A}} \Psi_f^{\mathrm{D}} | \, H_{\mathrm{int}} \, | \Psi_i^{\mathrm{A}} \Psi_i^{\mathrm{D}} \rangle |^2 \int F^{\mathrm{A}}(E) F^{\mathrm{D}}(E) \, \mathrm{d}E \tag{1.29}$$

where H_{int} is the hamiltonian that describes the electrostatic interaction between donor (D) and acceptor (A). The wavefunctions Ψ^D and Ψ^A describe the states of the two ions, respectively, in the initial (bra) and final (ket) states. The integral represents the overlap between the donor emission spectrum $F^{\mathrm{D}}(E)$ and the acceptor absorption spectrum $F^{\mathrm{A}}(E)$ and it is maximum when the differences between the levels of the donor and acceptor are equal, i.e. when they are resonant. However, thanks to phonon assisted processes, energy transfer may occur even though the levels are out of resonance. Energy transfer involving emission of phonons is usually more probable than absorption[11] and, as a consequence, the dependence on the energy mismatch ΔE_m of this process is similar to that of multiphonon relaxation [20]:

$$W^{\mathrm{DA}}(\Delta E_m) = W^{\mathrm{DA}}(0) \exp \left\{ \Delta E_m \hbar \omega_{\mathrm{eff}} \left[\ln \left(\frac{p}{S_0(n+1)} - 1 \right) - \ln \left(1 + \frac{S_{0,A}}{S_{0,\mathrm{D}}} \right) \right] \right\} \tag{1.30}$$

in which $S_{0,\mathrm{A}}/S_{0,\mathrm{D}} \approx 1$ is the ratio between the Huang-Rhys parameters of acceptor and donor at very low temperature, respectively. It must be noted that, at low temperature, only the lowest level of the manifolds is populated, so a resonance is less probable to occur.

The electromagnetic interaction can be expressed as a multipolar series [22] whose dominant contributions need only to be taken in account. By considering only dipole-dipole-, dipole-quadrupole-, and quadrupole-quadrupole interactions and by recalling that $W^{\mathrm{AD}} \propto |H_{\mathrm{int}}|^2$, the energy tranfer rate can be written as:

$$W^{AD}(R) \approx \frac{a^{\mathrm{d-d}}}{R^6} + \frac{a^{\mathrm{d-q}}}{R^8} + \frac{a^{\mathrm{q-q}}}{R^{10}} \tag{1.31}$$

where $a^{\mathrm{d-d}}$, $a^{\mathrm{d-q}}$, $a^{\mathrm{q-q}}$ are the coefficients relative to the electric dipole-dipole-, dipole-quadrupole-, and quadrupole-quadrupole interaction, respectively. In general, the magnetic dipole-dipole- and other types of magnetic interactions are smaller and are then neglected.

Because of these interactions, the emission spectrum and the temporal behavior of the relaxation of the excited states might show a strong dependence on the concentration, in

---

[11] Especially at low T.

particular on the mean separation R between donor and acceptor. Actually, the energy transfer mainly occurs between the donor and the nearest neighbor acceptors, for which the distance is short enough for a direct overlap of their electronic wavefunctions to occur. Inokuti and Hirayama [23] proposed a model in order to simulate the fluorescence time evolution:

$$I(t) = I(0)\mathrm{exp}\left[-\frac{t}{\tau} - \Gamma\left(1-\frac{3}{s}\right)\frac{N_a}{N_c}\left(\frac{t}{\tau}\right)^{\frac{3}{s}}\right] \tag{1.32}$$

where Γ is the gamma-function, τ is the intrinsic decay lifetime, s defines the type of interaction ($s = 6, 8, 10$ respectively for electric d-d-, d-q-, and q-q interaction), N_a is the acceptor concentration and N_c is a parameter called critical concentration of acceptor. In case the dipole-dipole interaction is dominant, Eq. (1.32) becomes:

$$I(t) = I(0)\mathrm{exp}\left(-\frac{t}{\tau} - \gamma\sqrt{t}\right) \qquad \gamma = \frac{4}{3}\pi^{\frac{3}{2}}N_a\sqrt{a^{\mathrm{d-d}}} \tag{1.33}$$

In the Inokuti-Hirayama theory, in addition to a random continuos distribution of acceptors around donors, some further conditions are assumed, in particular that the energy transfer can happen only between donor and acceptor. Other models [24, 25] expand the Inokuti-Hirayama one by considering also the donor-donor interaction, but they are not considered in this work because the presented measurements do not require such a complicated description.

Energy transfer processes can mainly be distinguished in four different phenomena that are exemplified in Fig. (1.4):

- **Energy transfer upconversion (ETU)**: when two spatially close ions are both excited, the donor may relax to a lower energy state and the acceptor is promoted to a higher energy level.

- **Energy transfer Down-Conversion**: part of the energy of the donor is delivered to the acceptor. In case the donor and the acceptor are ions of the same element, the process is usually called cross relaxation (CR).

- **Energy migration**: this process involves two ions in different energy levels. One ion takes on the state of the other but the final configuration is the same as the initial one. The only results are the spatial migration of the energy from a ion to another and an increase of the radiative emission decay lifetime.

- **Cooperative luminescence**: Two nearby excited ions can simultaneously relax by emitting a photon of energy equal to the sum of the energy of the two ions. In this case, both ions act as donors.

The first three process can have a strong impact on the emission spectrum even at low concentration (less than 1%). The fourth one is less probable and, generally, it is possible to observe it only in particularly high doped systems. These processes can be distinguished

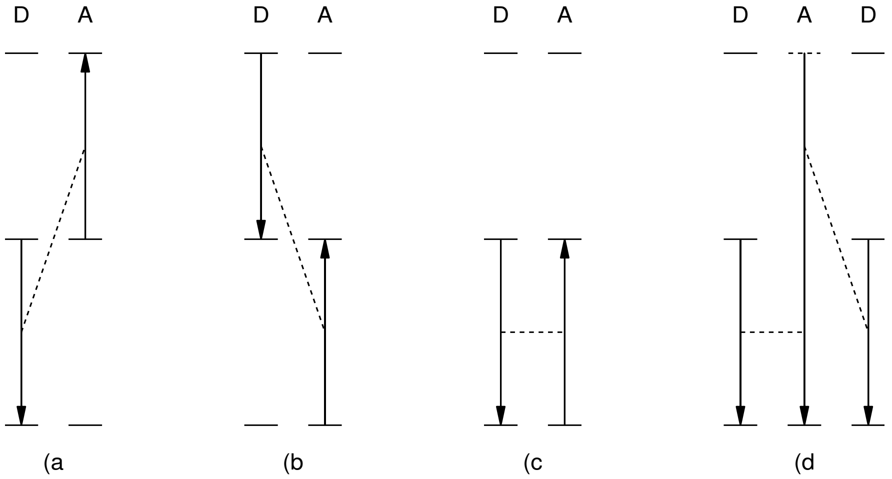

Figure 1.4: Scheme of the main energy transfer process. a) Energy transfer upconversion. b) Cross Relaxation. c) Energy migration. d) Cooperative luminescence.

from a combination of spontaneuos emission and absorption of photons because they occur with their own characteristic times and depend on the population distribution of the excited states.

1.3.4 Total lifetimes

As a consequence of the above described phenomena, the lifetimes τ of the excited states depend on three factors:

$$\frac{1}{\tau} = \frac{1}{\tau_R} + W^{\mathrm{MP}} + W^{\mathrm{AD}} \tag{1.34}$$

τ_R is the intrinsic radiative lifetime , W^{MP} is the multiphonon relaxation rate, and W^{AD} is the energy transfer process rate. A particular excited state has, in general, an intrinsic radiative lifetime which is roughly independent of the host matrix. However, the other two mechanisms can quench the photon emission depending on the effective energy phonon of the host matrix and on the concentration of the dopants.

1.4. Light absorption

A very careful study of light absorption processes is, obviously, of crucial importance for our purposes. Owing to the high optical quality of the dielectric single crystals investigated in this work, the host materials can be considered as trasparent from the mid-infrared range, outside of absorption band due to the lattice vibrational mode, up to the wavelength corresponding to the energy of the conduction band, in UV optical range, as reported in Tab. (1.2). When these host single crystals are doped with RE^{3+}, they inherit the energy level scheme of the dopant (influenced by the crystal field as described in the first section). In addition, a broad intense absorption is sometimes observed at a given frequency that depends both on the host matrix and the RE^{3+} ions. This is due to process of transfer of one electron, called charge transfer (CT) process, between the dopant and a ligand ion.

In this section, we first characterize the attenuation of the light crossing the crystal. Then, resonance absorption processes are distinguished by the type of energy level involved by specifying their typical cross section and linewidth. Finally, we will deal with the non-resonant absorption assisted by phonons.

1.4.1 Light extinction by the crystal matrix

The decrease of the intensity of a weak radiation of wavelength λ propagating in a crystal is described by the Beer-Lambert law

$$I(z,\lambda) = I(0)e^{-\alpha(\lambda)z} = I(0)e^{-n_0 z\sigma_{GSA}(\lambda)} \tag{1.35}$$

in which z is the distance travelled by light in the crystal. α is the absorption coefficient and n_0 is the density of atoms with a absorption cross section from the ground state equal to $\sigma_{\mathrm{GSA}}(\lambda)$[12].

In Eq. (1.35) it has been supposed that all atoms (ions) are in the ground state. As the RE^{3+} excited states can have a lifetime as long as several milliseconds, in a stationary regime with a continuos pump the fraction of ions in a excited state may be not negligible. In this case, the Beer-Lambert law becomes [18]:

$$I(z,\lambda) = I(0,\lambda)e^{-(n_0-n_1)z\sigma_{\mathrm{GSA}}(\lambda)+n_1 z[\sigma_e(\lambda)-\sigma_{\mathrm{ESA}}(\lambda)]} \tag{1.36}$$

Here, n_1 is the density of ions in the excited state that is characterized by the stimulated emission cross section $\sigma_e(\lambda)$ and by the excited state absorption (ESA) cross section $\sigma_{\mathrm{ESA}}(\lambda)$.

We have considered only one excited state, but it is simple to modify the equation in order to include more states. A pump-probe technique commonly used in order to measure these cross sections is described in literature [26].

1.4.2 Resonant absorption types

It is possible to classify the resonance absorption of RE in $4f$ states into three main categories according to the RE final state [27].

Intraconfigurational $4f^n - 4f^n$ transition As mentioned before, the transitions $4f^n - 4f^n$, including absorption from an excited state (ESA), are weakly parity allowed. The typical absorption cross section values range between 10^{-21} and 10^{-19} cm^2 and the linewidths may usually be very narrow [18].

---

[12] We have assumed that there is only a type of atom (ions) responsible for the absorption.

Interconfigurational $4f^n - 4f^{n-1}5d$ transition Contrary to the $4f$ levels, the energy of $5d$ levels may change even by tens of thousands of cm^{-1} from compound to compound. In order to predict this energy, Dorenbos [10] has introduced the following equation:

$$E(Ln, A) = 49\,340\,\mathrm{cm}^{-1} - D(A) + \Delta E^{\mathrm{Ln,Ce}} \tag{1.37}$$

The energy of the lowest $5d$ level of the Lantanides Ln in the compound A depends on the energy of the $5d$ level of Ce^{3+} as a free ion in the gas phase, on the so-called crystal field depression $D(A)$, that depends only by the host matrix, and on the difference between the lowest $5d$ spin-allowed level of Ln and Ce, $\Delta E_{sa}^{\mathrm{Ln,Ce}}$, which has a weak dependence on the compound.

Dorenbos has measured or estimated the parameter $D(A)$ for hundreds of compounds allowing the researchers to calculate, using ,Eq. (1.37), the position of $5d$ levels with an accuracy of $\pm\,600\,\mathrm{cm}^{-1}$. For example, $D(A)$ can range between about 7000 and $17000\,\mathrm{cm}^{-1}$ for fluorides, between about 10000 and $32000\,\mathrm{cm}^{-1}$ for oxides, between about 24000 and $34000\,\mathrm{cm}^{-1}$ for sulfides. Tab. (1.3) provides the values of $\Delta E_{sa}^{\mathrm{Ln,Ce}}$ and of the difference between the lowest $5d$ spin-forbidden level of Ln and Ce $\Delta E_{sf}^{\mathrm{Ln,Ce}}$ when it is less than $\Delta E_{sa}^{\mathrm{Ln,Ce}}$. The absorption cross section is about $10^{-18} - 10^{-17}\,\mathrm{cm}^2$ [9].

The $5d$ levels are very numerous and close each other. In large band gap crystals it is possible to observe the RE^{3+} $5d$ band splitted by the crystal field into relatively well isolated levels [28]. Thus, when they are excited, they quickly relax to the lowest $4f$ levels. Unless multiphonon relaxation or energy transfer occur, a broad and fast emission (of the order of $10 - 100\,\mathrm{ns}$) from this level is due to the allowed electric dipole[13] transitions well coupled with phonons. The relevant Stokes shift makes the crystal transparent to its own $5d$ levels emission.

Charge transfer (CT) A valence electron can be transferred from the ligand toward the unoccupied orbitals of the RE through the absorption of a photon[14]. In RE^{3+} doped crystals, the dopant becomes divalent thereby increasing his atomic radius. The lattice reaches faster a new equilibrium position releasing a large amount of energy as phonons (Fig. (1.5)). Then, the ligand recaptures the electron thereby leaving the RE in trivalent form in the ground state or in an excited state. The excess energy may be released through the emission of a photon. A Stokes shift of several tens of nm is usually observed [29]. However, at room temperature, the luminescence is thermally quenched heavily in many compounds.

Jørgensen [30] has proposed a simple formula to predict the photon energy required for

---

[13] Actually, some $4f - 5d$ transition can be spin forbidden In some RE^{3+} this $5d$ levels have less energy than that spin allowed one and can be observed as shown Tab. (1.3).

[14] More specifically, this process is noted as Ligand to Metal Charge Tranfer (LMCT) absorption. Actually, the opposite MLCT process can occur with more energetic photons but it is not studied in RE doped crystal.

Table 1.3: Optical electronegativity of RE^{3+} and energy difference between the first spin allowed and spin forbidden 4f-5d transition in Ln^{3+} with that of Ce^{3+}.

$\mathbf{RE^{3+}}$	$\chi_{\mathbf{opt}}$	$\mathbf{\Delta E_{sa}^{Ln,Ce}}$ [cm^{-1}]	$\mathbf{\Delta E_{sf}^{Ln,Ce}}$ [cm^{-1}]
Ce^{3+}	1.1	0	-
Pr^{3+}	2.0	12240	-
Nd^{3+}	1.2	22700	-
Pm^{3+}		25740	-
Sm^{3+}		26500	-
Eu^{3+}	1.8	35900	-
Gd^{3+}		45800	-
Tb^{3+}		13200	6300-7700
Dy^{3+}		25100	5200-7400
Ho^{3+}		31800	2700
Er^{3+}		30000	3050
Tm^{3+}	1.6	29300	2350
Yb^{3+}	1.7	38000	-

the process:

$$E \approx 30\,000\,\mathrm{cm}^{-1}(\chi_{\mathrm{opt}}(L) - \chi_{\mathrm{opt}}(M)) \tag{1.38}$$

where χ_{opt} is the optical electronegativity defined by Jørgensen and the symbols L and M correspond to ligand and metal (RE ion in our case), respectively. A more accurate expression can be found elsewhere [27, 29]. The value of the optical electronegativity of Lantanides and the common ligand are presented in Tab. (1.3), and Tab. (1.4) respectevely. Charge transfer transition is allowed electric dipole type and the fast emission[15], located in visible-UV, is broad. The charge transfer can occur at lower photon energy in the case the dopant is in an excited state. CT absorption may overlap with $4f$ to $5d$ levels absorption, thereby being difficult to distinguish.

Table 1.4: Optical electronegativity for the ligands considered in the inorganic compounds [32]

F^-	Cl^-	Br^-	O^{2-}	I^-
3.9	3.0	2.8	3.2	2.5

For the sake of completeness, we recall the existence of several more processes, among which one important example is the two photon absorption process, where the first step-level is virtual. In our case it can be neglected because it has a very low cross section at the intensity used in the experiment presented in this thesis. In Fig. (1.6) a typical Dorenbos energy level scheme of RE^{3+} has been represented.

---

[15] The order of magnitude of the radiative lifetime is 10^2 ns. However, the divalent ions at low T can be trapped and relax only at higher T [31].

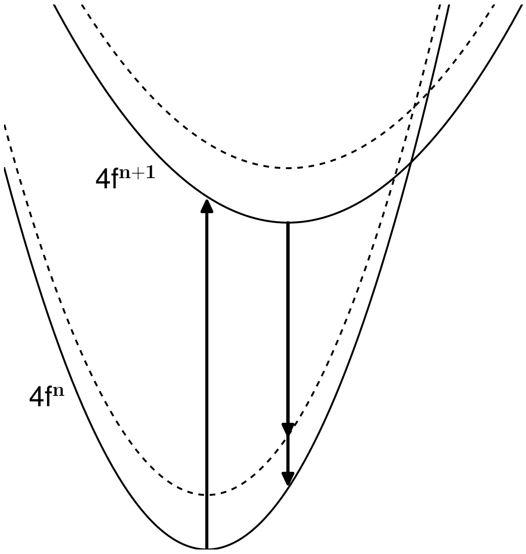

Figure 1.5: Energy of Yb ions versus nucleus displacement(configuration coordinate). There are shown the energy of both Yb^{3+} and Yb^{2+}, illustrating the transitions involved in charge transfer.

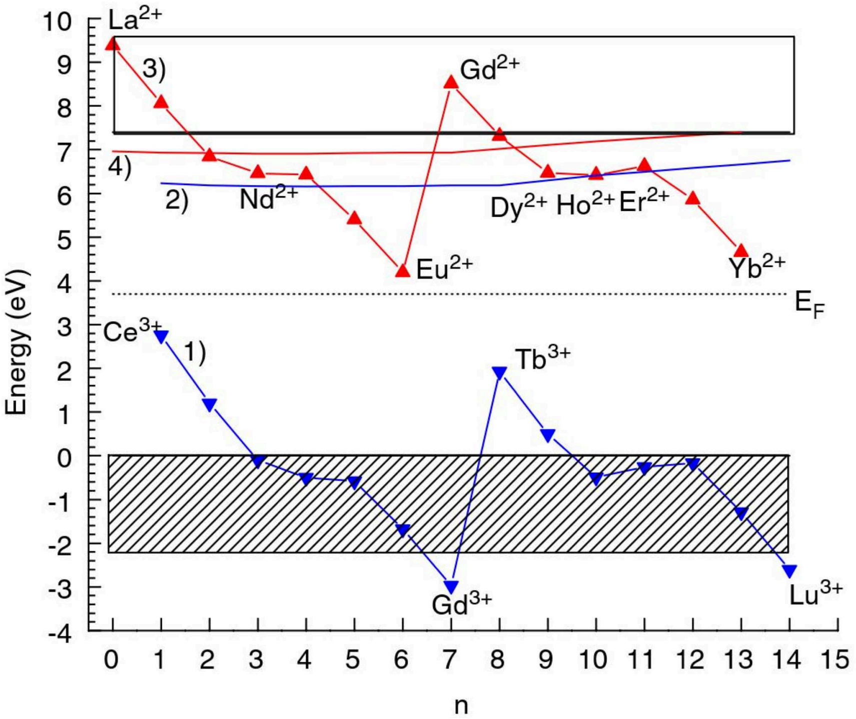

Figure 1.6: Energy level scheme of the lanthanides in $SrAl_2O_4$. Curves 1 and 2 connect the lowest level of the $4f^n$ configuration and the $4f^{n-1}5d$ configuration of the trivalent lanthanides, respectively. Curves 3 and 4 connect the lowest level of the $4f^{n+1}$ configuration and the $4f^n5d$ configuration of the divalent lanthanides, respectively. E_F is the Fermi energy midway between the valence and conduction band [33].

1.4.3 Color center and impurities

Because all RE have the same chemical properties, they are difficult to chemically separate from each other. The amount of impurities of other RE and other elements of highly pure powders used for the crystals growth is limited to tens of p.p.m. or less and can be determined by spectroscopic analysis. The term color centers is referred to a type of crystallographic defect that can absorb light at well defined frequencies. For example, the well studied F-center is an anionic vacancy in a crystal that is filled by one or more unpaired electrons. Impurities and especially color centers can quench the dopants emission.

1.4.4 Side band multiphonon assisted absorption

In the previous sections, the processes involving the absorption of one resonant photon have been discussed. Out of resonance, one can still observe absorption even though it is characterized by a cross section smaller by several orders of magnitude than that at resonance. Auzel [21] has associated this phenomenon to the multiphonon assisted absorption from the RE ion ground state to an excited state.

By inspection of Fig. (1.7), let E_i be the ion energy levels. The absorbed laser intensity fraction as function of the radiation energy E, assuming without loss of generality $E_1 < E < E_2$, can be theoretically given as a sum of two terms:

$$I(E) = I(E_1)\exp[-\alpha_S(E - E_1)] + I(E_2)\exp[-\alpha_{\mathrm{AS}}(E_2 - E)] \tag{1.39}$$

with:

$$\alpha_S = (\hbar\omega_{\mathrm{eff}})^{-1}\ln\left(\frac{p}{S_0(n+1)} - 1\right) \tag{1.40}$$

and

$$\alpha_{\mathrm{AS}} = \alpha_S + \frac{1}{kT} \tag{1.41}$$

The first term in r.h.s of Eq. (1.39) is related to the so-called Stokes process: an ion absorbs one photon and it is promoted to the excited state with energy E_1 releasing the energy in excess through the emission of one or more phonons. The amount of absorbed intensity depends on that at resonance $I(E_1)$ and roughly decreases in an exponential way with the number of phonons $p = (E - E_1)/(\hbar\omega_{\mathrm{eff}})$ involved, on average, in the process. In the AntiStokes process, described by the second term in r.h.s. of Eq. (1.39), an ion absorbs simultaneously one photon and enough phonons from the lattice in order to be promoted to the excited state characterized by energy E_2.

Contrary to the Stokes parameter α_S, α_{AS} has a strong dependence on T because the process depends on the energy absorption from the thermal bath. This theoretical prediction has been confirmed by measuring the absortion cross section as a function of the laser wavelength at room temperature, as can be seen by inspecting Fig. (1.7). Close to the resonance of the manifold $^4\mathrm{S}_{3/2},^4\mathrm{F}_{9/2},^4\mathrm{I}_{9/2}$, the absorption cross section is of the order of $10^{-20}\,\mathrm{cm}^2$. It decreases linearly (in logscale) by 6 orders of magnitude with the

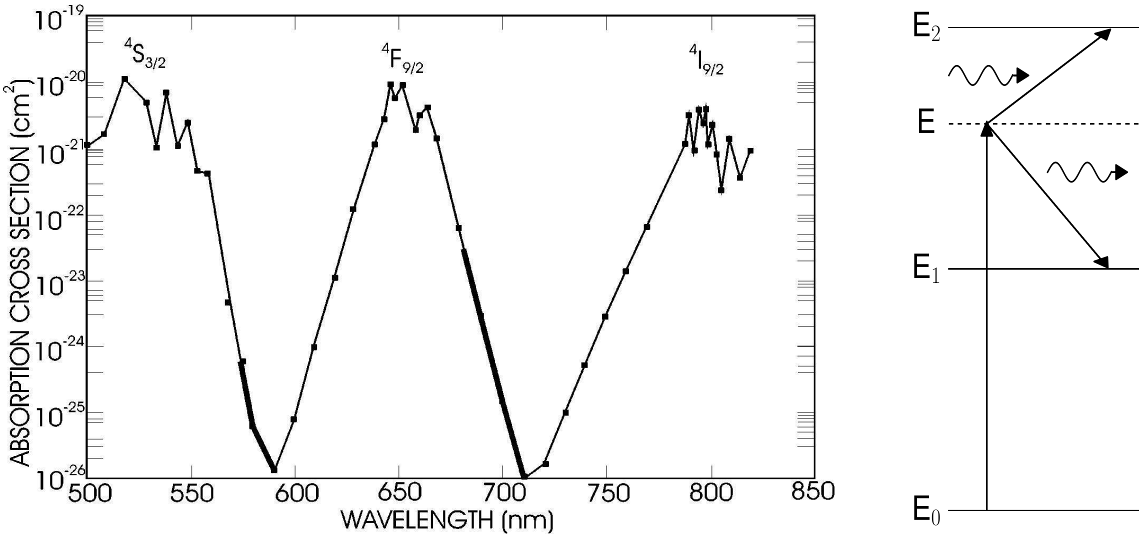

Figure 1.7: Multiphonon absorption cross section of Er^{3+}:YLF between $^4I_{9/2}$ and $^4S_{3/2}$ terms at room temperature [34]. Stokes and Antistokes processes scheme.

increase of pump photon energy until the AntiStokes process becomes important. The absorption cross section, then, increases linearly (in logscale) with the increase of pump photon energy according to the second term of Eq. (1.39), until the resonance with the next higher manifold is achieved.

1.5. RE doped crystals as active media for detectors

Rare earths play an important role in many light emitting devices thanks to their high competitive light emission processes in comparison with non-radiative ones. For the same reason, rare earth doped crystals are widely exploited as scintillators. In the first part of this section, we discuss the processes occurring in RE doped crystal when they are excited by ionizing radiation. Furthermore, the best RE based scintillator with their technical features and application are mentioned.

In the second part, we describe the working principle of the InfraRed Quantum Counter (IRQC) that many researchers have unsuccesfully tried to achieve during the last 50 years. However, many progress are made since the IRQC concept was proposed in 1959 by Bloembergen.

1.5.1 RE in inorganic scintillators

When a gamma ray (or other ionizing radiations) interacts with the crystal, energy is released by a variety of processes. In particular, a cascade process occurs when the photoelectron released by the gamma ray absorption, ionizes other atoms by creating more

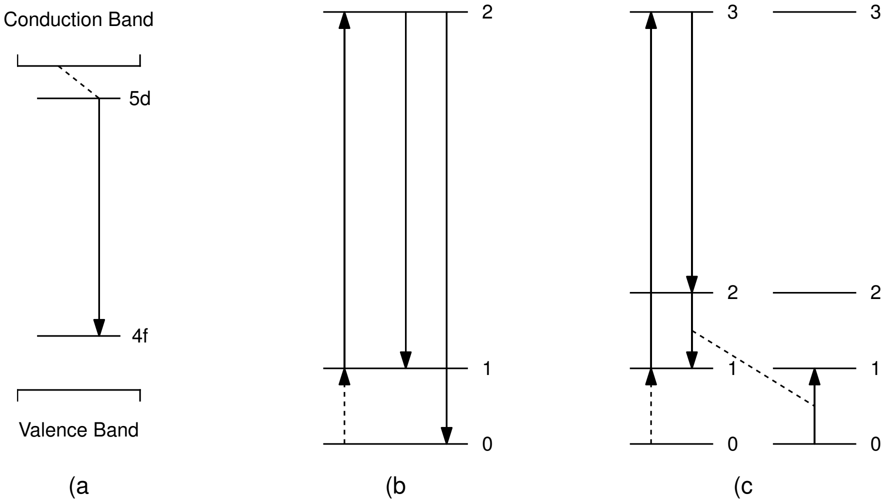

Figure 1.8: a) Scheme of the scintillation processes. b) Scheme of IRQC. c) Scheme of photon avalanche upconversion.

photoelectrons or when deep holes produced by the gamma ray absorption create Auger electrons and x-rays. This chain reaction stops as soon as the energy of these secondaries electrons or x-rays falls below the threshold energy needed to create the electron-hole (e-h) pairs ϵ_{min}.

The conversion efficiency β[16] is defined as the ratio between ϵ_{min} and the average effective energy needed to create a e-h pair. A considerable part of the energy may be lost in the creation of optical phonons that result in an enhancement of the sample temperature.

For RE doped crystals excited by gamma/x-rays, $\epsilon_{\text{min}} \approx (2.3 - 2.5)\, E_g$, where E_g is the energy gap of the crystal. The recombination of the pairs may occur yielding their energy to the activator (the RE ions) that emits a photon Fig. (1.8). Let T and QY be the probability of this energy transfer[17] and the quantum yield of the RE ions transition, i.e the probability to emit the photon, respectively. [35].

The number of photons produced by the scintillator, in which the energy E_γ is deposited by the radiation, is given by:

$$n_p = \frac{E_\gamma}{\epsilon} \cdot S \cdot Q = \frac{E_\gamma}{2.3 E_g} \cdot \beta \cdot S \cdot Q \qquad (0 \leq \beta, S, Q \leq 1) \tag{1.42}$$

Hence, the light yield (LY), i.e., the number of photons produced per MeV of energy

---

[16] β may depend on the type and energy of radiation.

[17] In low activator's concentration is reasonable to assume that all the radiation energy is released in the host matrix and then a part is transferred to the activator. In the case of high concentration- or stoichiometric materials, the previous assumption is not reasonable because the conversion and transfer processes tend to merge but this treatment can still be applied formally.

deposited in the scintillator, can be expressed as

$$LY = \frac{1\,\mathrm{MeV}}{2.5 \cdot E_g} \cdot \beta \cdot S \cdot Q \qquad (0 \leq \beta, S, Q \leq 1) \tag{1.43}$$

In Fig. (1.9) we show LY for gamma ray excitation as a function of E_g. From Eq. (1.43) and confirmed by Fig. (1.9), it is clear that $LY \leq 1\,\mathrm{MeV}/(2.5E_g)$.

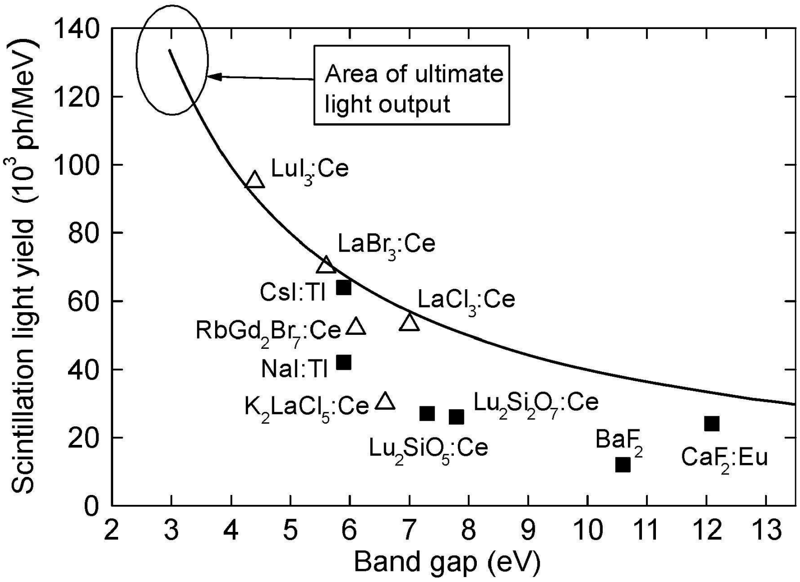

Figure 1.9: LY for γ-ray excitation vs E_g for the most common scintillators (black squares) and more recent ones (empty triangles) developed by the groups of Krämer and Dorenbos [36].

The most important requirement for a scintillator for many applications is speed in order to detect high counting rate signals and a high LY in UV-visible range, where photomultiplier tube or silicon photomultiplier are most efficient. However, even scintillators with several μs decay time have found applications in security systems and x-ray computed tomography.

Ce^{3+} is the active RE used in most scintillators. It ehxibits a bright luminescence, a fast decay time due to allowed $5d$-$4f$ transitions, and a suitable $4f$ energy level scheme. It has only two manifolds that are separated by a few tens of thousands of cm^{-1} from the lowest $5d$ level. In addition to that, it is trasparent to the Cerium emission thanks to the large Stokes shift and it has an high quantum yield Q. In particular Ce^{3+}:$LaBr_3$ has thoroughly been investigated for its high LY (60×10^3 ph/MeV between 350 and 430 nm), for its high energy resolution (2.6 % at 662 keV), and for its fast decay time (16 ns). Recently even the $5d - 4f$ transitions of Pr^{3+}:LuAG ($LY = 33 \times 10^3$ ph/MeV) and Eu^{2+}:SrI_2 ($LY = (100 - 120) \times 10^3$ ph/MeV with decay time equal to 1-2 μs) have been used.

Also charge transfer luminescence of Yb^{3+} is also attractive for its very fast decay time (even less than 1 ns[18]) at room temperature, in spite of its relatively low LY. Yanagida [37] has investigated $4f - 4f$ transitions in the range between the UV band and 800 nm, which

---

[18] It is due to the fast multiphonon relaxation that strongly limits the LY.

are characterized by a decay time of few microseconds. He has found LY as high as up to 15×10^3 ph/MeV.

1.5.2 Infrared Quantum Counter and photon avalanche upconversion

In 1959 Bloembergen [38] proposed to use the principle of excited state absorption in order to realize an infrared quantum counter. A rare earth ion is excited by one infrared photon, then a strong light source, used as a pump, promotes it to a more energetic state whose fluorescence in the visible range can be detected with a higher quantum efficiency using a photomultiplier tube. The main problem is that a fraction of the pump is absorbed by the ions in the ground state thereby exciting ions in the same state that infrared photons only should populate. In 1979, while studying this issue on $LaBr_3$ and $LaCl_3$ doped Pr^{3+} at low temperature, Chivian [39] discovered a new phenomenon that they denoted as photon avalanche.

The sample was exposed to a continuous wave dye laser pump radiation, tuned between the $^3H_5$ and $^3P_1$ manifolds and also non resonant with the ground state (Fig. (**??**) on page **??**). The fluorescence emitted by the $^3P_1$ and $^3P_0$ relaxation increased by orders of magnitude, as well as the pump absorption, as soon as the laser intensity was in excess of a certain critical value. The dye laser promotes the ions in $^3H_5$ to $^3P_1$ and $^3P_0$ level that relax mainly to the $^3H_6$. Now, an efficient cross relaxation $^3H_6 +^3 H_4 \rightarrow^3 H_5 +^3 H_5$ occurs. Not only the first ion returns in the $^3H_5$ state but also a nearby ion from the ground state is excited to the same manifold Fig. (1.8). When the laser intensity exceeds the critical value, the excitation rate of the ions in state $^3H_5$ due to the laser exceeds their natural relaxation rate, their population strongly increases thereby resempbling an amplification circuit with positive feed-back [40]. According Eq. (1.36), the increasing of the ions in the state $^3H_5$ enhances the pump absorption. A more detailed analysis can be found in [34], [41]. The photon avalanche process, as efficient combination of excited state absorption and cross relaxation, is applied to other rare earth element, such as Tulium, Holmium, Erbium, Samarium, Neodymium [42].

Since its discover, the photon avalanche was considered by many researchers a limitation rather than an advantage for the infrared radiation detection. Only recently, Gatch and *et al.* [43] managed to apply it to $Pr:LaCl_3$ in order to realize an infrared detector (1.0-2.3 μm) with a good noise equivalent power (NEP) equal to $9.3 \cdot 10^{-15}\,\mathrm{W}/\sqrt{\mathrm{Hz}}$ at room temperature, (comparable to common thermoelectrically cooled InGaAs detector).

Chapter 2

Implementation of a RE based detector

In the previous chapter the optical properties of rare earths have been presented. In this thesis, we want to investigate the possibility to apply the IRQC idea, that is briefly discussed in the Sec. (1.5.2), to the particle detection. We propose here a model to simulate and study the main technical features of a detector, such as time response, efficiency, and noise. The results and some assumptions will be confirmed in the the chapter 4.

2.1. A working model

In this simplified model, non-radiative processes, reabsorption, stimulated emission and side band absorption are neglected. The last two will be considered subsequently. For the realization of the detector we will use the RE energy level scheme with large energy gap between the considered levels (manifolds) or/and with host matrix with low phonon energies in order to reduce the quenching due to multiphonon relaxation. If the RE ions concentration is not too high, reabsorption can be neglected. If not, it can be treated by adjusting some parameters. Also the energy transfer processes are neglected in this model.

Let us consider a scheme of RE^{3+} doped crystal made up by five $4f^n$ energy levels as shown in Fig. (2.1). Let n_i, τ_i, β_{ij} and σ_{ij} be the fraction of the N ions that are excited in the i-th level, their radiative lifetimes, the branching ratio, and the absorption cross section from the i-th to the j-th level, respectively. A continuous wave (cw) laser, of intensity I and tuned to the frequency ν, provides the upconversion from state 1 to 4. In addition, no resonance absorption from the ground state occurs so that I can be considered costant all over the crystal. Hence, under only laser excitation all the ions are in ground state ($n_0 = 1$) until a particle (at the time $t = 0$), penetrates the crystal and, during a negligible time interval, excites $n_1(0)$ ions to the level 1.

A fraction of these ions is brought to the level 4 by mean of the laser. We suppose that level 4 mainly relaxes to the ground state and to level 1. This simplification is done to neglect the populations of level 2 and 3, but they can be easily included. The equations that describes the time evolution of the populations of the levels are

$$\begin{aligned} n_0(t) &\approx 1 && (2.1)\\ \frac{dn_1}{dt} &= -n_1\left(\frac{1}{\tau_1}+\sigma_{14}\frac{I}{h\nu}\right)+n_4\frac{\beta_{41}}{\tau_4} && (2.2)\\ \frac{dn_4}{dt} &= +n_1\sigma_{14}\frac{I}{h\nu}-n_4\frac{1}{\tau_4} && (2.3)\end{aligned}$$

Most of the ions remain in the ground state and after a (relatively) long time all excited ions are relaxed to the ground state. As shown by Eq. (2.2), two competitive mechanisms depopulate level 1: spontaneous emission, represented by the term $1/\tau_1$ and the upconversion process represented by $\sigma_{14}I/h\nu$. We can define the upconversion efficiency $\epsilon_{\rm up}$ as the fraction of the $n_1(0)$ ions in level 1 at $t = 0$ that has been promoted ("upconverted") to the level 4. The upconversion efficiency can be also expressed as:

$$\epsilon_{\rm up}=\frac{\sigma_{14}\frac{I}{h\nu}}{\frac{1}{\tau_1}+\sigma_{14}\frac{I}{h\nu}}=\frac{1}{1+\frac{h\nu}{\sigma_{14}\tau_1 I}} \qquad (2.4)$$

A high upconversion efficiency is obtained if the level 1 has a long lifetime and a large absorption cross section. Moreover, the laser must be intense. If the upconversion process

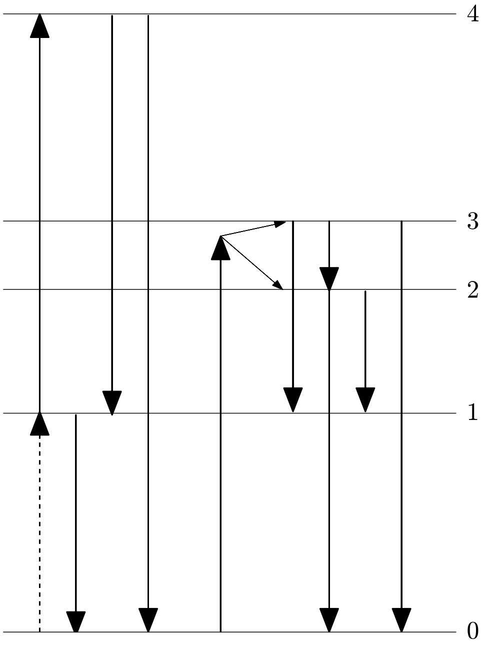

Figure 2.1: Scheme of the detection and noise generation processes. The dashed arrow the particle excitation.

is much less efficient than the spontaneous relaxation ($\tau_1 \ll h\nu/\sigma_{14}I$), i.e., when laser intensity is very low, Eq. (2.4) can be approximated by:

$$\epsilon_{\mathrm{up}} = \frac{1}{h\nu}\sigma_{14}\tau_1 I \tag{2.5}$$

Level 4 relaxes radiatively with its own lifetime τ_4 to the level 1 or to the ground state. In the first case, the emitted photon is indistinguishable from those of the laser[1]. Thus, only the second transition, i.e., that to the ground state, can be identified as the signal produced by the particle to be detected, once selected through suitable optical filters.

The first important parameter of the detector is the "effective upconversion efficiency" η_{up}, defined as the number of photons emitted in this transition ($4 \to 0$) divided by the number of ions excited to level 1 by the particle. It can be written as:

$$\eta_{\mathrm{up}} = \frac{1}{N \cdot n_1(0)} \int \frac{N \cdot n_4(t) \cdot \beta_{40}}{\tau_4} dt = \frac{1}{n_1(0)} \int \frac{n_4(t)\beta_{40}}{\tau_4} dt \tag{2.6}$$

It should be noted that the ions relaxing from level 4 to level 1 may be again upconverted to level 4 by the laser. The fraction of ions in level 4 that relax at first to level 1 and then are again upconverted, thereby accomplishing a "cycle", is $\beta_{41}\epsilon_{\mathrm{up}}$. It can be easily deduced that the fraction of ions that have accomplished j cycles is $(\beta_{41}\epsilon_{\mathrm{up}})^j$ and for each cycle relaxes to the ground state, emitting a detectable photon, with a probability equal to β_{40}. It is easy to show that

$$\eta_{\mathrm{up}} = \epsilon_{\mathrm{up}}\beta_{40} \sum_{j=0}^{\infty} (\epsilon_{\mathrm{up}}\beta_{41})^j = \frac{\epsilon_{\mathrm{up}}\beta_{40}}{1 - \epsilon_{\mathrm{up}}\beta_{41}} = \frac{\beta_{40}}{\beta_{41}} \left(\frac{1}{\beta_{41}\epsilon_{\mathrm{up}}} - 1 \right)^{-1} \tag{2.7}$$

For $\epsilon_{\mathrm{up}} = 1$, $\eta_{\mathrm{up}} = 1$[2],i.e., all the ions excited by the particle emit one photon more energetic than that they could have spontaneously emitted without the laser pump.

By solving the equations Eq. (2.1), Eq. (2.2), and Eq. (2.3), it is possible to obtain the time evolution of the signal. It mainly depends on the effective lifetime of the level 1 $(1/\tau_1 + \sigma_{14}I/h\nu)^{-1}$ and the natural lifetime of the level 2. In addition, if $\eta_{up}\beta_{41}$ is large, the recycling effect can have a deep effect on the detector response time.

In this model we have neglected the existence of the Stark level splitting as though the laser line width were not so narrow. Actually, one advantage of our apparatus is that the narrow line width of the tunable laser allow us to precisely select the Stark levels out of the manifolds we would like to work with. In this way the absorption cross section σ_{14} is optimized. It must be considered that only ions in that particular Stark level can be promoted and the population in the manifold follows the Boltzmann distribution so the absorption cross section can have a strong dependence on the temperature. In practice, level 1 is the lowest level of the manifold 1 and level 4 can be any level of the manifold 4.

---

[1] Actually, the wavelength is the same but while the photons emitted by the laser have a well-defined polarization, those spontaneously emitted are randomly polarized. Hovewer the discussion is more complicated because a little part of the laser intensity is scattered by the crystal.

[2] We have assumed $\beta_{40} + \beta_{41} \approx 1$.

At low T, however, only the lowest level of the manifold 4 is radiative.

The stimulated emission has the opposite effect of upconversion. It downconverts the ions in level 4 to level 1. However, the lifetime of level 4 is generally much shorter than that of level 1, especially if the level 4 is not the lowest of the manifold 4. Since the stimulated emission cross section is smaller than σ_{14}, it can be neglected to a good approximation. This will be confirmed by the measurements of chapter 4.

As in this model laser side band absorption is not accounted for, there is no room for noise. Unfortunately, this assumption is not correct and, in the measurements we have been carrying on, a large emission from level 4 is caused by the laser only, thereby becoming an important source of noise itself. As it will be proved in chapter 4, this process, due to an absorption of two laser photon and called in this work laser double resonance (LDR) process, is mainly due to the population of the level 1 by means of the laser through the phonon assisted side band absorption. This process has been described in Sec. (1.4.4). Once the level 1 is populated, upconversion can be induced by a second photon, exciting the ions in the level 4.

By referring to our model and Fig. (2.1), level 2 and level 3 can be populated by Stokes and antiStokes processes, respectively. Then, they partly relax to level 1, radiatively or through multiphonon relaxation. As the energy gap between level 1 and the photon is much higher than that between the photon and level 2, the Stokes process that populates directly level 1 can be neglected. However, It can become the predominant noise source in absence of level 2 and at low T, that inhibits the antiStokes processes. We can write the equation in stationary regime that describes the noise as

$$\begin{aligned}
n_0(t) &\approx 1 && (2.8)\\
\frac{dn_1}{dt} &= -n_1\left(\frac{1}{\tau_1}+\sigma_{14}\frac{I}{h\nu}\right)+\frac{n_2\beta_{21}}{\tau_2}+\frac{n_3\beta_{31}}{\tau_3}+n_4\frac{\beta_{41}}{\tau_4}=0 && (2.9)\\
\frac{dn_2}{dt} &= n_0\sigma_{02}\frac{I}{h\nu}-\frac{n_2}{\tau_2}+\frac{n_3\beta_{32}}{\tau_3}+\frac{n_4\beta_{42}}{\tau_4}=0 && (2.10)\\
\frac{dn_3}{dt} &= n_0\sigma_{03}\frac{I}{h\nu}-\frac{n_3}{\tau_3}+\frac{n_4\beta_{43}}{\tau_4}=0 && (2.11)\\
\frac{dn_4}{dt} &= n_1\sigma_{14}\frac{I}{h\nu}-n_4\frac{1}{\tau_4}=0 && (2.12)
\end{aligned}$$

Here, we have introduced the laser absorption cross section σ_{02} and σ_{03} that are related to the Stokes and antiStokes processes and several branching ratios that take even into account multiphonon relaxation. If we neglect the relaxation term from level 4 in the equations for the population of level 2 and 3 (Eq. (2.10) and Eq. (2.11)), the stationary fraction of ions in these two levels is proportional to laser intensity. Hence, it is possible to introduce an effective laser absorption cross section σ_{01} that takes into account the population of the level 1 as a consequence of the Stokes and antiStokes processes

$$\sigma_{01}=(\sigma_{02}+\beta_{32}\sigma_{03})\beta_{21}+\sigma_{03}\beta_{31} \qquad (2.13)$$

Hence,

$$\frac{dn_1}{dt} = -n_1\left(\frac{1}{\tau_1} + \sigma_{14}\frac{I}{h\nu}\right) + n_0\sigma_{01}\frac{I}{h\nu} + n_4\frac{\beta_{41}}{\tau_4} = 0 \tag{2.14}$$

By calculating n_1 from Eq. (2.12) and substituting it in Eq. (2.14), we obtain

$$\frac{n_4}{\tau_4}\left(1 - \beta_{41} + \frac{h\nu}{\tau_1\sigma_{14}I}\right) = n_0\sigma_{01}\frac{I}{h\nu} \tag{2.15}$$

The noise, defined as the number of photons per second emitted by the (4 → 0) radiative transition, can be estimated by

$$N\frac{n_4}{\tau_4}\beta_{40} = \left(1 - \beta_{41} + \frac{h\nu}{\tau_1\sigma_{14}I}\right)^{-1} N\sigma_{01}\beta_{40}\frac{I}{h\nu} \tag{2.16}$$

It turns out that the signal, defined as the total number of photons emitted by to the particle action, and the noise depend on the laser intensity in different ways. In particular, for low laser intensity, or more generally with low upconversion efficiency, signal and noise can be approximated by exploiting from Eq. (2.16), Eq. (2.7),Eq. (2.4) as

$$N\frac{n_4}{\tau_4}\beta_{40} = (N\tau_1\sigma_{01}\sigma_{41}\beta_{40})\left(\frac{I}{h\nu}\right)^2 \tag{2.17}$$

$$n_1(0)\eta_{\text{up}} = [n_1(0)\beta_{40}\tau_1\sigma_{14}]\,\frac{I}{h\nu} \tag{2.18}$$

On the contrary, in case of high upconversion efficiency, we have

$$N\frac{n_4}{\tau_4}\beta_{40} = N\sigma_{01}\frac{I}{h\nu} \tag{2.19}$$

and

$$n_1(0)\eta_{\text{up}} = n_1(0) \tag{2.20}$$

In order to obtain high upconversion efficiency with low laser intensity, it is necessary to choose suitable crystals, in which σ_{01} is as small as possible and $\tau_1\sigma_{14}$ is as large as possible. We have dealt with a model considering a cw laser but some interesting properties can be expected if a pulsed laser is used. This possibility will be discussed in chapter 4.

2.2. More interesting schemes

Some variations on the previous scheme can be realized. If level 4 relaxes assisted by phonons on a nearby level, or if level 4 is the lowest of the 5d, or if level 4 is a CT level[3], absorption may occur at a wavelength that can differ from that of emission, by even several tens of nanometers. Thus, both the emissions (4 → 0) and (4 → 1) can be collected and

---

[3] That have a remarkable Stokes shift

used as signal. In this case, the “effective upconversion efficiency” (Eq. (2.7)) becomes:

$$\eta_{\mathrm{up}} = \epsilon_{\mathrm{up}}\beta_{40}\sum_{j=0}^{\infty}(\epsilon_{\mathrm{up}}\beta_{41})^{j} + \sum_{j=1}^{\infty}(\epsilon_{\mathrm{up}}\beta_{41})^{j} = \left(\frac{\beta_{40}}{\beta_{41}} + 1\right)\left(\frac{1}{\beta_{41}\epsilon_{\mathrm{up}}} - 1\right)^{-1} \tag{2.21}$$

For each “cycle” of each ions one more detectable signal photon is released.

Actually, a more interesting scheme, involving photon avalanche process, is shown in Fig. (1.8)c on page 33. The second energy level 1 is equidistant (or almost equidistant) in energy from 0 and 2 levels, so cross relaxation (2,0)→(1,1) is very efficient. In addition, we assume a high branching ratio β_{32}. The particle excites ions of level 1, the laser promotes them to level 3 and they radiatively relax, in particular, to level 2. If the energy transfer process is efficient, each ion in level 2 with a nearby one in ground state are brought to level 1, where they are both ready to be promoted by the laser. In this case, for each cycle a detectable photon is released and another ion populates level 1 so that this recycling process may induce a signal light amplification. However, the noise increases at the same rate.

This model is more complicated to describe than that of the previous section. In particular, it depends on many parameters and different regimes can be achieved depending on the laser intensity. As the measurements performed in this work do not involve photon avalanche processes or it can be neglected, we do not discuss in detail this model. A system of equation describing this type of process can be found [40–42].

Now it is possible to envision the possibility of a detector based on IRQC. The total scintillation photon energy can be much higher than that of the incident particle while in modern RE scintillators it is at most 1/2.5 times less than that of the incident particle. However, in contrast to the advantage of a possible high light yield and low energy threshold, there might be the drawback of a long decay time of the signal, i.e., of the same order of τ_1.

Chapter 3

Cathodo- and radioluminescence of RE doped crystals in a wide optical band

In the previous chapters we have presented the IRQC concept and its possible application to the realization of a new class of particle/ionizing radiation detector. In the model we have proposed, the visible LY of the detector is proportional to the number of ions excited in a given low energy metastable level per unit amount of energy deposited in the crystal by the particle or by the ionizing radiation. The number of the excited ions can be estimated by measuring the number of photons emitted from this level per deposited energy unit[1], i.e., by measuring the infrared LY due to this low energy level. A large LY in the visible range requires that this intermediate level is efficiently populated by the incoming particle (or radiation) and its effective UP rate is large, as can be seen by inspecting Eq. (2.7).

Many processes contribute to the population of the low energy levels of RE doped crystals. Among them there are the direct excitation by the particle impact, the radiative and multiphonon relaxation from higher states, and maybe transitions induced optical phonons and even plasmons. However, these processes are poorly investigated.

A scant number of studies can be found in literature on the LY or on the population of these low RE energy levels by mean of energeticparticles. Interesting results have been found in the past in our laboratory [44]. A light yield LY $= (79 \pm 8) \times 10^3\,\mathrm{ph/MeV}$ at $\lambda \approx 1.03\,\mu\mathrm{m}$ at room temperature has been observed in a Yb:YAG 10% single crystal. Additionally, a light yield LY $= 120 \times 10^3\,\mathrm{ph/MeV}$ has been measured in powders of Eu-doped phosphors [45].

To our knowlegde, no articles provides the LY in mid-infrared range. Actually, these low RE energy levels are widely applied in optical devices, especially lasers, but have not found any applications in the particle detection realm because they have got long lifetimes and because the present detectors have low quantum efficiency in the infrared band.

---

[1] Without laser excitation that can reduce the number of emitting ions in the given level via the UP process.

For these reasons, an investigation of the infrared LY in different combinations of RE and host matrices of different concentration must be carried out. We also propose a new technique in order to estimate the LY with a good accuracy and efficiency even in mid-infrared range. We have built an experimental setup in which the crystal under investigation is excited by 70 keV electrons or x-ray and the emission spectrum is recorded from UV to mid-infrared band. The LY in visible range is estimated by comparing the visible emission to that of an another crystal whose LY is known. The infrared LY is also quantified from the recorded spectrum and the visible LY. This technique is optimized by studying two particular single crystals: Nd^{3+}:YAG and Tm^{3+}:YAG.

A further goal of this work is aimed at observing an enhancement of the visible cathodoluminescence when a laser is tuned to provide the UP of the ions in the first excited manifolds. Actually, even if the UP process has been extensively applied for optical devices, to the best of our knowledge, it has never been observed if produced by energetic particles or high energy radiation. Therefore, we have built one more experimental setup in order to prove the feasibility of this detection process. We have chosen to exploit an Er^{3+}:YAG single crystal because a suitable UP from its first excited state can be realized by adopting a tuned Ti:sapphire laser. However, we have to note that a detector with acceptable efficiency and noise is still far from being realized yet.

3.1. Apparatus

The aim of this section is to describe the experimental setup used to measure the LY and to analyze the emission spectrum of the sample. The technical features of the apparatuses and devices used in the experiment are briefly discussed in the present and next sections.

The experimental technique we developed consists in exciting the crystal under investigation with a pulsed or continuous beam of 70 keV electrons or x-rays. They are both produced or generated by exploiting a home made electron gun [46]. The block diagram of the experiment is shown in Fig. (3.1).

The crystal luminescence intensity in different optical ranges is selected by optical filters and is detected by suitable photodiodes (PDs). The emission spectrum is analyzed by CCD spectrometers and by a Fourier Transform infrared (FTIR) interferometer.

3.1.1 Electron gun

The electrons for the study of the impact excitation the crystals are delivered by a home-made electron gun (e-gun). The detailed description of th e-gun can be found in literature [46]. Here, we only recall its main features. The e-gun is located in a Pb shielded room because it is a strong source of stray X-rays. It can be operated at high voltage (H. V.) up to 100 keV by using a commercially available, d.c. voltage source (Spellman) in either continuous or pulsed mode. In the former one, it delivers a d.c. current with intensity up to 15 μA, whereas in the latter one it delivers electron bunches of several nC as short as 100 μs per pulse. The electron are released by thermionic effect be a Joule-heated, Tungsten filament. A pack of rechargeable cells, floated at H.V., powers the filament. The filament current controls the electron emission current. the released electrons are accelerated outside of a Wehnelt cylinder toward the closing flange in which a small opening allows electrons to impinge on the target crystal. Two magnetic coils are used as magnetic lenses to focus and deflect the electron beam. An additional coil, powered by a home made, a.c. generator, can be used to harmonically deflect the electron beam so as to achieve a pulsed electron injection regime by periodically crossing the exit opening. This opening also defines the spot size of the beam. In the pulsed regime, the repetition rate can be as high as 1 kHz. All the electrode system is contained in a sealed vessel that is evacuated to a residual pressure of $\approx 10^{-6}$ mbar.

A 2 mm hole drilled in a copper beam stopper mounted on the high vacuum side of the closing flange defines the maximum exploitable beam size. On the room-pressure side of the flange, a crystal holder flange is mounted. A 10 μm thick metal foil (either Tungsten or Tantalum), is sealed to the crystal holder. It is in mechanical and in electrical contact with the crystal and serves several purposes. It separates the high vacuum e-gun from the atmospheric pressure, screens the crystal from the light emitted by the hot filament of the e-gun, and, if Tungsten is used, it allows the electron beam to enter the crystal without loosing an excessive amount of energy. Moreover, when Tantalum is used, the foil stops electrons from reaching the crystal while itself becomes the source of the X-rays with which the crystal is irradiated. In both cases, the dielectric crystal is grounded by the metal foil connected to the $R = 1\,\mathrm{M}\Omega$ input resistance of an oscilloscope. The relative signal is termed beam stopper signal. Thus, the metal foils allows us to measure the amount of charge that has impinged on the crystal. The

A special flange with a sealed sapphire optical window has been built for the experiment in which an optic fiber let a laser to be shone sideways on the crystal.

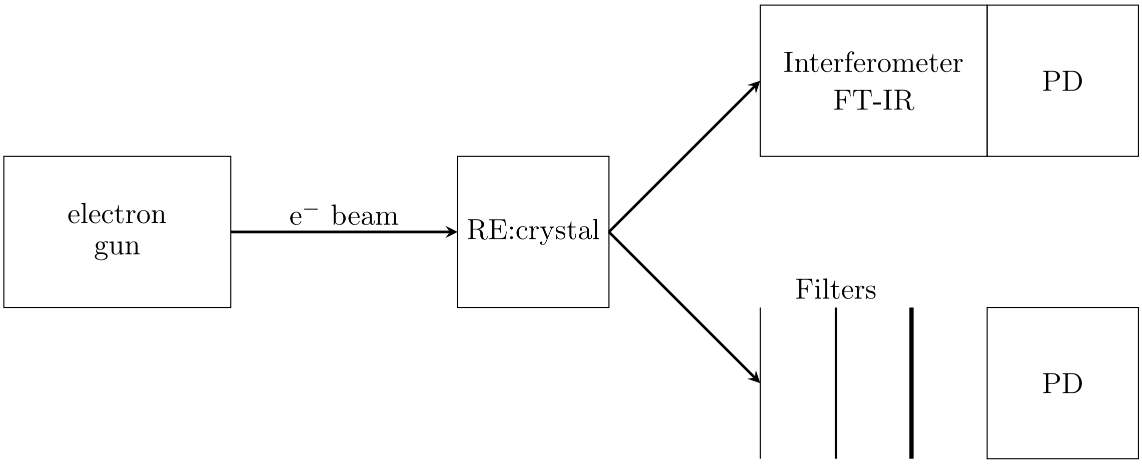

Figure 3.1: Block diagram of the experiment.

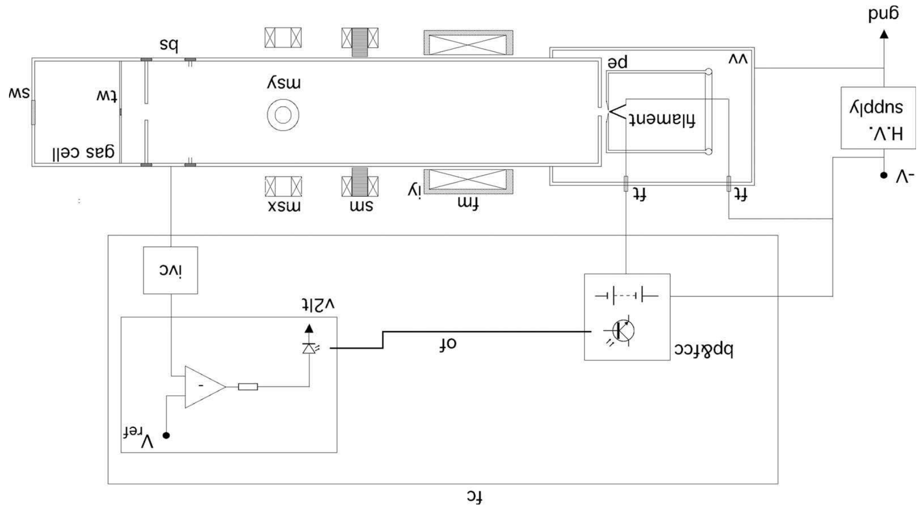

Figure 3.2: Block diagram of the electron gun assembly. Legend: vv= vacuum vessel, ft=high-voltage feedtrough, pe= Pierce electrode, fm= focusing magnet, iy= iron yoke, sm= magnets for the sweeping of the electron beam, msx, msy = magnetic stirrers for fine tuning of the x-y position of the electron beam center, tw= Ti window (not to scale) [46].

3.1.2 Optical filters

Several filters are available. They provide the simplest way to select a desired wavelength range. They can be mainly divided into two classes: the FB bandpass and FEL, FGL longpass. They are supplied by Thorlabs. Their typical trasmission curves are plotted in Fig. (3.3). The FEL and FGL filters are defined by their cut-in transmission wavelength, whereas the FB filters are designed by their center and full width at half maximum (FWHM).

3.1.3 PDs and amplifiers

Several types of PDs are exploited in order to analyze the luminescence in different optical bands, from the ultraviolet- to mid-infrared range. In Fig. (3.4) are shown the responsivity of the PDs. In particular, the Thorlabs Det36A and Det20C have been used in the photovoltaic mode. Their current output is linearly converted to a voltage signal by using a a transimpedance amplifier (Femto, mod. DPLCA200) with variable gain up to 10^9 V/A or it is integrated by a UA1 active integrator (or simply, charge amplifier) with a conversion factor of 0.25 mV/fC.

3.1.4 Spectrometers

Spectrometers have to be used in order to single out the individual lines of the luminescence. To this goal, owing to the wide wavelength range we wish to investigate, we used the following commercially available spectrometers.

- **Ocean Optics, mod. Red Tide USB650:** is a compact, fiber-based, silicon CCD spectrometer with 650 pixel resolution. Two models are available. The first one is set to record spectra in the range 200 to 850 nm. The second one is for the range 350 to 1000 nm. The integration time can be set up to one minute. Only the latter one has been calibrated in order to obtain a corrected spectrum.

- **Thorlabs, mod. CCS175:** is very similar to the previous spectrometers. It can record spectra in the range 500 to 1000 nm with accuracy ≈ 0.6 nm.

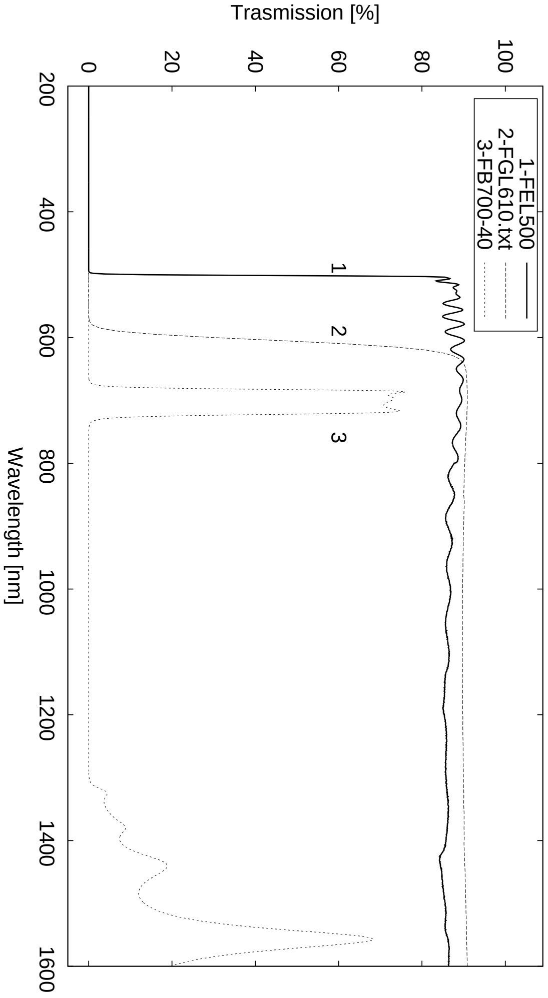

Figure 3.3: Typical trasmission curve of the used filters.

Table 3.1: Photodiodes features

PD	S1137-1010BQ[1]	Det36A[2]	C30723[3]	Det20C[2]	P7163[1]	P5968[1]
semiconductor[4]	Si(I)	Si(II)	InGaAs(I)	InGaAs(II)	InAs	InSb
Area [mm^2]	100.0	13.0	19.6	3.14	0.8	12.6

[1] Hamamatsu
[2] Thorlabs
[3] EG&G
[4] We label the PDs with the semiconductor type, and, sometimes with the tags (I) or (II).

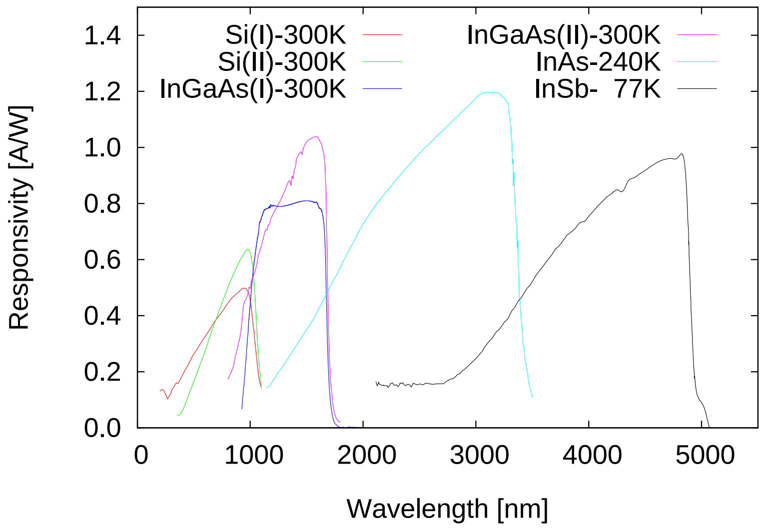

Figure 3.4: PD responsivities. They can be easily found in the literature. That of the InGaAs(I) is measured [47].

- **Ocean Optics, mod. NIRQuest512:** this fiber-based, InGaAs CCD spectrometer, that is thermoelectrically cooled down to −20 °C, is to be used in the range 900 to 1700 nm with a optical resolution ≈ 3 nm. The integration time can be set up to two minutes. It has not been calibrated.

- **Bruker, mod. Equinox 55:** This Fourier Transform infrared interferometer can be coupled with either a PD or a bolometer and allows the researchers to record emission or absorption spectra in the range 15798 to a few hundreds of cm^{-1} with maximum resolution $\approx 0.5\,\mathrm{cm}^{-1}$. Two techniques can be exploited in order to record a spectrum: the so-called rapid scan and step scan techniques. In the former one, the interferometer mirror makes continuous scans and up to four spectra can be obtained from each full forward-backward scan. The latter one can be used only for repetitive events. The moving mirror moves in discrete steps. At each step, the mirror is stopped and several signals are acquired in order to reduce the signal-to-noise ratio. This method finds application in study of the dynamics and kinetics of processes where high spectral and fast temporal resolution is necessary.

UV laser

As it is necessary to carry out spectroscopic measurements by optically exciting the crystals in order to compare the differences between electron impact and laser excitation, we have also used a commercially available Nd:YAG UV laser. It releases 8 ns long pulses at $\lambda = 266\,\mathrm{nm}$ at a maximum repetition rate of 0 Hz. The energy released by each pulse can be as high as 10 mJ.

3.2. Electron impact excitation studies

Two commercial single crystals, Nd^{3+}:YAG 1.1% by mol. (in the shape of a cylinder, 3 mm in diameter and 3.1 mm in thickness) and Tm^{3+}:YAG 4.4% by mol. (cylinder, 5 mm in diameter and 3 mm in thickness), are investigated as first samples in order to measure their infrared cathodoluminescence. They have been chosen for the large amount of literature with which our results can be compared. In particular, the Nd:YAG material is widely applied as a lasing medium for solid-state lasers.

3.2.1 Integral luminescence intensity measurements

The first goal is to measure the total intensity of the cathodoluminescence. This experiment is done by measuring the response of the PDs as a function of the charge impinging on the crystals. Different filters can be used to limit the wavelength band over which this measurement has to be carried out.

Linearity- First of all, it is necessary to verify that the level population is directly proportional to the energy released into the crystal by the particles at least in the low intensity region for two reasons: scintillators should work in a linear regime and the relative emission spectrum must not depend on the excitation intensity, if the LY has to be correctly evaluated.

The PD is mounted on a micrometrical translational stage in order to carry out measurements at several distances so that the solid angle subtended by the crystal at the PD can be determined in view of the estimation of the LY.

When the electron gun is used in pulsed mode, both the transimpedance amplifier output and the beam stopper signal are simultaneously acquired with a storage oscilloscope. For each settings of the injected charge, one hundred signals are fetched from the scope to a PC and numerically averaged offline in order to improve the signal-to-noise ratio.

We want to know the amount of charge generated in the PD in response to the luminescence light as a function of the charge impinged on the crystal. Let $i_d(t)$ be the current in the PD, $V_d(t)$ be the detector signal, and let $V_{\mathrm{bs}}(t)$ be the beam stopper signal. Typical signals are shown in Fig. (3.5). Let moreover $R_0 = 1\,\mathrm{M\Omega}$ be the scope input resistance. The total amount of charge produced in the crystal Q'_d can be related to the total charge Q_d flown in the input resistance of the oscilloscope

$$Q'_d = \int i_d \,\mathrm{d}t = \int \frac{V_d(t)}{G}\,\mathrm{d}t = \frac{R_0}{G}\int \frac{V_d(t)}{R_0}\,\mathrm{d}t = \frac{R_0}{G} Q_d \tag{3.1}$$

where the integrals are performed over the time interval separating two successive pulses[2].

Similarly, the total charge impinged Q_{bs} on the crystal during a pulse is obtained by

---

[2] The integrals are calculated after the offset due to the dark current has been subtracted.

integrating the beam stopper signal

$$Q_{\mathrm{bs}} = \int \frac{V_{\mathrm{bs}}}{R_0}\,\mathrm{d}t \tag{3.2}$$

The pulse repetition rate is set so as to ensure that during the time T_0 between two successive pulses, the excited RE ions can relax and crystal becomes electrically neutral again.

The results of the measurements of Q_d as function of Q_{bs} for Tm^{3+}:YAG are shown in Fig. (3.6) and presented in Tab. (3.4). Similar results are also obtained for the Nd doped crystals. The direct proportionality between the amount of charge impinging on the crystal and the intensity of the induced luminescence is very well obeyed. It is also verified in different optical ranges with the Si(II), InGaAs(II), InAs and InSb PDs, using suitable optical filters in order to isolate one or few specific sets of transitions.

In the case of Si(II) detector, the frequency of the electron beam pulses is set to 100 Hz as the signal due to the emission in 200-1100 nm range decays quite rapidly (within a few hundreds of μs (Fig. (**??**)). For all remaining PDs, which are more sensitive in the infrared region, where some of the fluorescence stems from longer lived states, the pulse repetition rate was lowered to 30 Hz (Fig. (**??**)).

The linearity measurements can be even performed with the e-gun in continuous mode. The beam stopper current I_{bs} and the potential difference V_d generated by the detector are measured by two multimeters. This method is faster and as good as the previous but no pieces of information on the lifetimes of the excited ion levels can be gathered. The results for the Nd^{3+}:YAG crystal are presented in Tab. (3.5). The results obtained in this way with Tm^{3+}:YAG are similar and the linearity is also proved in all investigated optical

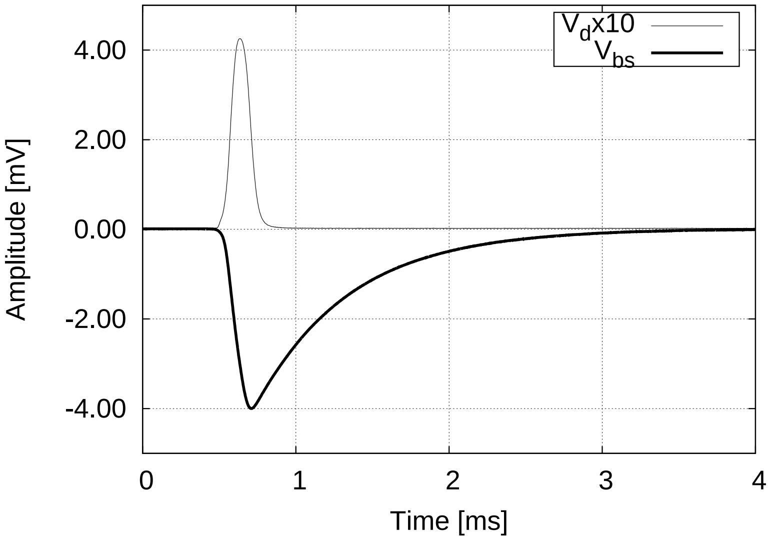

Figure 3.5: Typical PD and beam stopper signals. Si(II) response amplificated with 10^7 V/A, to the Tm:YAG luminescence, selected with FB450-40 filter.

ranges.

Estimation of the LY- The values we have obtained so far can be useful for the emission spectrum analysis. We suppose to use the electron gun in pulsed mode. The time-averaged, emission power spectral density $\langle P(\lambda)\rangle_t$, owing to the previously assessed linearity property, is directly proportional to the average charge injected in the crystal during each pulse[3]

$$\langle P(\lambda)\rangle_t d\lambda = k\frac{Q_{\rm bs}}{T_0}S(\lambda)d\lambda \tag{3.3}$$

in which $S(\lambda)$ is the spectrum, T_0 is the time interval between two successive pulses, and k is the proportionality constant. The LY per unit wavelength is obtained as

$$LY(\lambda)d\lambda = \left(\langle P(\lambda)\rangle_t \frac{\lambda}{hc}\right)\frac{T_0}{VQ_{\rm bs}}d\lambda = k\frac{\lambda}{hc}S(\lambda)d\lambda \tag{3.4}$$

in which V is the electron acceleration potential, $VQ_{\rm bs}$ is the energy of the charge pulse.

The charge carriers generated in the PD per pulse can be expressed as a double integral over wavelength and time

$$Q'_d = \int\int_{t_0}^{t_0+T_0} \frac{d\Omega}{\Omega}P(\lambda,t)D(\lambda)T(\lambda)\,\mathrm{d}t\,\mathrm{d}\lambda = T_0\int\frac{d\Omega}{\Omega}\langle P(\lambda)\rangle_t D(\lambda)T(\lambda)\,\mathrm{d}\lambda \tag{3.5}$$

Here, $d\Omega/\Omega = A/4\pi d^2$ is the solid angle subtended by the crystal at the PD with area A located at a distance d from the crystal, $T(\lambda)$ is the transmission of a the optical filter used, and $D(\lambda)$ is the PD responsivity.

---

[3] This assumption is generally only valid for low injected energy.

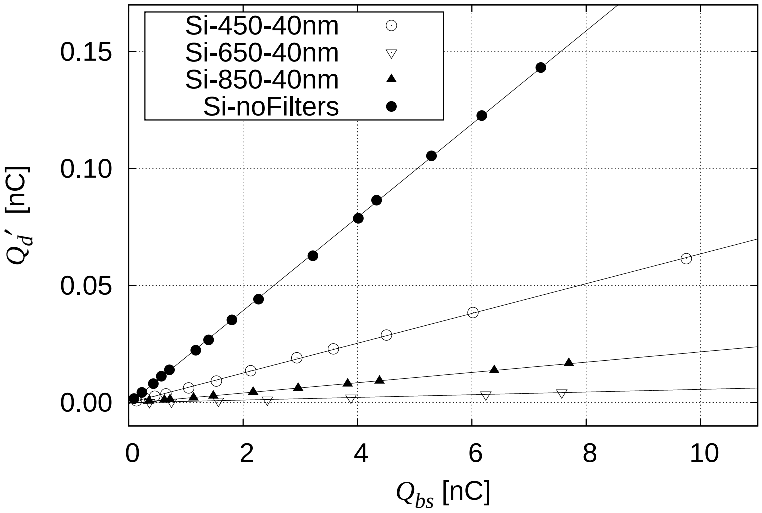

Figure 3.6: Tipical dependence of generated charge carriers in PD vs the pulse beam charge for different filters located in front of the PD.

Substituting Eq. (3.5) in Eq. (3.1), one obtains:

$$Q'_d = \int k \frac{A}{4\pi d^2} Q_{\mathrm{bs}} D(\lambda) T(\lambda) S(\lambda) d\lambda \tag{3.6}$$

so

$$k = \frac{Q'_d}{Q_{\mathrm{bs}}} \frac{4\pi d^2}{A} \left[\int D(\lambda) T(\lambda) S(\lambda) d\lambda \right]^{-1} \tag{3.7}$$

Substituing k in Eq. (3.4):

$$LY(\lambda) d\lambda = \frac{\lambda}{hc} \frac{Q'_d}{Q_{\mathrm{bs}}} \frac{4\pi d^2}{VA} \frac{S(\lambda) d\lambda}{\int D(\lambda) T(\lambda) S(\lambda) d\lambda} \tag{3.8}$$

As the absolute distance d of the detector from the PD is only given with an unknown offset x_0, the ratio (Q'_d/Q_{bs}) is estimated at several distances $x = d - x_0$ by a linear fit of Q'_d vs Q_{bs}. In the point source approximation, the parameter $a = Q_d d^2/Q_{\mathrm{bs}}$ is estimated by the fit

$$\frac{Q'_d}{Q_{\mathrm{bs}}}(x) = \left(\frac{Q'_d}{Q_{\mathrm{bs}}} d^2 \right) \frac{1}{(x + x_0)^2} = \frac{a}{(x + x_0)^2} \tag{3.9}$$

with a and x_0 as free parameters. The values of the fit for Nd:YAG and TmYAG are reported in Tab. (3.5), Tab. (3.4) and the correctness of this approach can be observed by inspecting Fig. (3.7) obtained for Tm:YAG. Similar results are obtained for Nd:YAG although the e-gun was used in continuous mode.

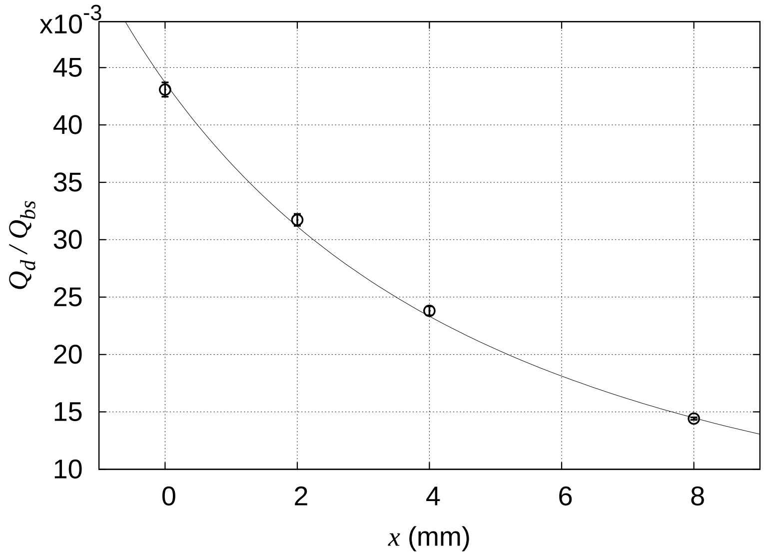

Figure 3.7: Typical dependence of the $Q_d/Q_b s$ vs the relative distance. In particular, the measurements are performed with Si(II) PD exciting the Tm:YAG.

Hence, the integrated LY in the range $[\lambda_i, \lambda_f]$ is:

$$LY(\lambda_i, \lambda_f) = \left[\frac{1}{Vhc} \frac{4\pi a}{A \int D(\lambda) T(\lambda) S(\lambda)\, \mathrm{d}\lambda} \right] \int_{\lambda_i}^{\lambda_f} S(\lambda) \lambda\, \mathrm{d}\lambda \tag{3.10}$$

Once the spectrum in a broad optical band is obtained and the term in the square brackets is estimated with any combinations of the PDs, optical filters and amplifiers[4], LY in each range can be calculated.

Nevertheless, in this way, LY may be affected by a large sistematic error that is difficult to estimate because the assumption that the energy injected in a pulse is VQ_{bs}, may be not correct. First of all, the deposited energy has a strong dependence on the Titanium foil thickness that is eroded in time by the electron beam.

Secondly, it is not sure that all Q_{bs} electrons release their energy into the crystal. Some of them may not properly be focused and may then collide directly against the flange. Some others may be backscattered by the crystal towards the foil where they are stopped and collected by the flange. Moreover, the crystal composition and size can also have an influence on the measurements of the effective charge injected in to the crystal.

It must be noted that all estimations of LY obtained by using Eq. (3.8) with different PDs are affected by the same systematic error. All the values differ from the true one by a proportionality constant that is the same proportionality constant linking VQ_{bs} and the true value of the injected energy. As a consequence, the estimation of the "absolute" LY value will be done in next section using a formula similar to Eq. (3.8) but the measurements are those performed by using th x-ray excitation produced with the electron beam. Unfortunately, the production efficiency of x-ray is of the order of 0.1%, so the resulting luminescence is much weaker than that obtained by electron impact. Hence, cathodoluminescence is used to obtain an accurate emission spectrum, in particular when the spectra are obtained with the FTIR technique, whereas x-ray excitation provides avery accurate value of LY once the spectrum in a broad band is obtained.

Without a common, intense enough emission line, it can be difficult to merge the spectra recorded in different wavelength ranges with different spectrometers. This problem can be overcome by using Eq. (3.8). For each spectrum, a "pseudo" $LY(\lambda)$ in the same range can be evaluated by using a careful choice of PDs and optical filters. In particular, it is necessary that $D(\lambda)T(\lambda)$ are zero outside the range of the given spectrum. In this way, it is possible to calculate the integral in Eq. (3.8). As discussed before, all the LYs calculated in different spectral regions in this way differ from the true one by the same proportionality constant and it is thus easy to merge them together. In other words, spectra recorded in different optical bands are merged by normalizing each one to the absolute intensity value.

Using the electron gun in continuous mode, the Eq. (3.8) becomes

$$LY(\lambda)d\lambda = \frac{1}{G}\frac{\lambda}{hc}\frac{V_d}{I_{\text{bs}}}\frac{4\pi d^2}{VA}\frac{S(\lambda)d\lambda}{\int D(\lambda)T(\lambda)S(\lambda)d\lambda} \tag{3.11}$$

Let us define $a = V_d d^2/(I_{\text{bs}} \cdot G)$. It is evaluated in a similar way as in pulsed mode. The a parameter values for Nd:YAG obtained by using Si(II) detector in both pulsed and continuous operating modes of the e-gun, are equal within 5%.

---

[4] Obviously the formula is valid only for transimpedance amplifier, but for other type of amplifier it can easily be modified

3.2.2 Lifetimes

When the electron gun is used in pulsed mode, information on the temporal evolution of the emission can be obtained by simultaneously acquiring the beam stopper and detector signals.

Let consider the beam stopper signal $V_{\mathrm{bs}}(t)$ fetched by the oscilloscope. It is the response of a series RC circuit to the electrons injection $e(t)$, where $R_0 \approx 1\,M\Omega$ is the impedance of the oscilloscope and C is the effective capacitance due to Faraday cup and cable. The electronic time constant $\tau_{\mathrm{bs}} = RC$ is estimated with a good accuracy by fitting an exponentially decaying function to the final part of the signal. Typically, ($400\,\mu\mathrm{s} \leq \tau \leq 600\,\mu\mathrm{s}$), depending on the beam stopper used. $e(t)$ can be obtained solving numerically the following equation

$$V_{\mathrm{bs}} + \frac{1}{\tau_{\mathrm{bs}}}\frac{dV_{\mathrm{bs}}}{dt} = e(t) \tag{3.12}$$

In fig **??**a beam stopper signal and the computed $e(t)$ are shown.

Now, let us consider the PD signal generated by the emission from only one level with lifetime τ, selected thanks to an appropriate optical filter. Except by a proportionality constant, the light intensity emitted by the crystal is described by the following equations

$$I + \frac{1}{\tau}\frac{dI}{dt} = e(t) \tag{3.13}$$

provided that the time needed for electrons to excite the crystal and to be then collected by the Faraday cup is much less than the luminescence characteristic time, as it is reasonable to assume. If the signal is produced by many transitions of by many processes, such as energy transfer, the previous equation has to be modified.

A similar discussion for the beam stopper signal is valid for the PD signal, leading to

$$V_d + \frac{1}{\tau_d}\frac{dV_d}{dt} = I(t) \tag{3.14}$$

According to Eq. (3.14), the time constant τ_d can be estimated fitting an exponential decaying function to the final part of V_d when this signal is generated with the 50 ns short pulse of a Q-switched laser diode, whose emission at ≈ 900 nm makes this measurement possible for all different PDs.

In order to make measurements of lifetime, the response time of the electronics must be kept as small as possible. Therefore, owing to their very large output capacitance, the PDs are always amplified by the transimpedance amplifier whose output impedance is very low and whose bandwidth is such as to add only $\approx 3\,\mu\mathrm{s}$ to the signal time constant. For the same reason, no charge amplifier is used for lifetime measurements as its integration constant $\approx 450\,\mu\mathrm{s}$.

The temporal evolution of $V_d(t)$ of an emission due to a transition with a single time constant τ is numerically evaluated by simultaneously solving Eq. (3.12), Eq. (3.13), and Eq. (3.14), and adjusting the value of τ until the computed signal waveform agrees with

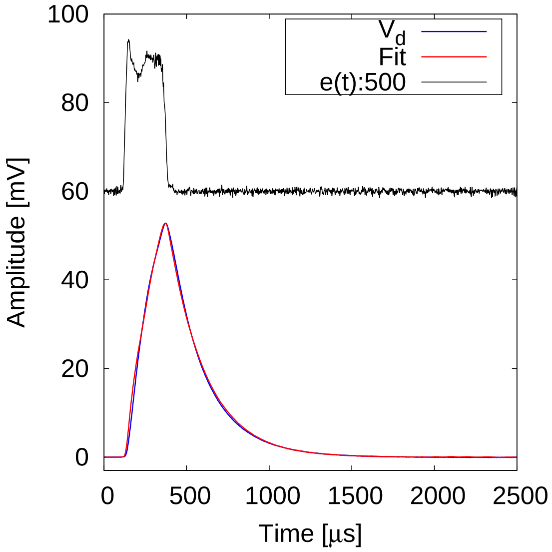

Figure 3.8: Experimental (blue) and simulated (red) V_d signal, and injection pulse (black) $e(t)$ obtained for the infrared emission of Nd:YAG.

the measured one.

A similar procedure can be followed also in the case the signal were due to several transitions with different lifetimes by suitably modifying the rate equations. We have to note the length of the electron pulse is the most important factor that limits the accuracy of this method.

The results of the procedure adopted to derive the signal shape due to infrared emission are shown in Fig. (3.8) for Nd:YAG 1.1% by mol. We obtained lifetime $\tau = (224 \pm 10)\,\mu$s, in agreement with the $228\,\mu$s reported in literature [48].

3.2.3 Emission spectra acquisition

In order to record spectra in the visible and near infrared regions we used the e-gun in the continuous mode. Several μA of $70\,keV$ electrons excite the crystal, whose luminescence is collected by an optical fiber connected to the CCD spectrometer. In particular, Redtide 650 (I) ocean optics and Thorlabs CCS175 spectrometers provide a calibrated spectrum from 350 nm to 1000 nm Fig. (**??**).

For the near- and mid-infrared region we used the FTIR interferometer Bruker Equinox 55. In the case of the Nd sample, the e-gun is used in the pulsed mode delivering ≈ 10 nC at 70 keV per pulse at 200 Hz repetition rate and the interferometer is operated in step-scan mode. In order to improve the signal-to-noise ratio, a few spectra are averaged together. In Fig. (3.9) we report the average spectrum for Nd, recorded with a resolution of $4\,\mathrm{cm}^{-1}$ using the InGaAs (I) PD. The spectrum is corrected by taking into account the spectral responsivity of the detector. We have also recorded a spectrum with the InSb PD in order to investigate a band more extended toward the infrared region, as shown in Fig. (3.10). We can observe that Nd does not show any detectable emission for $\tilde{\nu} \lesssim 6800\,\mathrm{cm}^{-1}$. The broad emission at $\tilde{\nu} \approx 2000\,\mathrm{cm}^{-1}$ is an an artifact due to the thermal emission of the interferometer casing.

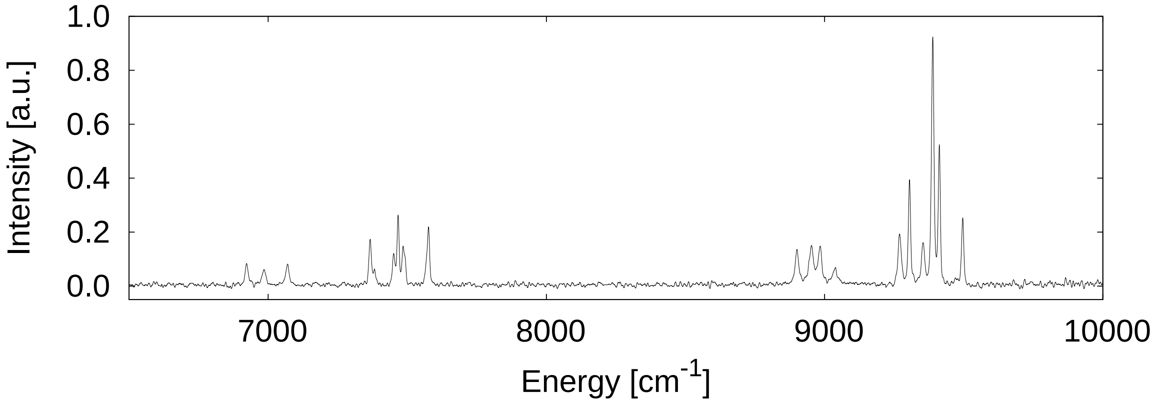

Figure 3.9: Nd:YAG emission spectrum recorded with InGaAs (I) PD.

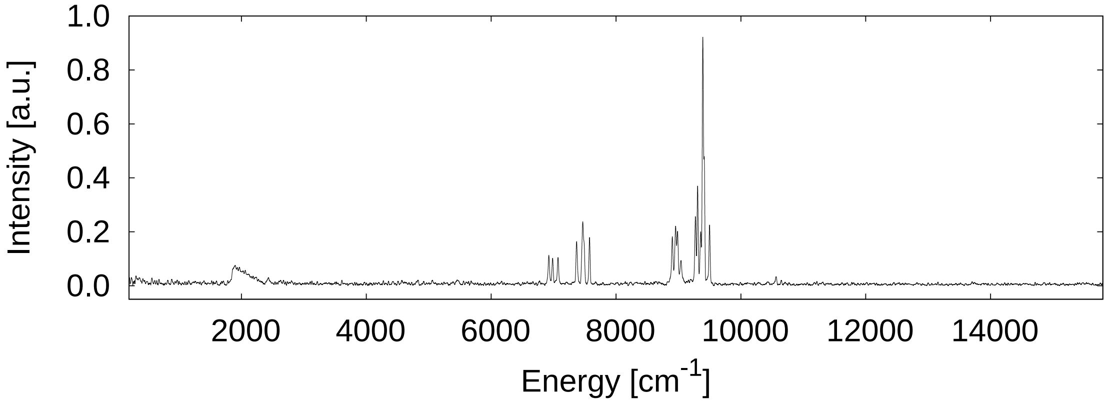

Figure 3.10: Nd:YAG emission spectrum recorded with InGaAs (I) PD.

For the Tm^{3+}:YAG sample we used the e-gun in continuous mode in order to operate the interferometer in the rapid-scan mode with InGaAs or InAs PDs connected to the charge amplifier even though its time constant is quite large. Although the noise is higher with this procedure, it is possible to acquire a huge number of spectra in a limited time that are averaged together so that the noise level is reduced to an acceptable level. In Fig. (3.11) we show the spectra obtained with both detectors and corrected by the relative responsivities.

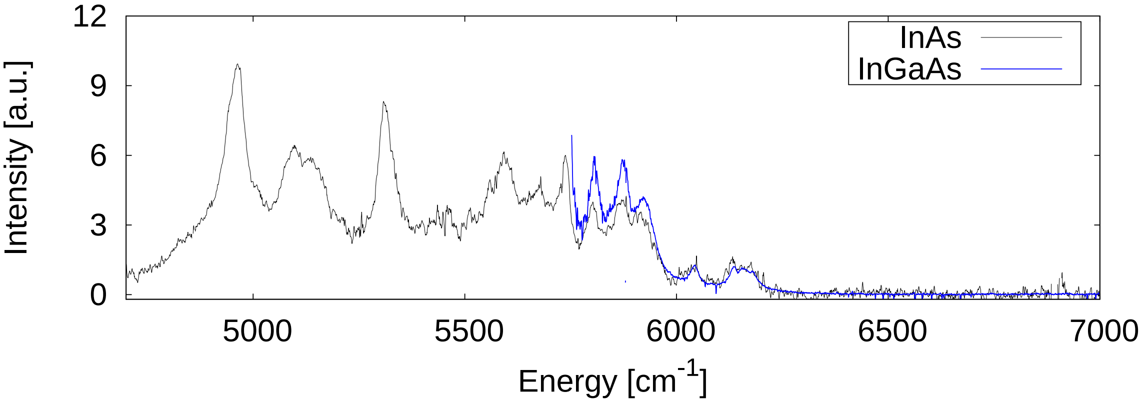

Figure 3.11: Infrared Tm:YAG spectra obtained with different PDs. Black curve: InAs. Blue curve: InGaAs.

3.2.4 Spectra merging and lines identification

In order to have a spectrum in a broad band we have to merge spectra obtained in narrower ranges with different spectrometers and PDs. The procedure is quite cumbersome and we will describe it for the different crystals.

For both Nd and Tm samples the spectra recorded with the two Redtide spectrometers are merged by normalizing them to the common, most intense and most energetic transition.

Nd

In order to merge the visible and near-infrared spectra of Nd, the common transition to be used is located at $\lambda = 400\,\mathrm{nm}$. The error done by neglecting the wavelength dependence of the spectrometer efficiency in the wavelength range below 300 nm is negligible because the more energetic transitions, i.e., those for $(260 \leq \lambda \leq 300)\,\mathrm{nm}$, are very weak, as confirmed by the analysis of the Q_d/Q_{bs} measurements performed with UV optical filter

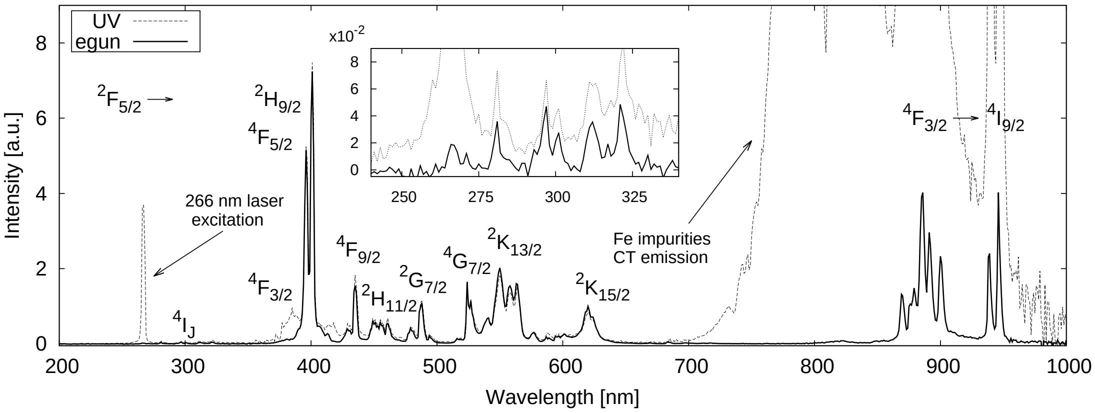

Figure 3.12: Nd:YAG electron and UV excitation emission spectra from 200 to 1000 nm.

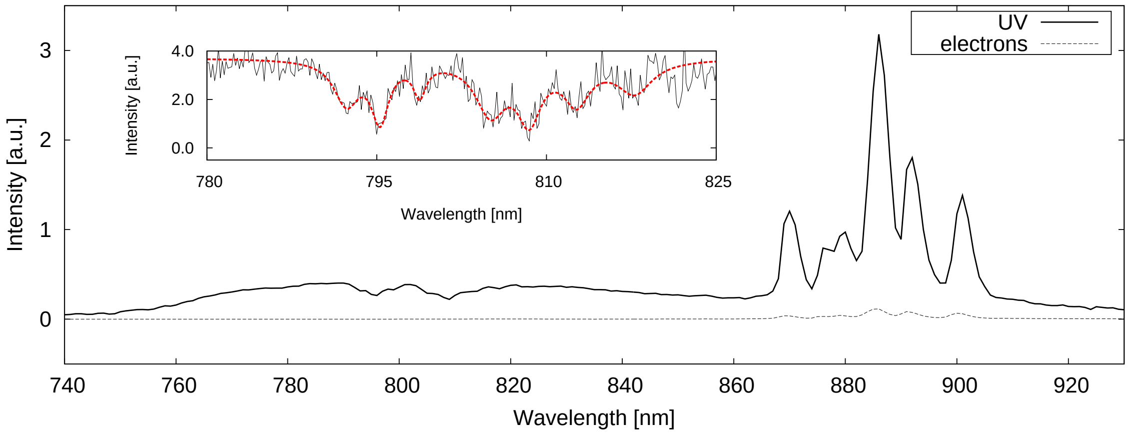

Figure 3.13: Magnification of Fig. (3.12).

In order to merge the visible spectra obtained with the Redtide spectrometers with the infrared spectrum obtained with the FTIR interferometer coupled with the InGaAs(I) PD, we use Eq. (3.8) because they do not share any common transitions. In order to do so, we need to know the values of the a parameter for the SI(II) detector in the the range 350−1000 nm, $a_{Si}(350-1000)$ and and for detector InGaAs(II) in the range 1000−1600 nm, $a_I(1000-1600)$. The latter one has been directly measured. The former is calculated starting from the a_S value measured in the optical range of the Si(II) PD, $a_{Si}(350-1100)$.

Unfortunately, the required $a_{Si}(350-1000)$ value and the measured $a_{Si}(350-1100)$ are different because a large emission is observed between 1000 and 1100 nm. To solve this problem, we estimate the $LY(\lambda)$ in the 1000-1100 nm range by using Eq. (3.10) from the InGaAs PD measurements. The value of $a_{Si}(1000-1100)$ can be deduced from the InGaAs LY because the LY itself is detector independent

$$\frac{a_{Si}(1000-1100)}{A_{Si}\int_{1000}^{1100} D_{Si}(\lambda)S_F(\lambda)\,\mathrm{d}\lambda} = \frac{a_I(1000-1600)}{A_I\int_{1000}^{1600} D_{InGaAs}(\lambda)S_F(\lambda)\,\mathrm{d}\lambda} \tag{3.15}$$

in which S_F is the spectrum recorded with the FTIR interferometer.

Now, it is a simple matter to deduce

$$\begin{aligned} a_{Si}(350-1000) &= a_{Si}(350-1100) - a_{Si}(1000-1100) \\ &= a_{Si}(350-1100) - a_I(1000-1600)\frac{A_{Si}\int_{1000}^{1100} D_{Si}(\lambda)S_F(\lambda)\,\mathrm{d}\lambda}{A_I\int_{1000}^{1600} D_I(\lambda)S_F(\lambda)\,\mathrm{d}\lambda} \end{aligned} \tag{3.16}$$

Now, it is possible to obtain the spectrum between 200 and 1600 nm (or even, 4500 nm) that are shown in Fig. (3.15)

In order to validate the previous procedure, we can also do the following. The parameter $a_{Si}(350-1000)$ can be also directly measured using an appropriate optical filter or can be estimated by the comparing signals obtained with different pairs of filters, one of which must not be opaque between 1000 and 1100 nm.

The ratio V_d/I_{bs} relative to different optical filters is measured Tab. (3.5). An equation similar to Eq. (3.6) can be obtained with the electron gun in continuos mode

$$\frac{V_d}{I_{\mathrm{bs}}} = c \int D(\lambda)T(\lambda)S(\lambda)\,\mathrm{d}\lambda \tag{3.17}$$

Once the integral for each filter is calculated using the previously merged spectra, the measured V_d/I_{bs} values vs the corrisponding integrals in Eq. (3.17) should lie on a straight line through the origin[5]. The goodness of the fit ($c = 16.29 \pm 0.12$ 0.7%) Fig. (3.14) proves the correctness of the spectrum we obtained in this way.

As the transitions above 700 nm originate from the same ${}^4\mathrm{F}_{3/2}$ manifold, as it will be discussed in the next section, the spectrum obtained with particle excitation should be equal to that obtained by laser excitation. This is actually confirmed by comparing our spectrum with literature result [48].

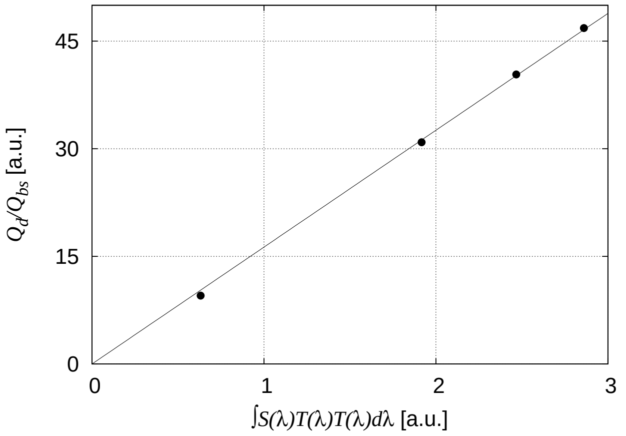

Figure 3.14: Linearity of Q_d/Q_{bs} vs the integral of the r.h.s. of Eq. (3.17).

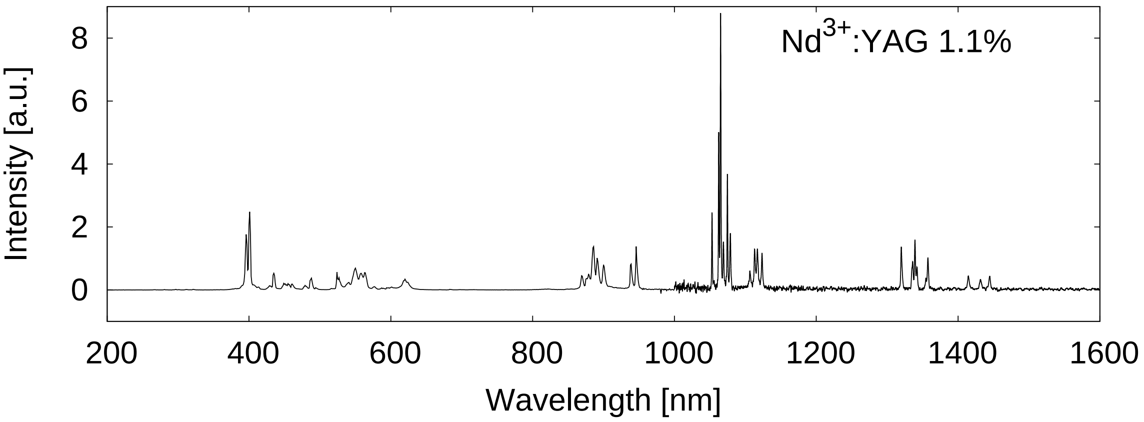

Figure 3.15: Nd:YAG calibrated emission spectrum.

---

[5] The measurement performed with FB1064-10 filter are not considered in this analysis because its transmission curve is affected by a very low accuracy, that is inherited by the computed integral.

Tm

In this case, the common transition to be used in order to normalize the spectra obtained by the two CCD spectrometers and that are to be merged occurs at 350 nm. As there is only one more line at 290 nm, which is observed with one spectrometer only, we assume that the spectral sensitivity of the spectrometers is roughly constant between 290 and 350 nm. In any case, the 290 nm line is so weak that its contribution to the overall intensity of the spectrum is negligible.

On the other hand, in order to merge this visible spectrum with the infrared one obtained with the FTIR interferometer, we used the same procedure leading to Eq. (3.10), previously described for Nd.

However, in this case the required parameters can be directly measured with both the Si(II) and InAs PDs because there are no lines in the spectrum between 1000 and 1100 nm.

The infrared spectrum obtained with the FTiR interferometer is quite noisy. Owing to the absence of relatively intense lines in the 900-1500 nm, we use the spectrum provided in the 900-1600 nm range by the InGaAs CCD spectrometer because it is much less noisy, as shown in Fig. (3.17). The complete spectrum is shown in Fig. (3.18).

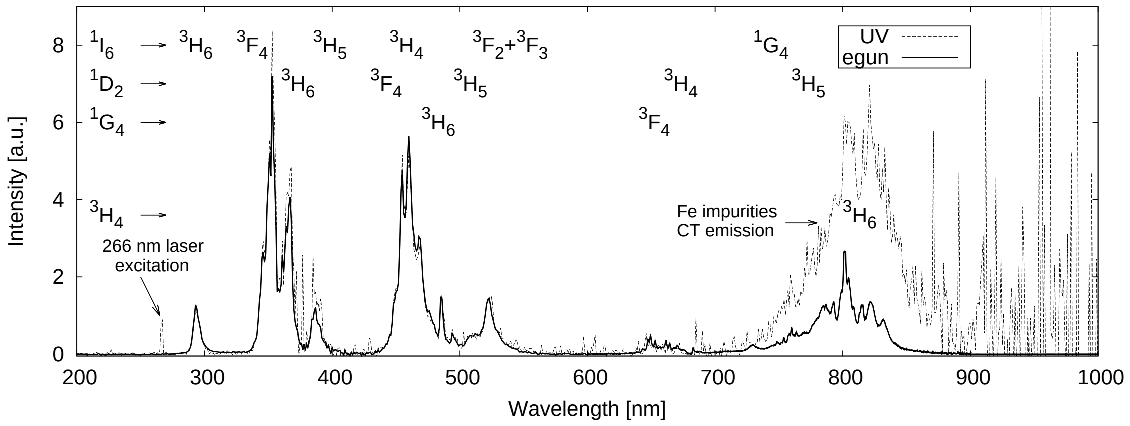

Figure 3.16: Tm:YAG electron and UV excitation emission spectrum from 200 to 1000 nm.

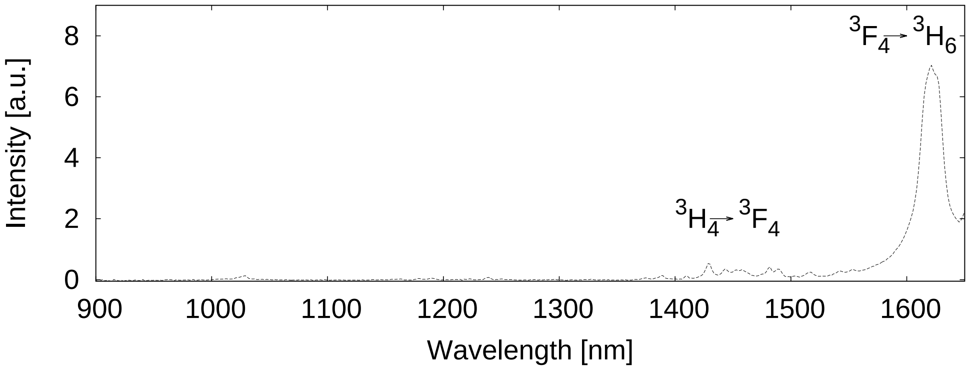

Figure 3.17: Tm:YAG emission spectrum recorded with ocean optics NIR512.

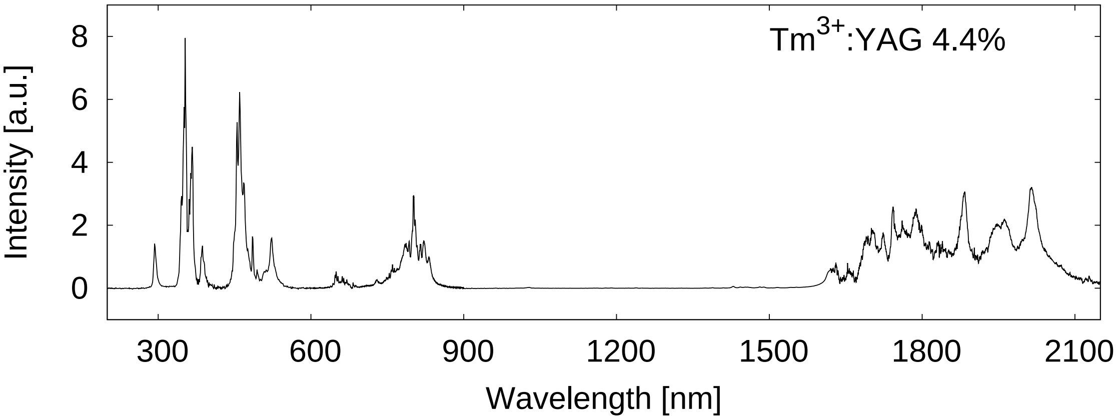

Figure 3.18: Tm:YAG correct emission spectrum.

3.2.5 Identification of the radiative transitions

The identification of the radiative transitions is mainly accomplished by the locating the wavelengths in the spectrum. We consider only those levels for which the non-radiative multiphonon relaxation rate is negligible [6]. A measure of the lifetime of a transition can be used in order to resolve possible ambiguities because the lifetimes of the manifolds can be found in literature. In addition, the high-power pulse of the 266 nm Nd:YAG laser can used in order to selectively populate a high energy level to observe its luminescence.

---

[6] eq? For the YAG, $C = 9.7 \cdot 10^7\,\mathrm{s}^{-1}$ and $\alpha = 3.1 \cdot 10^{-3}\,\mathrm{cm}{-1}$, with effective energy phonon $700\,\mathrm{cm}^{-1}$ [49]

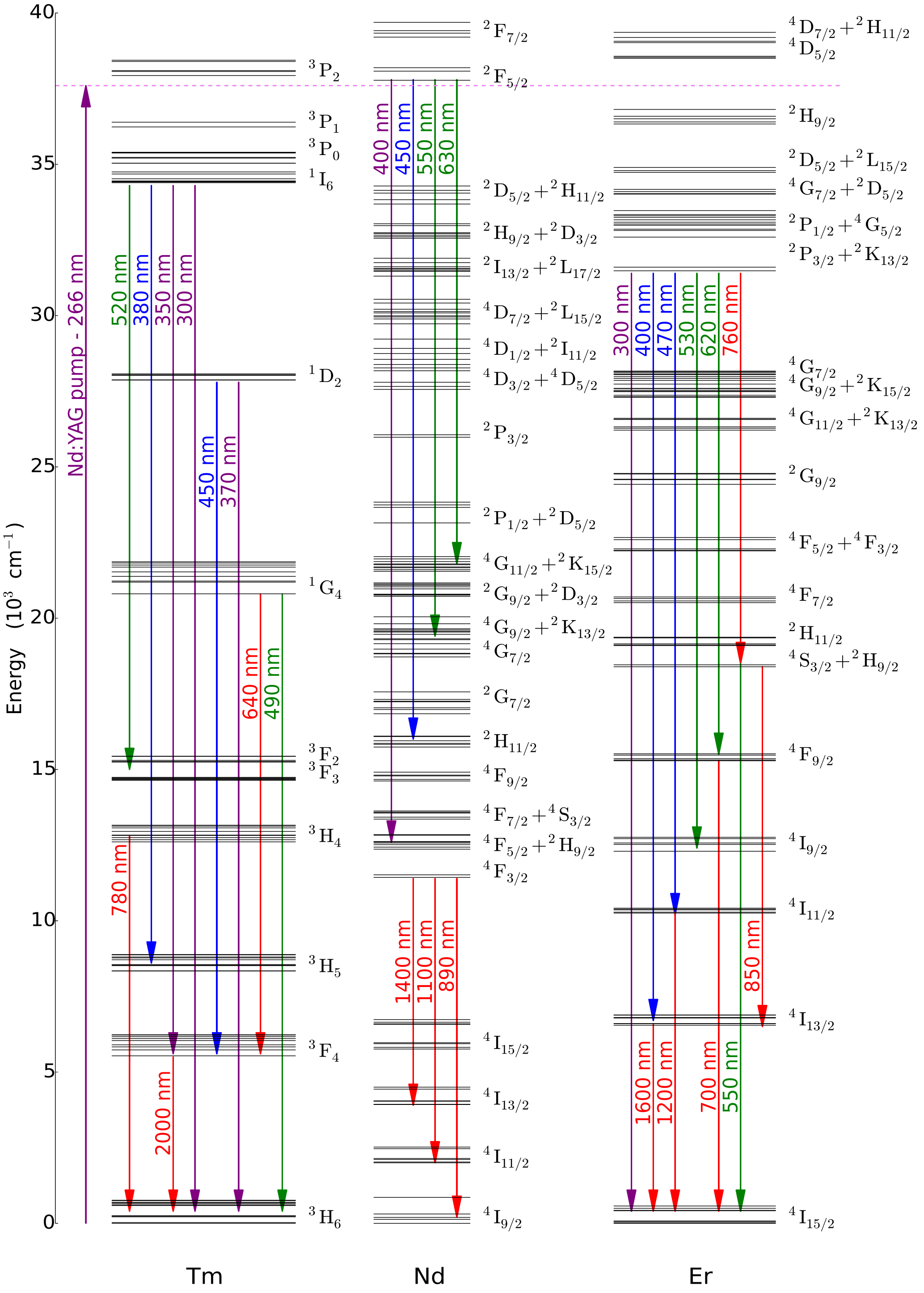

Figure 3.19: Energy level structure and more intense emissions observed of Tm:YAG, Nd:YAG, Er:YAG [50].

Nd

Owing to the high effective energy of the phonons of the matrix, only three manifolds (^{2}F(2)$_{5/2}$,^{2}P$_{3/2}$,^{4}F$_{3/2}$)[7] are expected to radiatively decay with lifetimes 3.02 μs, 0.32 μs, and 220 μs, respectively. For these manifolds the multiphonon relaxation rate is estimated to be at least one hundred times less than radiative relaxation rate [49].

Each of the twentyeight lines in infrared region (see. Fig. (3.15)) are associated to a transition from one Stark level of ^{4}F$_{3/2}$ manifold to one of ^4I_J with $J = 9/2$ for 850-950 nm range, $J = 11/2$ for 1040-1110 nm, $J = 13/2$ for 1350-1450 nm. The emission towards the ^{4}I$_{15/2}$manifold, expected at about 1800 nm, is buried in the noise because of its very low branching ratio (about 0.6%). In addition, the spectrum is very similar to that obtained by directly exciting the ^{4}F$_{3/2}$ manifold with a light source [48,51] and using Si(II) detector coupled with FEL1000 filter, a lifetime of $\approx 224\,\mu$s is estimated, thereby confirming the identification.

Since the emission from the ^{2}P$_{3/2}$ manifold occurs almost totally in the infrared range [49], we can deduce that it is very little if not excited at all.

The visible cathodoluminescence spectrum well agrees with the literature results obtained with Nd^{3+}:YAG sample doped between 0.1-6% by mol. and excited with 15 keV electrons at 300 K and 77 K [52], with samples excited by ^{239}Pb and ^{241}Am α particles [53,54], respectively, and with low temperature ($T = 8$ K) samples excited with 192 nm synchrotron radiation [55], In particular, Ning *et al.* [55], owing to the high resolution of their experiment, are able to ascribe the visible emission to the ^{2}F(2)$_{5/2}$ manifold. We use this result as a benchmark. However, to our knowledge, the first calibrated spectrum in the very broad range 200 to 1700 nm (or, even, 5000 nm), obtained with particles excitation, is presented in this work. Finally, we stress the fact that the emission in the visible range is too fast in order to measure its lifetime via the signal time evolution.

By referring to the level scheme shown in Fig. (3.22), a physical model can be cast to interpret the data [55], The e-h pairs generated in the crystals yield their energy to the Nd^{3+} ions, thereby exciting them to the 5d levels. These levels relax to those of the ^{2}F(2)$_{5/2}$ manifold via multiphonon relaxation by cascading through the lowest 5d level and the ^{2}F$_{7/2}$ manifold because only four phonons are required to bridge the energy gap.

The mechanisms that populate the ^{4}F$_{3/2}$ manifold are more complicated. First of all, it is necessary to understand how large is the fraction of population due to the relaxation from the ^{2}F(2)$_{5/2}$ manifold. This piece of information can be obtained by exciting the crystal with the 266 nm laser. In this way, ^{2}F(2)$_{5/2}$ manifold is directly populated and the resulting infrared luminescence due to the ^{4}F$_{3/2}$ manifold can be observed.

Fig. (3.12) shows a similar visible emission due to UV- and electrons excitation. The small differences in the two spectra may arise because of the difference of the volumes excited either by photons or particles. Actually, electrons are stopped in the first few hundreds of μm of the crystal, whereas the laser excites the whole crystal volume.

---

[7] All the other emissions are quenched or very weak

We have observed a broad emission centered at about 800 nm. It is believed to be associated with iron impurities. The following CT process takes place

$$O^{2-} + Fe^{3+} + h\nu \rightarrow O^{-} + Fe^{2+} \tag{3.18}$$

leading to a strong laser absorption centered at 256 nm. This absorption is independent of the doping of the YAG crystal. The relaxation of Fe^{2+} to an excited state of Fe^{3+} which is responsible for the emission at 800 nm. This emission is in part absorbed by the Nd^{3+} ion as shown Fig. (**??**). Energy transfer or/and optical phonons released by relaxation of the Fe^{2+} manifold may justify the increase of the $^4F_{3/2}$ emission compared to the $^2F_{5/2}$.

Venikouas *et al.* [49] excited with a 266 nm laser an iron-free sample doped at 0.87% by mol. The absence of the emission at 800 nm has allowed them to prove that all the ions in the $^2F_{5/2}$ manifold relax by emitting a visible photon to a level that non-radiatively populates the $^4F_{3/2}$manifold that eventually emits an infrared photon. As a consequence of this mechanism, the ratio of the number of photons emitted in the visible range to that of photons emitted in the infrared range is ≈ 1.

From our measurements, this ratio for electron impact excitation is 5.4. Thus, we infer that several other mechanisms have to be active. Probably, the ratio between the populations of the $^4F_{3/2}$ manifold to the $^2F_{5/2}$ manifold may even be larger because the quantum yield of the $^4F_{3/2}$manifold is $\approx 87\,\%$ owing to the possible cross relaxation $^4F_{3/2} + {}^4I_{9/2} \rightarrow {}^4I_{15/2} + {}^4I_{15/2}$ [56].

3.2.6 Tm

The intense emission between 1600 and 2100 nm that can be observed in Fig. (**??**) is associated with the transition $^3F_4 \rightarrow {}^3H_6$. The spectrum shape is very similar to that obtained by a similar sample excited with a laser [57]. We measured a lifetime of 6.6 ms is estimated by the time evolution measured with InAs PD.

The weak emission between 1400 and 1550 nm and between 800 and 840 nm is ascribed to the transitions $^3H_4 \rightarrow {}^3F_4$ and $^3H_4 \rightarrow {}^3H_6$, respectively. They have the same time evolution shown in Fig. (3.20).

Similarly, using suitable filters, we can associate the emission around 750, 550, and 400 nm to transitions from the $^1I_6$ manifold (see Fig. (3.21)) and the emissions around 800, and 650 nm to those from the $^1G_4$ manifold.

It is known that cross relaxation $^3H_4 + {}^3H_6 \rightarrow {}^3F_4 + {}^3F_4$ may be very efficient and so the effective lifetimes of $^3H_4$ of Tm_x^{3+}:Y_{1-x}AG ranges between 511 μs for $x = 0.005$, 152 μs for $x = 0.04$ and 61 μs for $x = 0.06$ [56].

After $\approx 300\,\mu$s from the beginning of the pulse, only the manifolds $^3H_4$, $^3F_4$, and the groundstate $^3H_6$ are still populated because all other manifolds have lifetimes of less than a few tens of μs, as shown in Fig. (**??**). Thus, the lifetime of the $^3H_4$ manifold can be determined by analyzing the final part of the signal. We obtain the value $\tau \approx 110\,\mu$s that is compatible with the lifetime f the $^3H_4$ for a Tm^{3+}:YAG single crystal doped at 4.4% [56].

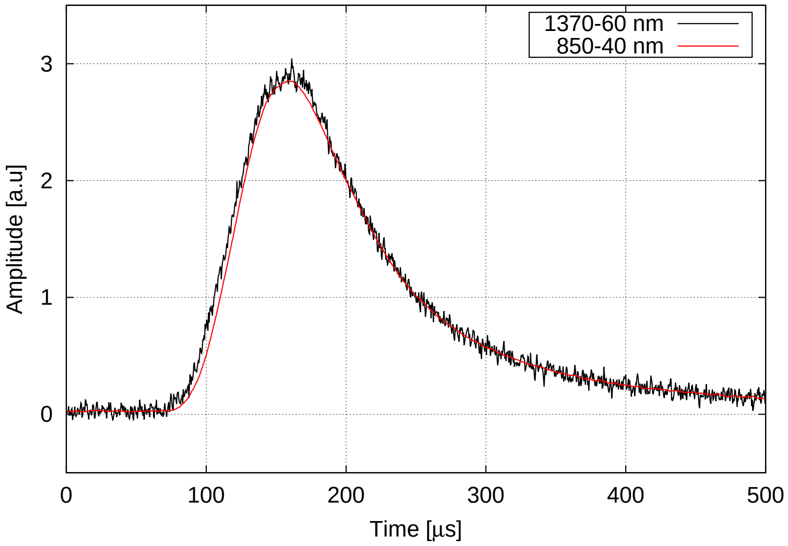

Figure 3.20: Time evolution of the PD output in particle excited Tm:YAG using several filters.

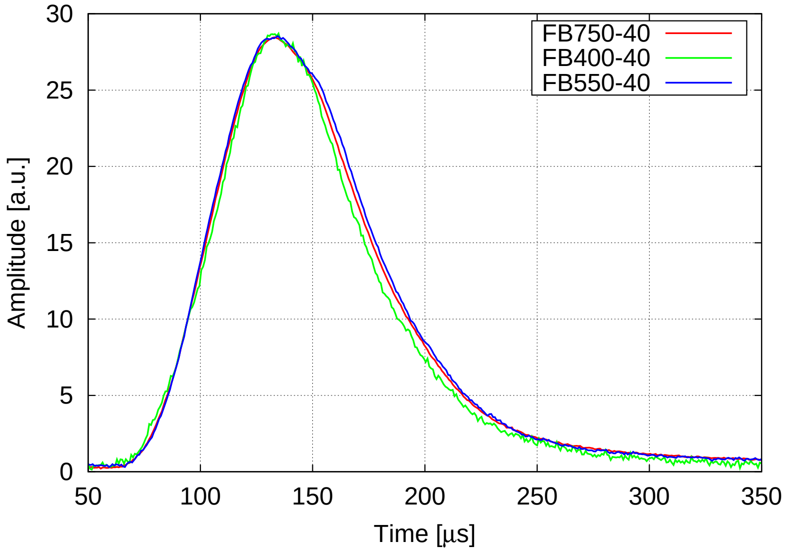

Figure 3.21: Time evolution of the PD output in particle excited Tm:YAG using different filters

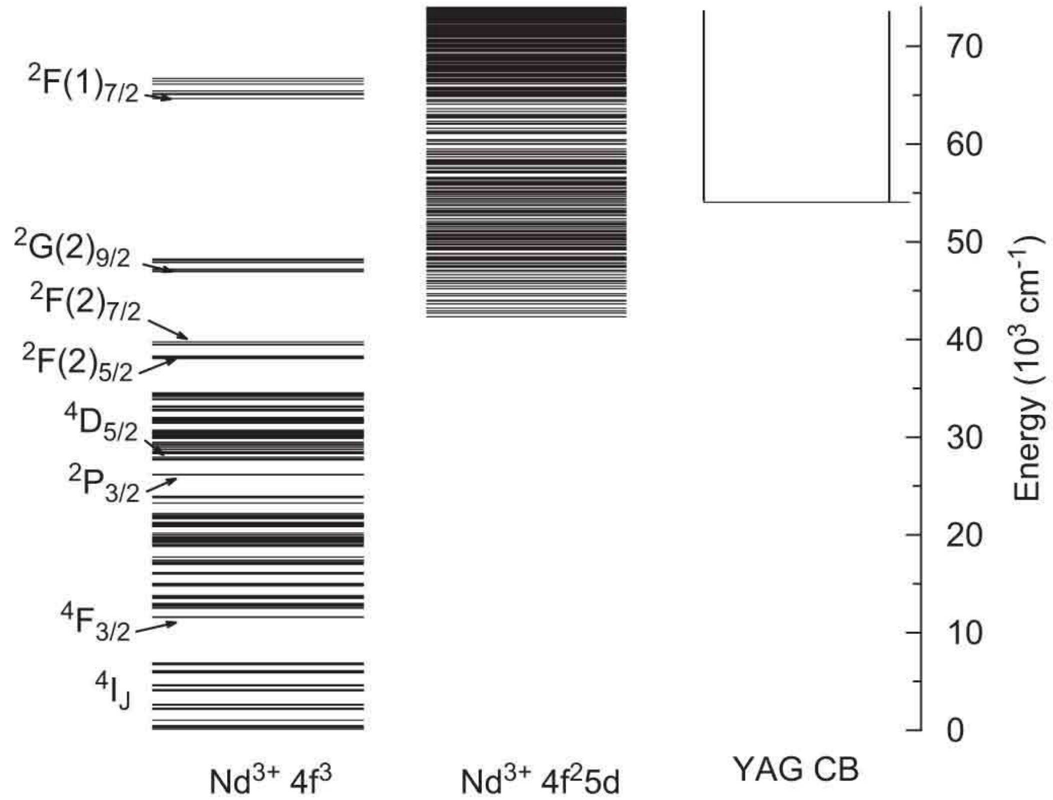

Figure 3.22: The $4f^3$, 5d energy level of Nd^{3+} in YAG and the conduction band respect to the valence band are shown. [55]

3.3. X-ray excitation studies

As mentioned above, LY cannot be accurately measured with electron impact excitation because it is difficult to estimate the exact quantity of energy injected into the crystal.

For this reason, we replace the Tungsten foil in the crystal holder flange with a $10\,\mu$m thick Tantalum foil. A 2 mm thick lead[8] foil with an suitable hole is fixed in front of the window in order to set the area of the x-ray beam. A black conductive adhesive tape, on which the sample is glued, closes the hole, thereby stopping the electrons that may have crossed the tantalum foil. The area of the x-rays beam must be much smaller than that of the crystal surface on which x-rays impinge and the crystal width must be at least of few millimeters to be sure that almost all the x-rays are stopped into the crystal. The goal is to accomplish a pulsed x-rays beam whose energy is proportional to the charge Q_{bs} of the electron beam pulse.

LYs of several samples can be easily determined with good accuracy by comparison with a sample whose LY is known. The calibration can be carried out only with x-rays because there are no literature calibration studies carried out by using electron impact excitation. Moreover, contrary to YAG, other matrices, including those based on Fluorine, are heavily damaged by a prolonged irradiation with the electron beam.

X-ray excitation can be a good alternative that may allow us to obtain the LY in different optical band, even if it has some disadvantages. Because the excitation and consequently the emission are much weaker, it is necessary to amplify the PD signals with the long time constant, charge amplifier, thereby loosing the possibility to extract information on the level lifetime from the detector signal. Moreover, much longer integration times are required to obtain a decent spectrum,

As a calibrated sample we used a $(\mathrm{Lu}_{0.75}\mathrm{Y}_{0.25})\mathrm{Al}_5\mathrm{O}_{12}$:Pr 0.16% (LuYAG:Pr) single crystals (5x5x5 mm^3) grown via Czochralsky method at ITME, Warsaw. It has $LY = 27 \times 10^3$ ph/MeV with 5.3% energy resolution in the UV range [58].

As we are more interested in the infrared and visible region than the UV, we have recorded spectra obtained by exciting this crystal with x-rays and with the 266 nm laser in order to identify the occurring transitions. These spectra are shown in Fig. (3.27) and Fig. (3.28). The x-rays generate e-h carriers that transfer energy to the Pr^{3+} ions, exciting them to the $5d$ levels. The UV laser directly populates the same levels. As some lines correspond to more than one possible transition, we also recorded the emission spectrum obtained by selectively exciting the $^1\mathrm{D}_2$ manifold with a dye laser tuned at 585 nm. The main transitions scheme we have been able to deduce is shown in Fig. (3.29).

We have to note that the calibration of the spectrum obtained with x-ray excitation on the UV emission produces a relative enhancement of the emission in the visible range. This means that the manifolds $^1\mathrm{D}_2$ and $^1\mathrm{G}_4$ are more populated by x-ray excitation than by UV excitation. Moreover, one can deduce that in the x-ray excitation, in addition to the relaxation of the $5d$ levels, other processes may occur to populate the $4f$ levels.

---

[8] The thickness of the lead foil is big enough to stop all the x-rays generated by the 70 keV electrons.

In analogy with the case of the particle excitation, we can introduce the formula for the LY in a given wavelength band as

$$LY(\lambda_i, \lambda_f) = \frac{R_0}{G\tau_d}\frac{4\pi}{kA}\left(\frac{Q_d}{Q_{\mathrm{bs}}}d^2\right)\frac{\int_{\lambda_i}^{\lambda_f}\lambda S(\lambda)\,\mathrm{d}\lambda}{\int_{\lambda_i}^{\lambda_f}\eta(\lambda)T(\lambda)\lambda S(\lambda)\,\mathrm{d}\lambda} \tag{3.19}$$

in which G and τ_d are the gain and the integration constant of the charge amplifier, and k is a proportionality constant. Moreover, the PDs responsively has ben replaced by their quantum efficiency $\eta(\lambda)$.

At variance with the electron impact excitation case, now the spectrum is not corrected for the CCD efficiency. Thus, we use a little modified (and approximate) procedure. We assume that $\eta(\lambda)T(\lambda)$ is constant in the desired wavelength range $[\lambda_i,\, \lambda_f]$. This assumption is not a limiting factor because the PD quantum efficiency is generally a smooth function of λ. Moreover, bandpass filters can select narrow wavelength ranges, thereby strongly enhancing the goodness of this approximation. Alternatively, since the longpass filter FGL transmission above the cut-in wavelength is constant, equal to ≈ 0.90, the difference of the a parameters related to two different filter, is equal to the a parameter related to an ideal bandpass filter with a trasmission of 0.90 between the two longpass filter cut-in. Within this approximation, Eq. (**??**) becomes

$$LY(\lambda_i, \lambda_f) = \frac{R_0}{G\tau}\frac{4\pi}{k\eta TA}\left(\frac{Q_d}{Q_{\mathrm{bs}}}d^2\right). \tag{3.20}$$

The parameter $a = (Q_d/Q_{\mathrm{bs}})d^2$ is measured using the Si(I) detector for the crystals Pr:LuYAG, Nd:YAG, and Tm:YAG with the procedure outlined earlier in this work. In Fig. (**??**) we show the dependence of Q_d/Q_{bs} vs the distance x and the inverse parabolic fit.

We have to note that a small fraction of x-rays can directly hit the detectors, especially when short crystals of low atomic number Z are used, thereby giving a contribution to the measured signal. This contribution is estimated by blocking the luminescence light with a $200\,\mu$m thick Al foil and then it is subtracted. In Fig. (3.26) we show for Nd :YAG crystal the relevance of the x-ray contribution.

If the k proportionality constant in Eq. (3.20) were known, the LY in the given band of any crystals could be obtained by the measurement of the quantity a. We observe from Eq. (3.20) that in this type of measurements it crucial to know with precision the efficiency of the x-ray generation process, related to proportionality constant k. It can be estimated if the x-ray energy is fully released in the sample and provided the LY and the a parameter of a generic crystal in any wavelength range are known. As the sensitivity of the detector that has been used to measure the light yield of the LuYAG:Pr sample is peaked in the UV range, it is reasonable to expect that the reported light yield is mainly determined by $4f5d \to 4f^2$ radiative transitions. Furthermore, short integration times are prone to underestimate the slow components. In order to select the PD signal component due to

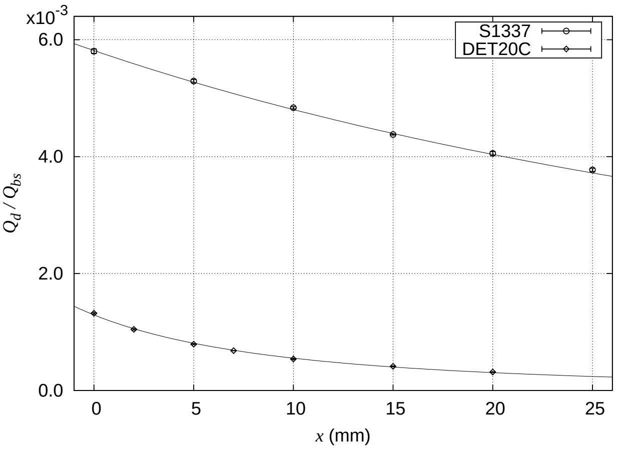

Figure 3.23:

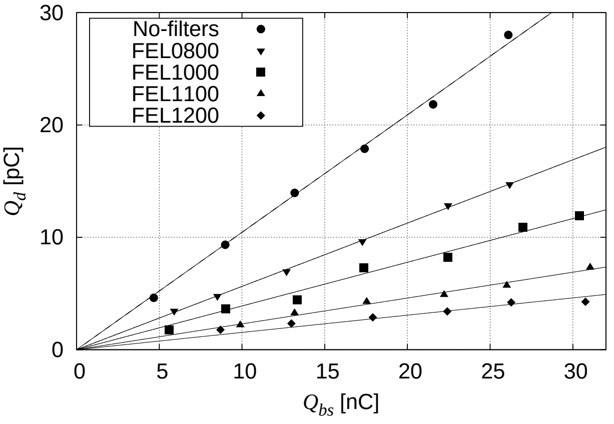

Figure 3.24: Linear response in the visible range of the Pr:LuAG crystal as a function of the injected charge.

the UV scintillation, the previously described measurements are performed with optical longpass filters FGL and with Silicon detector S1337 (that has a high quantum efficiency even in deep UV). In particular, the UV component is estimated as the difference of the a parameter without filters and that with FGL495 filter corrected by the filter trasmission, as can be seen by inspecting Fig. (**??**). This procedure yields the k value.

Likewise, the LY yield, calculated with eq 3.20, is estimated between 495 and 1700 nm using different longpass filters (FGL, FEL) and also InGaAs PD (see Fig. (**??**) and Fig. (3.24)). The results are reported in tab **??**. Owing the high phonon energies of LuYAG, no transitions in the mid-infrared range are to be expected. However, the LY in this band can be measured in the same way using InAs or InSb PD.

The value of a parameter for both samples using S1337 PD are presented in Tab. (3.2). In addition, the emission spectra between 200-1000 nm is recorded with silicon CCD spectrometers and they are very similar to that acquired with electrons excitation. This is reasonable because the x-rays, as the electrons, create a swarm of secondary ionizing pho-

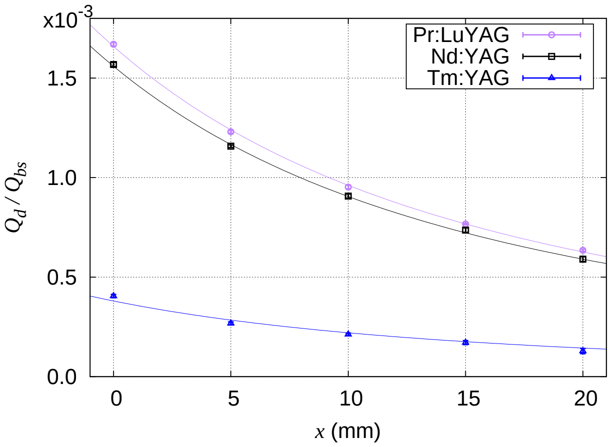

Figure 3.25: Linear response in the infrared range of the Pr:LuAG crystal as a function of the injected charge.

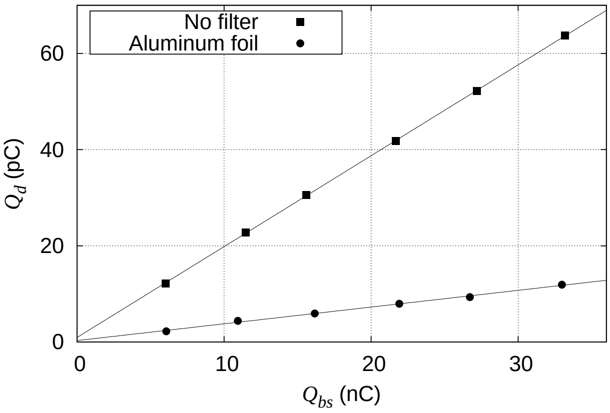

Figure 3.26: X-ray contribution to the PD output.

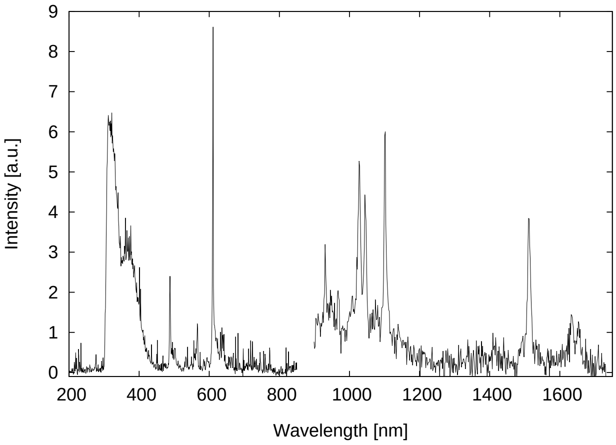

Figure 3.27: Emission spectrum Pr:LuYAG excited with electron gun

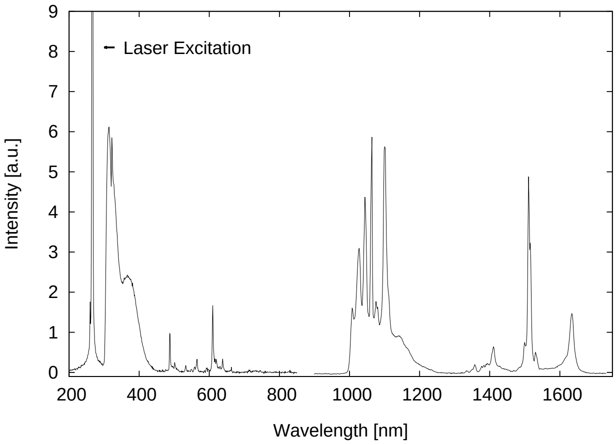

Figure 3.28: Emission spectrum Pr:LuYAG excited with 266 nm laser.

Pr:LuYAG	
Optical range [nm]	*LY* [ph/MeV]
200-495	27000 [58]
495-780	8300
780-1000	1100
1000-1100	1300
1100-1200	600
1200-1700	1100

toelectrons, For these reasons, we can assume that the ratio between the *LY*s in visible and in infrared range is the same for the two different excitations. Hence, the *LY* between 200 and 1000 nm band for both samples is estimated by using Eq. (3.19) and from the analysis of the previous section, the *LY* above 1000 nm is obtained. We can deduce that the number of ions excited per MeV in the low metastable manifolds $^4F_{3/2}$ and $^3F_4$ are about 56×10^3 and $\approx 49 \times 10^3$ for Nd:YAG and Tm:YAG, respectively. The accuracy of these figures is estimated to be $\approx 10\%$.

In particular we have calculated the visible *LY* of the Nd:YAG crystal and obtained 10.4×10^3 ph/Mev, in agreement with the 11×10^3 ph/MeV reported by Yanagida and his group [54] for a similar sample at the same dopant concentration. In addition, they measured the *LY* in visible range for several RE doped YAG and LuAG single crystals via gamma-ray excitation and obtained values up to 15×10^3 ph/MeV.

The results are summarized in in Tab. (3.2).

3.4. Electron excitation and up conversion

We have observed that electrons and x-rays lead to a considerable population of the low energy levels of the rare earth ions dopant. we have to prove that UP can be now induced,

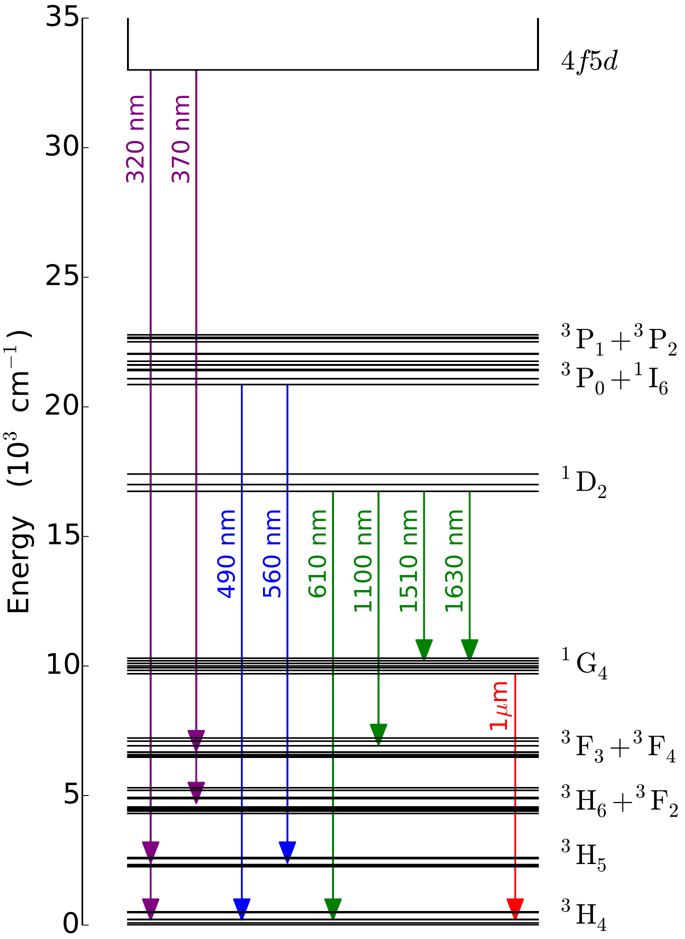

Figure 3.29: Energy level structure of Pr:LuAG and the main transitions.

thereby showing the feasibility of the detection process. In order to produce UP the crystals are mounted on a suitably modified flange so that the crystal can be irradiated sideways with a tunable continuous wave Ti:Sa laser whereas the luminescence light is collected by a photomultiplier PMT located in front of the crystal, as shown in Fig. (3.30). The laser can deliver up to 200 mW in the wavelength range 790-860 nm.

Unfortunately, neither Nd^{3+} ion nor Tm^{3+} ions inYAg show an energy level scheme compatible with the emission range of the tunable laser and, thus, cannot be used to this goal. We therefore, use an Er:YAG single crystal doped at 0.5% by mol. Its energy level structure is shown in Fig. (**??**). The particle excitation should populate the first excited $^4I_{13/2}$ manifold that is located at $\approx$ 0.74 eV above the ground state. The laser, tuned at $\approx$ 850 nm, promotes the ions from this manifold to the $^4S_{3/2}$ whose fluorescence at $\approx$ 550 nm will tag the particle passage.

Table 3.2: *LY* parameters for ND: and T:YAG

Nd:YAG		
Manifold	Optical range [nm]	*LY* [ph/MeV]
$^2F_{5/2}$	390-650	10400
$^4F_{3/2}$	800-1500	56000
Tm:YAG		
Manifolds	Optical range [nm]	*LY* [ph/MeV]
$^1I_6, ^1D_2, ^1G_4, ^3H_4$	280-900	7700
$^3F_4$	1600-2300	49100

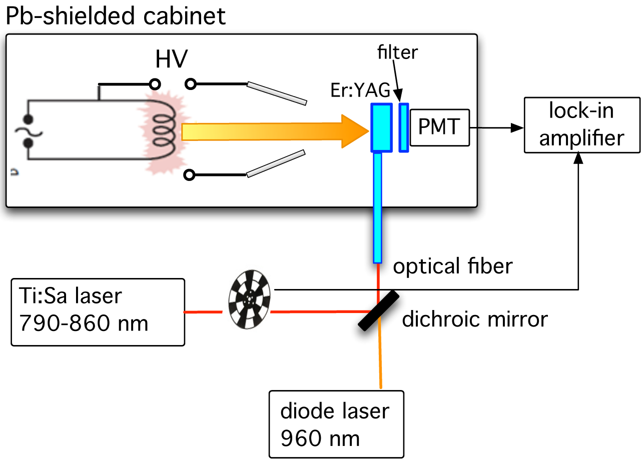

Figure 3.30: Scheme of the apparatus for double resonance and up conversion measurements.

We have carried out the same cathodoluminescence measurements as for Nd and Tm but, as we observed a strong nonlinear response of the crystal to the amount of charge injected into it, these measurements are not yet competed and are still under way. Nonetheless, as the detector has to work at very low particle excitation, the nonlinearity does not hinder the UP conversion measurements.

For the sake of completeness, we show in Fig. (**??**) the cathodoluminescence spectrum of Er:YAG where the radio time manifolds are identified.

In order to carry out the UP measurements the Ti:Sa is chopped at low repetition rate ($\approx 10\,$Hz). A bandpass filter (FB550-40) between crystall and PMT selects the fluorescence only in the range 540-560 nm. In order to reduce the large noise due to the Ti:Sa laser, the PMT output is connected to a lock-in amplifier synchronized with the chopper. This noise is actually the so called laser double resonance (LDR) that will be treated in detail in the next chapter. The e-gun is operated in continuous mode at 70 keV.

A dynamic equilibrium occurs in the population of the different excited state, in particular a constant fraction of ions lives in $^4I_{13/2}$ state and the lock-in amplifier rejectst the PMT signal due to the $^4S_{3/2}$ constant emission at 550 nm.

The wavelength of the tunable Ti:Sa laser is varied in the range 790 nm-860 nm in

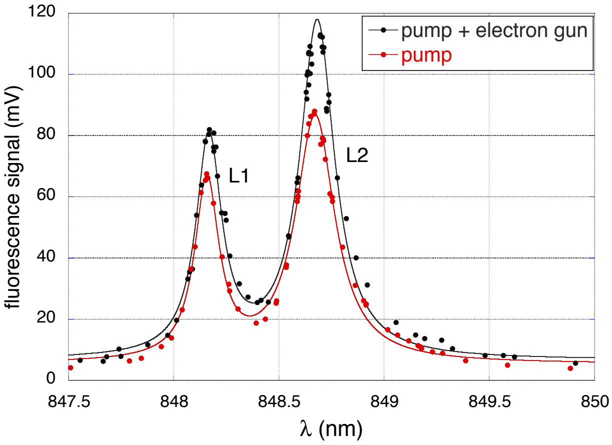

Figure 3.31: Double resonance and up conversion of Er:YAG [59].

order to find the resonances between $^4I_{13/2}$ and $^4S3/2$ Stark levels at which we expect an increase of the lock-in signal. In fig 3.31 we plot the signals due to the $^4S_{3/2}$ fluorescence intensities for different wavelengths of the pump laser, but at the same laser intensity, with and without the electron excitation. The second measurement is needed to quantify the contribution of the laser double resonant process. Two particularly intense transitions are identified by fitting each of the two sets of data to two Lorentzian functions. Even if the emission due to laser double resonance represents a large contribution to the signal, an increase of about 30% of the areas under the Lorentzian curves when electrons excite the crystal, demonstrates the feasibility of the detection process based on the Infrared Quantum Counter concept.

Moreover, it is also observed, by setting the laser wavelength at about 848.7 nm, a linear dependence between the current $I_{\rm bs}$ (up to 1.6 μA) of the electron beam and the fluorescence signal with a fixed laser intensity (280 mW).

3.4.1 Conclusion

To summarize the results of this section, we can say that an efficient procedure to measure the *LY* in different optical bands can be proposed and we have successfully implemented it.

Both with electrons and x-ray excitation it is possible to record emission spectrum with CCD spectrometers, but only cathodoluminescence is intense enough in order to acquired spectra from 632 nm to 5 μm, with a resolution up to 0.5 cm^{-1} using FTIR coupled with InSb (or InAs up to 3 μm). Rapid-scan mode allows to complete the measurements in few minutes.

Furthermore, the electron excitation allows us to study the emission temporal evolution, from which important information on the level lifetimes, energy transfer process and the levels involved in the emission can be deduced.

Laser excitation can be useful in order to resolve some ambiguous transition identification. We have observed that electrons excitation provides the same emission spectrum of

Pr:YAG 0.16%					
excitation	**PD**	**filter**	**Q_d/Q_{bs}x10^3**	**x_0** [mm]	**a** [mm^2]
X-rays	S1337	-	5.80 ± 0.04	31.86 ± 0.46	1.678 ± 0.057
		FGL400	1.74 ± 0.01	-	-
		FGL495	1.41 ± 0.01	-	-
		FGL715	0.58 ± 0.01	-	-
		FGL780	0.42 ± 0.01	-	-
		FGL850	0.33 ± 0.01	-	-
		aluminum foil	0.21 ± 0.01	-	-
	Det10C	-	1.044 ± 0.012	11.46 ± 0.70	0.87 ± 0.08
		FEL800	0.563 ± 0.003	-	-
		FEL1000	0.389 ± 0.009	-	-
		FEL1050	0.282 ± 0.003	-	-
		FEL1100	0.230 ± 0.004	-	-
		FEL1200	0.154 ± 0.006	-	-
		aluminum foil	0.031 ± 0.011	-	-

Table 3.3: Results of the linearity fits performed with different PDs, filters and inverse parabolic fits of the Nd:YAG excited by electrons or by x-rays

x-ray excitation and even if it is able to release much more energy into the crystal, some host materials may be damaged.

For each excitation type, it is possible to quantify the relative emission in many narrow optical bands from UV to mid-infrared range by measuring the ratio Q_d/Q_{bs} in different positions with appropriate optical filters and detectors. By comparison with a calibrated sample, the visible LY can be estimated from Eq. (3.20), as well as the LY in each other range where the relative emission compared to the visible one is known if the required spectrum is known (Eq. (3.19)) or if filters are used (Eq. (3.20)).

Tm:YAG 4.4%					
excitation	**PD**	**filter**	**Q'_d/Q_{bs}x10^3**	**x_0** [mm]	**a** [mm^2]
Electrons	Det36A	-	19.94 ± 0.06	10.84 ± 0.28	5.14 ± 0.19
		FB450-40	6.37 ± 0.04	-	-
		FB650-40	0.57 ± 0.01	-	-
		FB800-40	2.20 ± 0.01	-	-
	Det10C	-	2.94 ± 0.03	11.46 ± 0.70	0.87 ± 0.08
		FEL1500	2.65 ± 0.06	-	-
	P7163	-	-	10.79 ± 0.60	1.54 ± 0.09
X-rays	S1337	-	-	31.9	0.386 ± 0.011

Table 3.4: Results of the linearity fits performed with different PDs, filters and inverse parabolic fits of the Tm:YAG excited by electrons or by x-rays.

Nd:YAG 1.1%					
excitation	**PD**	**filter**	$\mathbf{V_d}/\mathbf{I}_{\mathrm{bs}}$	$\mathbf{x_0}$ [mm]	**a** [mm^2]
Electrons	Det36A	-	46.818 ± 0.054	7.03 ± 0.30	13.81 ± 0.98
		FEL500	40.361 ± 0.048	-	-
		FEL750	30.911 ± 0.023	-	-
		FB900-40	9.529 ± 0.011	-	-
		FB1064-10	4.272 ± 0.004	-	-
	C30723	-	-	6.74 ± 0.09	4.873 ± 0.090
X-rays	S1337	-	-	31.97 ± 0.65	1.593 ± 0.058

Table 3.5: Results of the linearity fits performed with different PDs, filters and inverse parabolic fits of the Nd:YAG excited by electrons or by x-rays

Chapter 4

Low temperature upconversion measurements

In the previous chapter, a population of the low energy level in Nd:YAG and in Tm:YAG as high as about $5 times 10^4$ per MeV has been estimated and the measurements on the Er:YAG has proved the feasibility of the detector. However the efficiency, i.e, the visible LY and the noise are not satisfactory at all. For these reasons, a study of the upconversion process, and in particular of the laser double resonance (LDR), must be carried out. The development of new experimental setup allows us to investigate several detection energy level schemes for different combinations of rare earth dopants and host matrices, at room temperature and at 10 K.

In the chapter 2 we have proposed a model to describe the characteristics of the detector based on the IRQC concept. Now, we will present the measurements that have led to prove the goodness of that model. In particular, it will be demonstrated that the phonon assisted, side band absorption is the main process responsible for the LDR and noise. We will search for the most promising RE doped crystals and upconversion energy level schemes for the realization of the proposed detector by also minimizing any spurious contributions.

4.1. Experimental technique and setup

The experiment aimed at observing the upconversion processes is conceptually very simple. An infrared source, used to simulate the effect of the particle induced excitation, is shone on the crystal in order to populate the low energy levels of the RE ions. The ions are promoted to higher lying levels by a tunable laser. Finally, the visible fluorescence emitted by the deexcitation of the high levels is detected. In the following we describe the technical detail of the apparatus built for the experiment.

The RE doped crystals are mounted on the cold head of a cryocooler within a suitable cryostat and can be cooled down to 10 K. Three antireflection quartz windows (transparent in the range 200 nm to 4000 nm), each centered on a different side of the crystal, allow us to excite and to observe the crystal from outside the vacuum vessel. By referring to the pictures of the apparatus shown in Fig. (4.2) and Fig. (4.3), the left window is used to pump the crystal with an infrared source. The laser enters the cell through the right window, whereas the third window allows the PhotoMultiplier Tube (PMT) or PDs to collect the fluorescence.

1. The infrared source (Newport, mod. 80030) is based on a SiC filament that is Joule heated up to incandescence. Its spectral emission is characterized by a Planck distribution at temperature $T \approx 1550\,\mathrm{K}$. The infrared source is used to simulate the particle passage by exciting the rare earth ions into a specific low energy metastable level. Two lenses, that act as a telescope, and one diaphragm focus the light on the crystal whereas optical filters can be mounted to select the desired wavelength ranges of the source fluorescence. An intensity of $340\,\mu\mathrm{W}$ and of $680\,\mu\mathrm{W}$ is measured with the Germanium bolometer (Coherent, mod. LM-10) when optical filters FEL1500 and FEL1300 are respectively mounted. The diameter of the beam spot in the middle of the crystal, measured by a cam[1], is $\approx 3\,\mathrm{mm}$.

2. A tunable lasers is necessary in order to pump the ions in the excited state to a more energetic one. Thanks to its broad tuning range and to its narrow linewidth, it is possible to test different upconversion energy level schemes and to optimize the upconversion efficiency tuning the laser between the Stark level resonances.Three tunable laser are available

    - **Avesta cw Ti:Al$_2$O$_3$ Laser:** It is a Ti:sapphire laser is tunable[2] between 690 and 1030 nm with 1.5 W output power at 800 nm and about 700 mW average output power when it is pumped with 6 W released by a Coherent cw frequency-doubled Nd:YAG Lasers (532 nm). Thanks to two etalons placed into the resonator, the linewidth of the generated radiation is narrowed down to 2 GHz. The beam has a TEM$_{00}$ spatial mode and a divergence less than 2 mrad.
    - **Coherent cw Ti:Al$_2$O$_3$ Laser:** Ti:sapphire laser is pumped by 6 W cw frequency-doubled Nd:YAG Lasers (532 nm) or by 6 W Argon-ion laser. It is tunable between 790 and 860 nm with about 200 mW average output power and with a picometer accuracy.
    - **Dye Laser:** The rhodamine 6G dye laser, pumped by 6 W cw argon-ion laser, has $\approx$ 200 mW output power that can be tuned from 570 nm to 615 nm with picometer accuracy.

    Several micrometrical adjustable mirrors are used to lead the laser beam to the center of the crystal. Lenses with different focal lengths can be located on the laser optical path in order to reduce the laser beam diameter in the middle of the crystal. The

---

[1] The beam is reflected by inserting a mirror at halfway between the source and the crystal and then analyzed by the cam so that the optical path travelled by the beam is the same as that from the source to the crystal.

[2] with only one set of optics

beam diameter can be measured by the cam. The bolometer (Coherent, mod. LM-10) and the wavelength analyzer (Thorlabs, mod. S132C) measure the intensity and the wavelength of all the three tunable laser with an accuracy of 1 mW and 1 pm, respectively. An half-wave plate can set the angle of the linear polarization of the lasers.

3. The PDs are the same described in Sec. (3.1). The Hamamatsu PMT R2248 has a bialkali photocathode and eigtht dynodes. Its quantum efficiency and its gain as function of wavelength and supply voltage are shown in fig. 4.1. The PMT output is read by a ammeter.

In addition, a weak 60 keV gamma source ($10^7 \gamma/\mathrm{srad\,s}$) can be located in a groove of the vessel, centered to the crystal. It can excite the sample thanks to the few mm of the aluminum thickness in that part of the vessel.

The infrared source induces a small constant fraction of RE ions to a desired low energy metastable level. The wavelength of the laser required for up conversion an be approximately calculated by using literature data for the level energy values of RE ions[3]. The resonances between the Stark levels of the two investigated manifolds are sought in the neighborhood of the calculated value. At resonance, upconversion occurs. The consequent visible fluorescenceis collected by the PMT.

This measurement is repeated with the infrared source switched off in order to study the LDR process. The more energetic level may be populated by laser itself, indeed. By comparison of the PMT output[4] in the two cases, we can estimate the signal-to-noise ratio S/N. Please note that in this context we use the term “signal” to identify the PMT output with the infrared source switched on and the term “noise” is used to name the PMT output in the LDR case. The dependence of signal, noise and relative ratio on several factor like laser intensity and phonon energy of the crystal is investigated in order to confirm the model proposed in Chapter (3). The aim is to understand how to reduce S/N enough in order to detect the excitation of the small gamma source.

---

[3] The values of RE ion energy levels are tabulated only for few matrices and show a quite large dependence on the temperature (Eq. (**??**)). The accuracy of the calculated wavelength is < 1 nm.

[4] Under the same laser conditions.

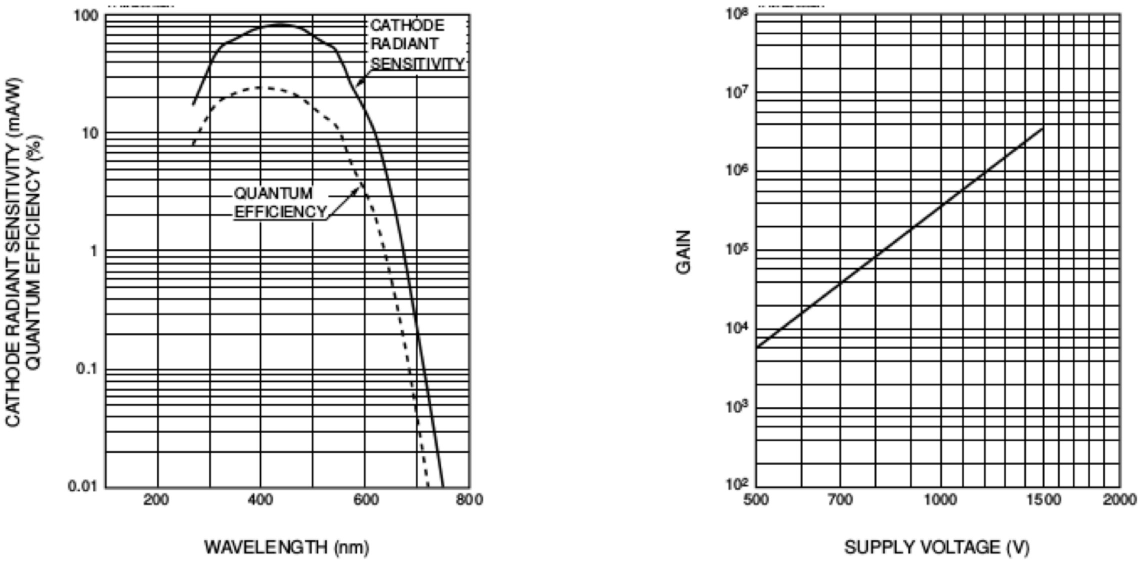

Figure 4.1: Features of the PMT.

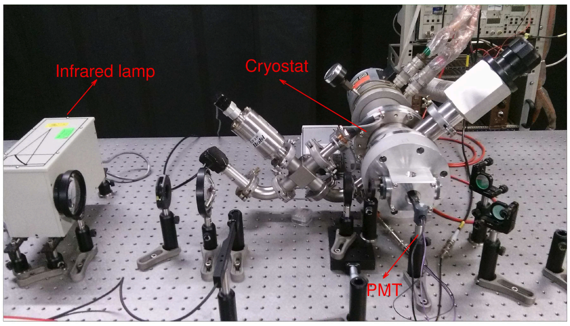

Figure 4.2: Cryogenic and optical setup of the experiment.

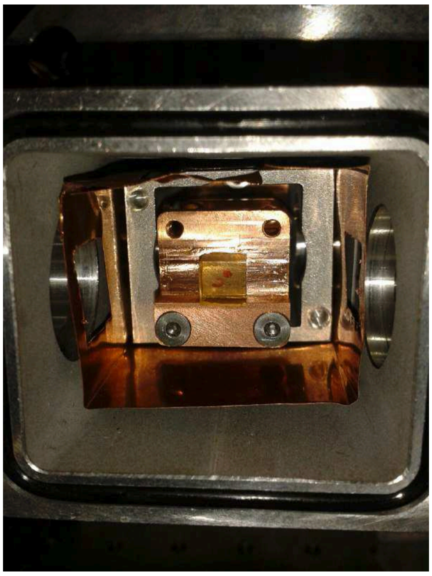

Figure 4.3: Detail of the crystal cell assembly.

4.2. Erbium

The UP and LDR of three different host matrices (YAG, KYF, YLF) doped with Erbium (0.5%, 1%, and 1%, respectively)[5] are investigated at 10 K. The structure of the Erbium energy levels and the UC and LDR scheme applied to them are shown in Fig. (4.4).

The source light crosses the longpass filter FEL1500, thereby only populating the first excited $^4\mathrm{I}_{13/2}$ manifold directly from the ground state. Particle excitation should populate the same manifold.

As discussed in section Sec. (1.3.2), at 10 K only the first two levels of the $^4\mathrm{I}_{13/2}$ manifold are mainly populated because the third energy level of this manifold is separated from the first by about $45\,\mathrm{cm}^{-1} \approx 6\,\mathrm{meV}$ [60] that corresponds to about $6k_\mathrm{B}T$. According to the Boltmann distribution, the ratio between the population of the two levels is also equal to about 400. Actually, the observed fluorescence is weaker when the laser is tuned on the second level of the manifold rather than when the laser is tuned on the first one. No resonances are observed from the other levels.

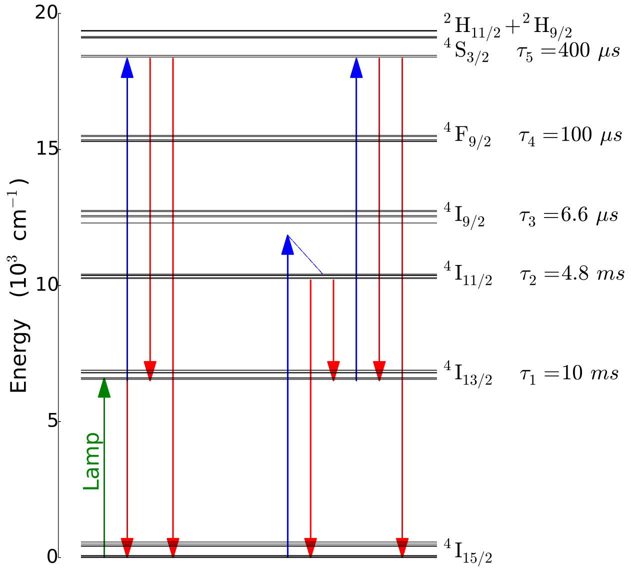

Figure 4.4: Energy level structure, energy level up conversion, and LDR scheme for Er:YLF [61] [62].

The Ti:Sa laser can be tuned on the transitions $^4\mathrm{I}_{13/2,1/2} \rightarrow {}^4\mathrm{S}_{3/2,\mathrm{M}}$ with $\mathrm{M} = 1/2$ or $3/2$ at about 836 nm and 840 nm, respectively. The bandpass filters FB540-40, that selects only the crystal fluorescence from the transition $^4\mathrm{S}_{3/2} \rightarrow {}^4\mathrm{I}_{15/2,\mathrm{M}}$ [6] is mounted in front of

---

[5] The first crystal is the same describer in the previous chapter. It has been cut as a cube 3 mm on each side. The two other crystals (of a similar sizes) are grown by the Tonelli group of Department of Physics of the Pisa University.

[6] Only the $^4\mathrm{S}_{3/2,3/2}$ decays radiatively because the two levels of $^4\mathrm{S}_{3/2}$ manifold are separated by $\approx 60\,\mathrm{cm}^{-1}$. Even if the more energetic $^4\mathrm{S}_{3/2,1/2}$ is excited, it quickly relaxes to the level $^4\mathrm{S}_{3/2,3/2}$, indeed.

the PMT to avoid the noise due to the Ti:Sa light scattered by the crystal. It should be noted that this upconversion scheme is described by the first model in Chapter (2), where the ${}^4\mathrm{I}_{15/2,5/2}$, ${}^4\mathrm{I}_{13/2,1/2}$, ${}^4\mathrm{I}_{11/2,1/2}$ and ${}^4\mathrm{S}_{3/2,1/2}$ (or ${}^4\mathrm{S}_{3/2,3/2}$) are to be identified with levels 0, 1, 2, 3, and 4, respectively. At 10 K we can neglect energy transfer processes between these levels [].

In Fig. (4.5), Fig. (4.6), Fig. (4.7) the PMT signal as function of the Ti:Sa laser wavelength[7] with infrared source switched off and on is plotted for the three Erbium doped host matrices. The two sets of data relative to each crystal are fitted to Lorentzian functions. Tthe results of the fits are presented in Tab. (4.1). The different quality of the crystal can be responsible for the difference in the $FWMH$. In particular, it should be noted the very narrow absorption line of the Er:YLF.

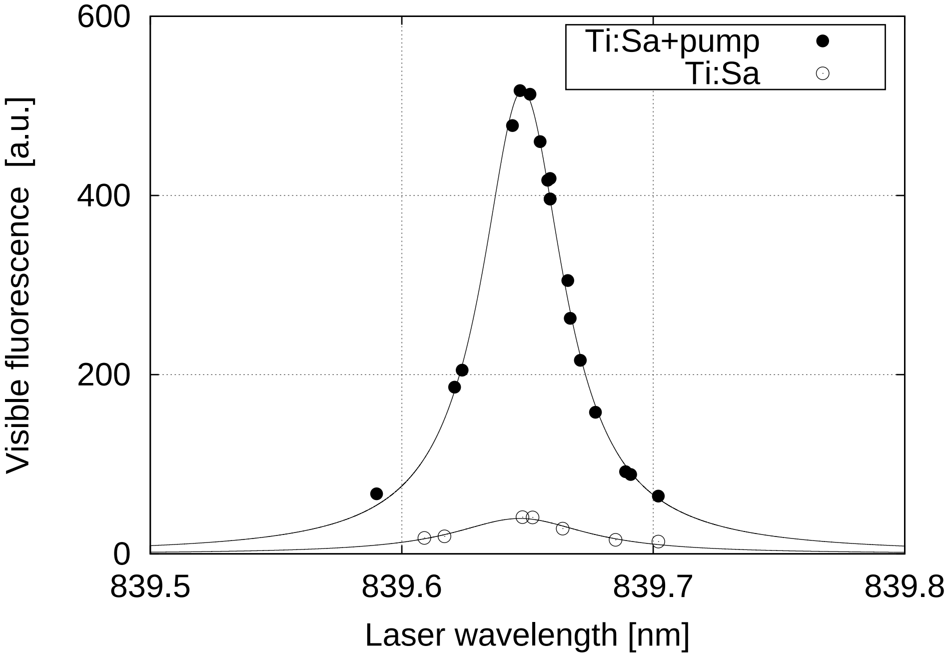

Figure 4.5: Dependence of the PMT output and noise on the laser wavelength for Er:YAG.

---

[7] With the same intensity. The polarization in each cases is set to maximize the signal.

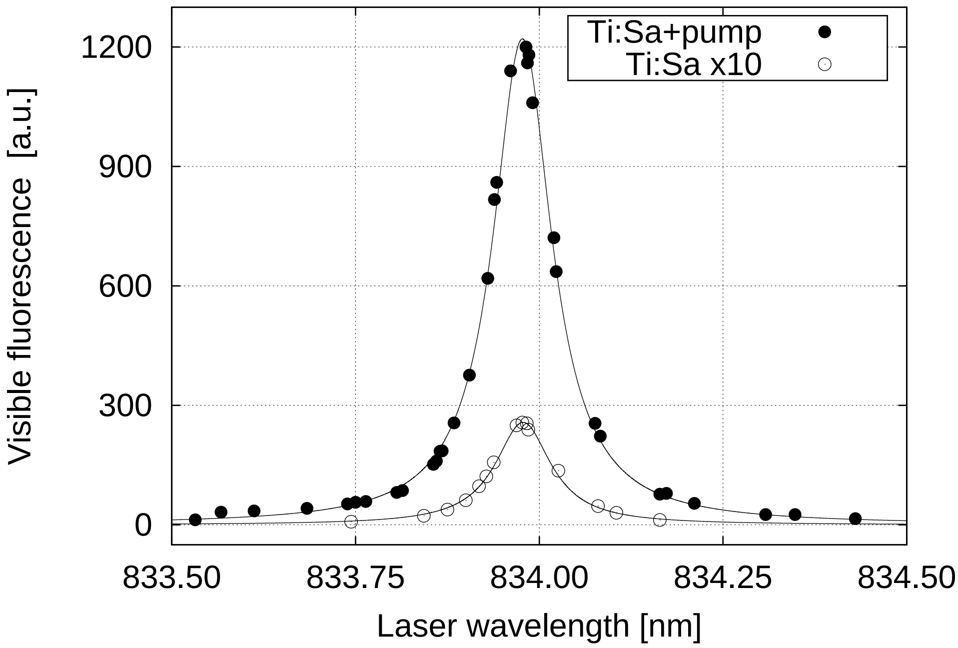

Figure 4.6: Dependence of the PMT output and noise on the laser wavelength for Er:KYF.

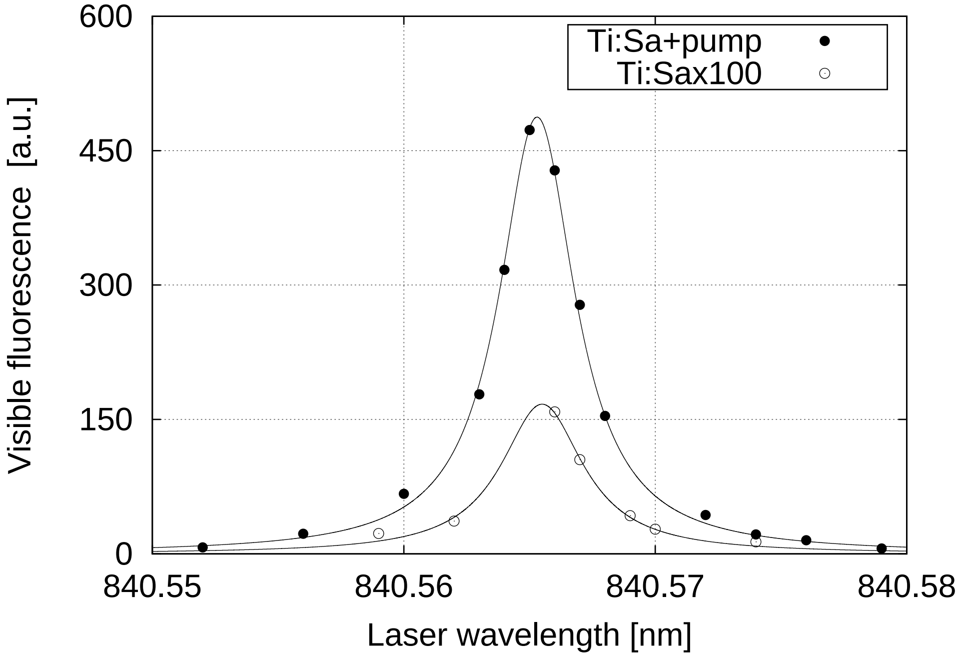

Figure 4.7: Dependence of the PMT output and noise on the laser wavelength for Er:YLF.

As for electron excitation, the signal and the noise depend on the laser wavelength but their ratio is independent of it. In fact, the two Lorentzian functions obtained with the source switched on and off only differ by the amplitude coefficient.

Actually, the effective UP efficiency (defined as the number of emitted visible photons divided by the number of ions excited in the low metastable level) depends on many factors (Eq. (**??**)) but it is the same for the ions excited into the $^4\mathrm{I}_{13/2,1/2}$ level by the source and by the laser.

We also plot the results obtained with the birifrangent crystal Er:YLF as a function of the laser polarization orientation. As signal and noise also share the same dependence on it, this means that the S/N quantity represents the ratio of the number of ions excited in the $^4\mathrm{I}_{13/2,1/2}$ level when the infrared source is on to that when the source is off.

It must be noted that according to Eq. (1.39) the cross section of the phonon assisted side band absorption and so the number of ions excited in $^4\mathrm{I}_{13/2,1/2}$, has a strong dependence on the laser wavelength, but it can be neglected in the narrow linewidth range. The Lorentzian shape fitting the sets of data is due to the fact that the effective upconversion efficiency (Eq. (1.39)) is proportional to the cross section of the transition $^4\mathrm{I}_{13/2,1/2} \rightarrow {}^4\mathrm{S}_{3/2,\mathrm{M}}$ for low intensity[8].

According to the model in Chapter (2), the $^4\mathrm{I}_{11/2}$ manifold is populated by the laser via the Stokes process, whereas the Antistokes process, that should populate the $^4\mathrm{I}_{9/2,1/2}$ manifold, is inhibited by the low temperature. It is observed, actually, a decrease of the LDR output[9] by a factor equal to about 20 by cooling the Er:YAG crystal from room temperature to 10 K.

The energy separation between the laser photon tuned at the resonance and the $^4\mathrm{I}_{11/2}$ manifold is about of $1600\,\mathrm{cm}^{-1}$. About 2, 3, 4 phonons are needed for Er doped YAG, YLF and KYF, respectively, for the Stokes process to occur (see Tab. (1.2)). In addition, as the multiphonon relaxation rate decreases exponentially with the effective phonon energies of the host matrix (Sec. (1.4.4)), a major contribute to the radiative relaxation is expected by the $^4\mathrm{S}_{3/2}$ and $^4\mathrm{I}_{11/2}$ manifolds in low energy phonon matrices. In particular, the multiphonon relaxation of the $^4\mathrm{I}_{11/2}$ manifold favors the population of the $^4\mathrm{I}_{13/2}$, thereby increasing the LDR process Fig. (4.4), whereas the radiative relaxation towards the ground state is dominant [61]. For this reasons, we expect a lower S/N ratio (under the same experimental conditions) for the Er:KYF crystal and a higher values for the Er:YAG. Actually, the S/N value tabulated in Tab. (4.1) can roughly be compared to each other because the crystals slightly differ in concentration and absorption cross section and have been excited with slightly different laser intensities. However, we have obtained a larger than expected value for the ER:KYF compared to the other two. It may be caused by low crystalline order that can give rise to a major laser absorption. This is confirmed by the larger linewidth.

Eq. (2.16) and Eq. (2.7) predict a different laser intensity dependence of the signal and the noise. In particular, for low intensity the former should have a linear dependence whereas the latter a quadratic one. The measurements for all the three crystals confirm the prevision, as can be seen in Fig. (4.8) for Er:KYF.

---

[8] In the measurements with electron excitation we used gaussian function to fit the data because, at room temperature, the line broadening due to the vibrational coupling deforms the Lorentzian shape

[9] We have to account for a thermal shift of 1 nm in the whole temperature range.

However, in all the three cases, the LDR process is too efficient in order to detect an increase of the signal due to the small gamma source.

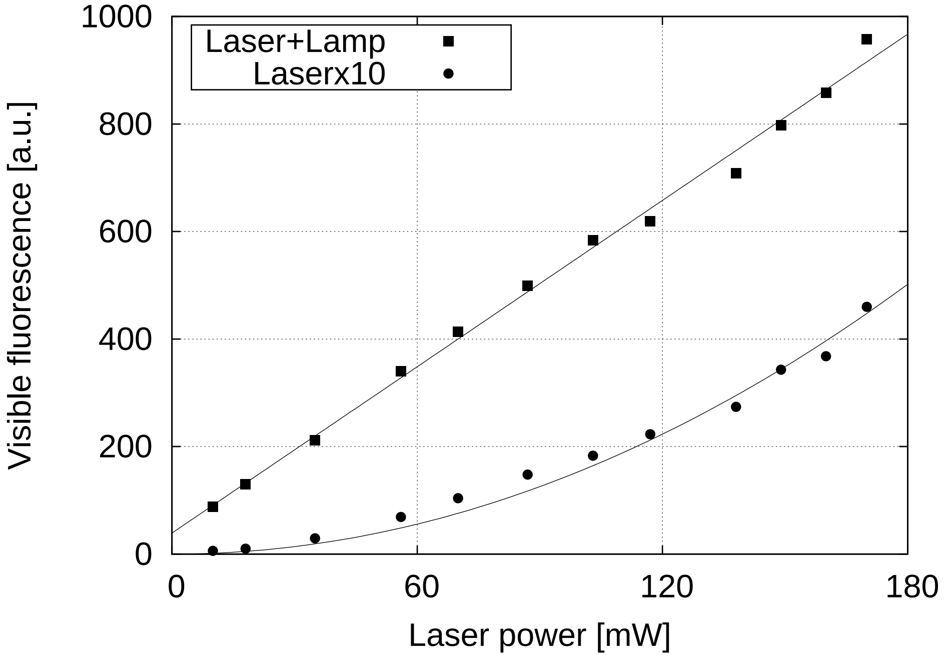

Figure 4.8: Dependence of the PMT signal and noise (LDR) on the laser intensity for the Er:KYF crystal.

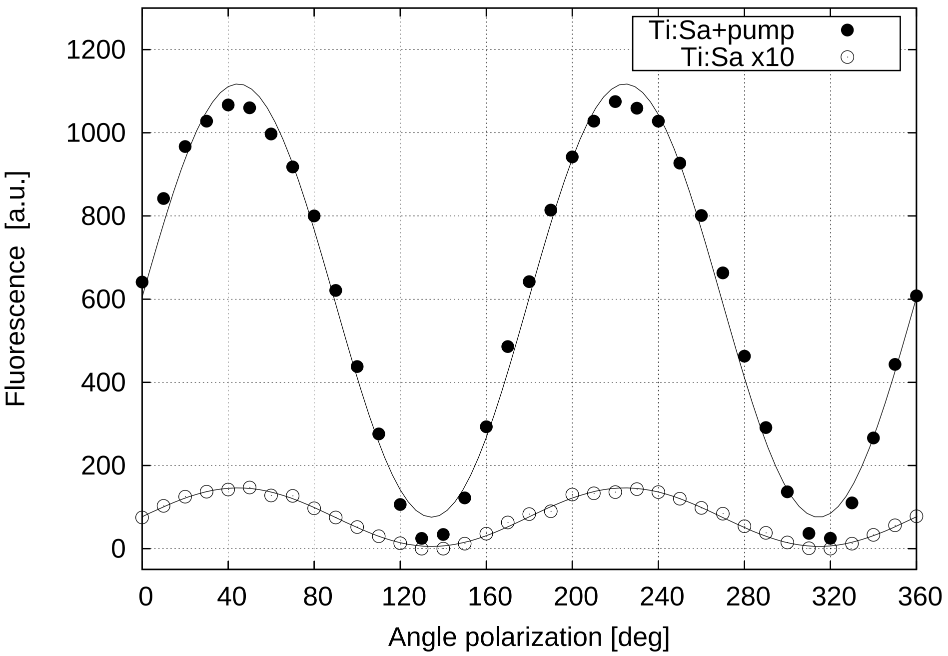

Figure 4.9: Dependence of the PMT signal and noise (LDR) on the laser polarization orientation for the Er:YLF crystal

4.3. Model validation

In the previuos section we have presented results that follow the proposed model. However, we now perform measurements on Er:YLF without the source showing that the Stokes process is responsible for LDR.

The population of the $^4I_{13/2}$ due to the Ti:Sa laser (II) as a function of the laser wavelength and with the intensity set to 100 mW is studied by measuring the infrared fluorescence of this level with the InGaAs(II) PD coupled with the FEL1500 longpass filter. Its use and the responsivity of the PD ensure that only the fluorescence from $^4I_{13/2}$ can be detected. The amplified output of the PD is measured by a voltmeter. The results, plotted in Fig. (4.10), follows Eq. (1.39) where the Antistokes process can be neglected just off resonance. These measurements are similar to those performed in absorption by Auzel Fig. (1.7) at room temperature for a similar sample. The infrared fluorescence decreases exponentially with the energy difference between the laser and the next lower manifold.

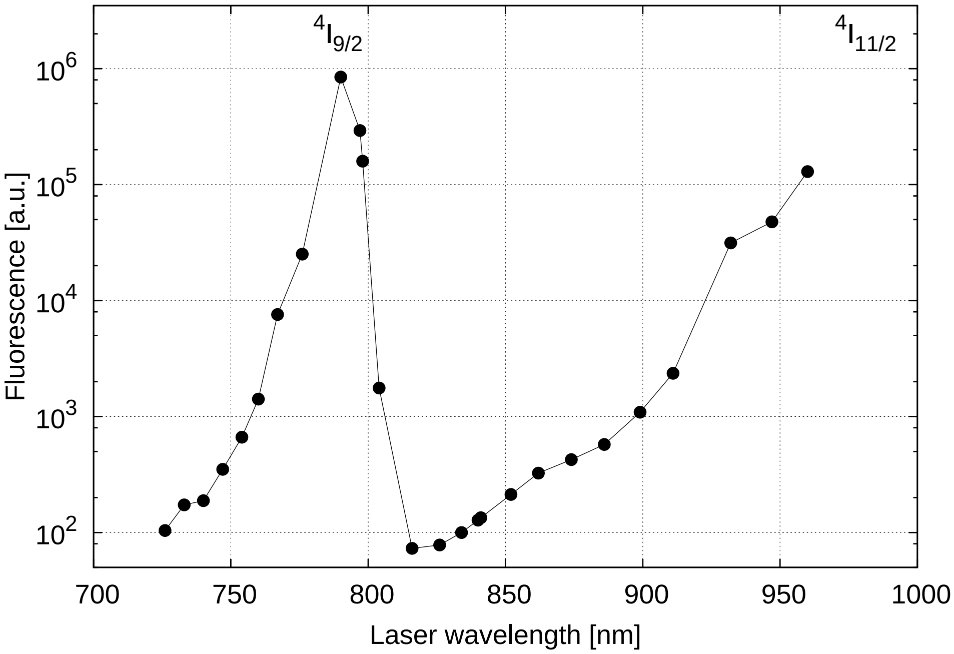

Figure 4.10: Dependence of the multiphonon side band absorption on laser wavelength in Er:YLF. The position of the energy of the manifolds is shown.

We can prove that the population of the $^4I_{13/2}$ manifold is due to the relaxation from the $^4I_{11/2}$ one by pulsing the laser beam with a chopper[10]. The Ti:Sa is tuned to the resonance at 840.565 nm with an intensity of 540 mW. The fluorescence of the $^4S_{3/2}$ is measured with the PMT coupled with the filter FB540-40. The LDR can occur only if the level $^4I_{13/2,1/2}$ is populated and simultaneoulsy the laser beam is shone on the the crystal. If the laser pulses are short enough and if their repetition rate is slow enough, then almost all ions excited by one laser pulse in to $^4I_{13/2}$ have already relaxed to the ground state before the

---

[10] It is a rotating metal disk with a slit that are larger than the beam size.

arrival of the next pulse. During each pulse only a small fraction of the ions excited into $^4\mathrm{I}_{11/2}$ by the laser relaxes to $^4\mathrm{I}_{13/2}$. Hence, the slower the pulse repetition rate and the shorter their duration, the smaller is the LDR strength. As the lifetimes of the $^4\mathrm{I}_{11/2}$ and of the $^4\mathrm{I}_{13/2}$ manifolds are of few milliseconds in YLF, this effect can be already important with a rate of few Hz and laser pulse of few milliseconds. In Fig. (4.11), the time evolution of the LDR is plotted with and without the chopper. Compared to the continuous mode, at 4 Hz and at 10 Hz the LDR is reduced by a factor equal to about 6 and 400. This interesting measurement is currently under investigation.

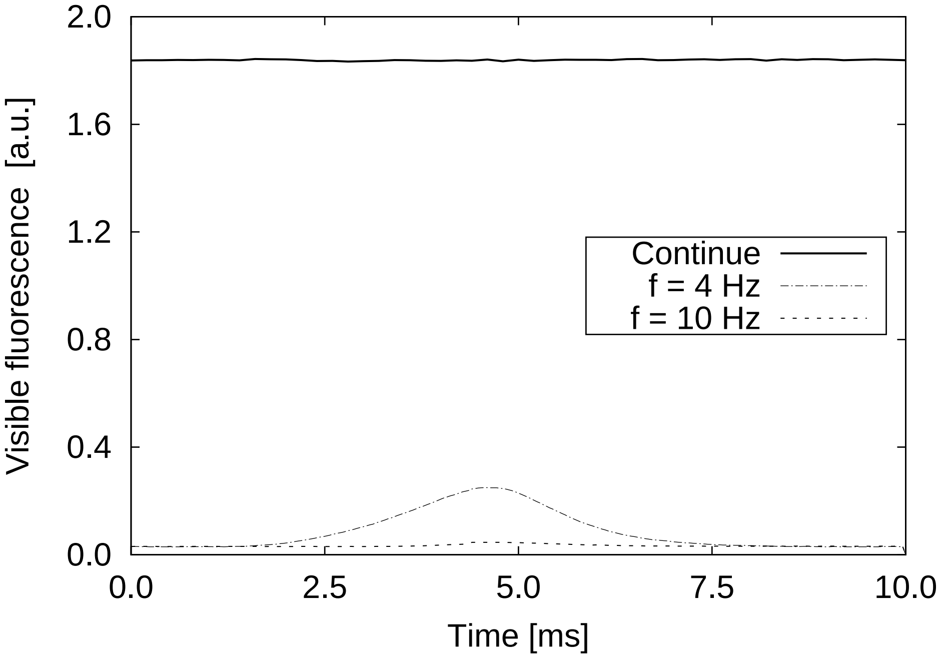

Figure 4.11: Time evolution of the PMT signal for different repetition rates of the laser pulses.

4.4. Er:YLF upconversion efficiency

It is important for the realization of the detector to achieve a high UP efficiency but, as we seen before and in Eq. (2.7), the noise increases with the laser intensity. In order to estimate the efficiency we have repeated the measurements of the visible fluorescence induced by the infrared source as function of laser intensity using the Avesta Ti:Sa. It delivers up to 750 mW at 840.565 nm. We can also achieve an intensity equal to about 60 W/cm^2 focusing the beam to 1.3 mm of diameter. According to Eq. (2.7)[11], tha data are fitted to the following function

$$f(I) = a\eta_{up}(I) = a\left[\frac{\beta_{40}}{\beta_{41}}\left(\frac{1+bI}{\beta_{41}} - 1\right)^{-1}\right] \tag{4.1}$$

---

[11] actually this formula is obtained considering an uniform laser intensity, whereas the laser profile is gaussian. This should be led to an understimation of the efficiency

with a and b adjustable parameters. Here, β_{40}, β_{41} are fixed to 0.28 and 0.67 [61][12], I is the laser intensity. In particular, we get

$$b = \frac{\sigma_{14}\tau_1}{h\nu} \tag{4.2}$$

from which it is possible to estimate the absorption cross section: $\sigma_{14} \approx 4 \cdot 10^{-19}\,\mathrm{cm}^2$, consistent with the value obtained in literature [].

From the estimated parameter b, the effective upconversion efficiency η_{up} is computed as function of laser intensity and is plotted in Fig. (**??**)

For example, with an laser intensity of $10\,\mathrm{W/cm^2}$, $\eta_{up=40\,\%}$ is obtained, i.e., 40% of the ions excited by the source have been converted into visible photons at 540 nm, instead to fluoresce at about 1600 nm.

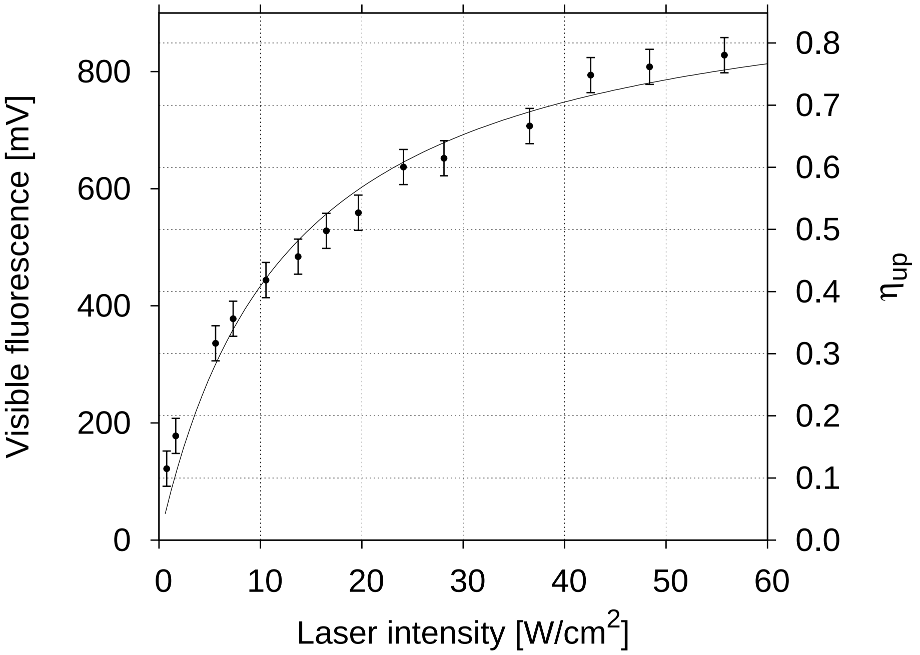

Figure 4.12:

4.5. Other energy level schemes

The S/N is observed also in other UP energy level schemes of Erbium doped KYF. UP is provided by the Dye laser tuned on the level $^4I_{11/2,1/2}$ and on one level of $^4G_{9/2}$ at 579.094 nm. The filter FEL1500 that selects the source fluorescence is replaced with the filter FEL1000 in order to allow the source to excite the manifold $^4I_{11/2}$. Once $^4G_{9/2}$ is populated, it quickly relaxes to the $^4S_{3/2,3/2}$ level. Then, the fluorescence at 540 nm is collected by the PMT. However, two filters, FB540-40 and FGB67, are mounted in front of the PMT because the scattered laser light causes its saturation. In fact, fa ew mV offset

---

[12] Confirming the good assumption that $\beta_{40} + \beta_{41} \approx 1$ used to obtain the formula

affects the measurements Fig. (4.13). The S/N is not comparable with the others obtained for the different source intensity excitations, but the noise is again too high in order to detect the small gamma source.

4.6. Other rare earths

Besides the Erbium measurements campaign, other RE ions havesimilarly been studied. It has been chosen an energy level scheme in which the laser photon is separated from the next lower manifold by an energy bridged by al least three phonons. The energy level of the different RE^{3+} level are shown in Fig. (4.13).

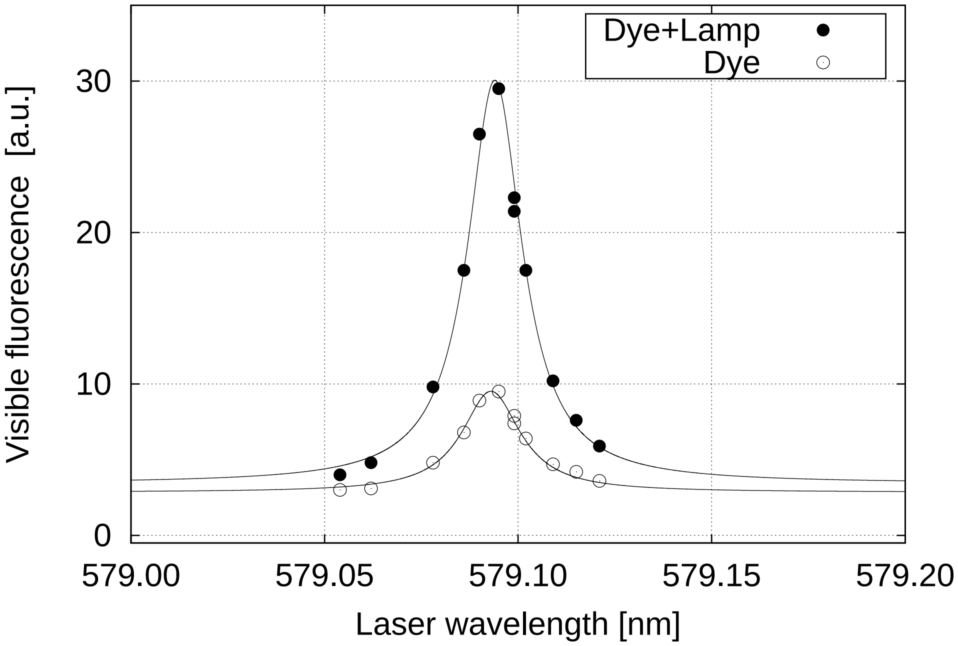

Figure 4.13: Dependence of the PMT output and noise (LDR) on the dye laser wavelength for Er:KYF crystal.

4.6.1 Ho:YLF 0.8%

The source excites the Ho^{3+} ion in the first excited state $^5I_7$ whose lifetime is about 17 ms. Then the Dye laser promotes these ions to $^5G_5$ or $^1F_5$ manifold, that relax to $^5S_2$. It emits at about 545 nm and the fluorescence is selectively collected by the PMT. The fits provide two Lorentian functions centered at 585.789 nm with a FWMH of about 15 pm. However the noise is again too large.

4.6.2 Dy:BYF 0.65%

Dy:BYF has a very interesting energy level scheme. The first excited manifold $^6H_{13/2}$, located at around 3500 cm^{-1} has a lifetime of 6 ms at 10 K [63] and the Dye laser is tuned between the lowest level of this manifold and that of the $^4F_{9/2}$ manifold. The laser photon is separated in energy from the next lower manifold by 4100 cm^{-1}, corresponding to about eleven effective phonon energies. Hence, we expect a very low noise due to Stokes process. The emission $^4F_{9/2} \rightarrow^6 H_{15/2}$ at 482 nm is expected as a consequence of the source induced population of the $^6H_{13/2}$ imanifold and is selectevely collected by the PMT.

Nevertheless, no fluorescence output is observed with or without the lamp, searching the resonance between 575 and 585 nm with a laser intensity of 100 mW. The resonance is found around 576.4 nm by populating the $^6H_{13/2}$ manifold using the cw Avesta Ti:Sa laser with 100 mW at about 810 nm. The $^6F_{5/2}$ manifold is directly populated and then relaxes to the$^6H_{13/2}$manifold with the assistance of phonons. Hence, we have supposed that a very low absorption cross section characterizes the transition $^6H_{13/2} \rightarrow^4 F_{9/2}$.

4.6.3 Yb:YAG 10%

The $4f$ energy level structure of Yb^{3+} is consists of only two manifolds. They are separated in energy by about 10250 cm^{-1}. The more energetic $^2F_{5/2}$ has a lifetime of about 1 ms. It is found that a CT cross section at around 265 nm from this manifold is equal to $1.1 \cdot 10^{-18}$ cm^{-1} [32].

At low temperature, about 10% of the Yb^{2+} ions radiatively relax to the excited state of Yb^{3+} by emitting photon at 330 nm or 465 nm. The remaining ions relax by releasing a high number of phonons [64]. A recycling process, as described in Sec. (2.2), can be also applied for the realization of the detector. In addition, a high number of ions excited by X-ray into the $^2F_{5/2}$ manifold has been already proved [44].

The crystal is cooled down to 10 K and is excited with a laser diode at a wavelength between 255 and 265 nm with intensity of 1 mW, thereby providing the upconversion of the first excited manifold. However, a saturation of the PMT occurs though the longpass filter FGL400 and FGL450 screen the PMT by the UV diode excitation. We plan to repeat these measurements with a suitable notch filters and also with Yb doped different matrix.

Table 4.1: Lorentzian fit parameters

Crystal	**Transition**	**Laser+source**		**Laser**		**S/N**
		Center [nm]	**FWMH** [pm]	**Center** [nm]	**FWMH** [pm]	
Er:YAG	$^4I_{13/2,1/2}\rightarrow ^4S_{3/2,3/2}$	839.648	39	839.647	65	13.1
Er:KYF	$^4I_{13/2,1/2}\rightarrow ^4S_{3/2,1/2}$	833.977	97	833.978	92	47.4
	$^4I_{11/2,1/2}\rightarrow ^4G_{9/2,???}$	579.094	17	579.093	18	4.0
Er:YLF	$^4I_{13/2,1/2}\rightarrow ^4S_{3/2,1/2}$	836.709	16	-	-	-
	$^4I_{13/2,1/2}\rightarrow ^4S_{3/2,3/2}$	840.565	4	840.565	4	≈ 300

Conclusions

We have developed an experimental technique in order to efficiently investigate many different Re doped crystals with the goal of the realization of a IRQC based detector for low-threshold particle detection.

We have developed a theoretical model in order to describe the physics at the basis of such a detector scheme and we have carried out the measurements necessary to validate the model.

In particular, we can estimate with good accuracy the number of ions excited by the particle per energy unit into the different radiative states in the range energy between 0.25 and 6 eV.

As a second step, the different upconversion energy level schemes and their efficiency at a temperature of 10 K can be tested. Finally the crystal as active medium of the IRQC based detector can be investigated with a small gamma source.

We have demonstrated the feasibility of the detection process but we have not managed to reduce enough the noise in order to build a real detector, yet.

The performed measurements allow us to define some important characteristics on the basis of which it is possible to identify the optimum crystal as detector active medium. A low energy phonon host matrix ensures low multiphonon relaxation rate, increasing the effective level lifetimes and limiting the Stokes and Antistokes processes. The last two can also be reduced by choosing suitable RE energy level schemes. In addition, high excited state absorption cross sections are required to obtain high upconversion efficiency and low noise with low laser intensity.

Ce:LaBr$_3$ satisfies this requirements. In particular, it has only two $4f$ manifold, separated in energy by only about 2000 cm^{-1}. No lifetime measurements have been performed, to our knowledge, on this excited state but it is reasonable that its lifetimes at low temperature can reach even tens of ms. The upconversion towards the $5d$ levels ensures a large excited state absorption cross section. Furthermore, Ce:LaBr$_3$ itself is a good scintillator, as mentioned in Sec. (1.5.1), and the upconversion process, involving a recycle mechanism as described in Sec. (2.2), can improve its features. We plan to investigate this crystal in the next future.

With this technique, we are also planning to investigate the involment of the photon avalanche upconversion in the detection process in crystal such as Pr:LaCl$_3$ and Nd:KPB.

Acknowledgments

I wish to thank Prof. M. Tonelli of the Physics Department of the University of Pisa for its kind collaboration within the AXIOMA project. I also wish to express my warmest gratitude to all people of the research group in which I have been working for my thesis. A particular thanks is due to my colleague and friend Marco Guarise.

Bibliography

[1] B. G. Wybourne. *Spectroscopic properties of rare earths.* Interscience, New York, 1965.

[2] G. Liu and B. Jacquier. *Spectroscopic properties of rare earths in optical materials*, volume 83. Springer Science & Business Media, New York, 2006.

[3] S. Hufner. *Optical spectra of transparent rare earth compounds.* Elsevier, Amsterdam, 2012.

[4] B. H. Bransden and C. J. Joachain. *Physics of Atoms and Molecules.* Pearson, Noida (India), 2006.

[5] B. G. Wybourne and L. Smentek. *Optical spectroscopy of lanthanides: magnetic and hyperfine interactions.* CRC, Boca Raton, 2007.

[6] Martin J Klein. On a degeneracy theorem of kramers. *American Journal of Physics*, 20(2):65–71, 1952.

[7] W. T. Carnall, G. L. Goodman, K. Rajnak, and R. S. Rana. A systematic analysis of the spectra of the lanthanides doped into single crystal LaF3. *J. Chem. Phys.*, 90:3443–3457, 1989.

[8] P. S. Peijzel, A. Meijerink, R. T. Wegh, M. F. Reid, and G. W. Burdick. A complete 4fn energy level diagram for all trivalent lanthanide ions. *J. Solid State Chem.*, 178:448–453, 2005.

[9] P. C. de Sousa Filho, J. F. Lima, and O. A. Serra. From Lighting to Photoprotection: Fundamentals and Applications of Rare Earth Materials. *J. Brazil Chem. Soc.*, 26:2471–2495, 2015.

[10] P. Dorenbos. The 5d level positions of the trivalent lanthanides in inorganic compounds. *J. Lumin.*, 91:155–176, 2000.

[11] O. Svelto. *Principles of Lasers.* Springer, New York, 2010.

[12] D. E. McCumber and M. D. Sturge. Linewidth and temperature shift of the R lines in ruby. *J. Appl. Phys.*, 34:1682–1684, 1963.

[13] Mathijs de Jong, Luis Seijo, Andries Meijerinka, and Freddy T Rabouwa. Relation between stokes shift and huang-rhys parameter. *Phys. Chem. Chem. Phys.*, 17:16959–16969, 2015.

[14] J. Solé, L. Bausa, and D. Jaque. *An introduction to the optical spectroscopy of inorganic solids.* Wiley, New York, 2005.

[15] K. Rademaker. *Rare Earth-Doped Alkali-Lead-Halide Laser Crystals of Low-Phonon Energy.* Cuvillier, Gőttingen, 2005.

[16] BR Judd. Optical absorption intensities of rare-earth ions. *Phys. Rev.*, 127:750, 1962.

[17] G. S. Ofelt. Intensities of crystal spectra of rare-earth ions. *J. Chem. Phys.*, 37:511–520, 1962.

[18] M. Eichhorn. Quasi-three-level solid-state lasers in the near and mid infrared based on trivalent rare earth ions. *Appl. Phys. B*, 93:269–316, 2008.

[19] B. M. Walsh, H. R. Lee, and N. P. Barnes. Mid infrared lasers for remote sensing applications. *J. Lumin.*, 169:400–405, 2016.

[20] T. Miyakawa and D. L. Dexter. Phonon sidebands, multiphonon relaxation of excited states, and phonon-assisted energy transfer between ions in solids. *Phys. Rev. B*, 1:2961, 1970.

[21] F. Auzel. Multiphonon-assisted anti-Stokes and Stokes fluorescence of triply ionized rare-earth ions. *Phys. Rev. B*, 13:2809, 1976.

[22] D. L. Dexter. A theory of sensitized luminescence in solids. *J. Chem. Phys.*, 21:836–850, 1953.

[23] M. Inokuti and F. Hirayama. Influence of energy transfer by the exchange mechanism on donor luminescence. *J. Chem. Phys.*, 43:1978–1989, 1965.

[24] D. A. Zubenko, M. A. Noginov, V. A. Smirnov, and I. A. Shcherbakov. Different mechanisms of nonlinear quenching of luminescence. *Phys. Rev. B*, 55:8881, 1997.

[25] L. D. Zusman. Kinetics of luminescence damping in the hopping mechanism of quenching. *Sov. JETP*, 46:347, 1977.

[26] J. Koetke and G. Huber. Infrared excited-state absorption and stimulated-emission cross sections of Er3+-doped crystals. *Appl. Phys. B*, 61:151–158, 1995.

[27] J. C. Krupa. Optical excitations in lanthanide and actinide compounds. *J. Alloy. Compd.*, 225:1–10, 1995.

[28] J. C. Krupa and M. Queffelec. UV and VUV optical excitations in wide band gap materials doped with rare earth ions: 4f–5d transitions. *J. Alloy. Compd.*, 250:287–292, 1997.

[29] P. Dorenbos. Systematic behaviour in trivalent lanthanide charge transfer energies. *J. Phys.-Condens. Mat.*, 15:8417, 2003.

[30] C. K. Jørgensen. *Modern aspects of ligand field theory.* North-Holland, Amsterdam, 1971.

[31] N. Guerassimova, N. Garnier, C. Dujardin, A. G. Petrosyan, and C. Pedrini. X-ray-excited charge transfer luminescence in YAG: Yb and YbAG. *J. Lumin.*, 94:11–14, 2001.

[32] R. Moncorgé, O. N. Eremeykin, J.-L. Doualan, and O. L. Antipov. Origin of athermal refractive index changes observed in Yb 3+ doped YAG and KGW. *Opt. Commun.*, 281:2526–2530, 2008.

[33] P. Dorenbos. Absolute location of lanthanide energy levels and the performance of phosphors. *J. Lumin.*, 122:315–317, 2007.

[34] F. Auzel and Y. Chen. Photon avalanche luminescence of Er 3+ ions in LiYF 4 crystal. *J. Lumin.*, 65:45–56, 1995.

[35] A. Lempicki. The physics of inorganic scintillators. *J. Appl. Spectrosc.*, 62:787–802, 1995.

[36] K. W. Krãmer, P. Dorenbos, H. U. Gűdel, and C. W. E. Van Eijk. Development and characterization of highly efficient new cerium doped rare earth halide scintillator materials. *J. Mater. Chem.*, 16:2773–2780, 2006.

[37] T. Yanagida. Study of rare-earth-doped scintillators. *Opt. Mater.*, 35:1987–1992, 2013.

[38] N. Bloembergen. Solid state infrared quantum counters. *Phys. Rev. Lett.*, 2:84, 1959.

[39] J. S. Chivian, W. E. Case, and D. D. Eden. The photon avalanche: A new phenomenon in Pr3+-based infrared quantum counters. *Appl. Phys. Lett.*, 35:124–125, 1979.

[40] Fr. Auzel. Upconversion and anti-stokes processes with f and d ions in solids. *Chem. Rev.*, 104:139–174, 2004.

[41] M. F. Joubert, S. Guy, and B. Jacquier. Model of the photon-avalanche effect. *Phys. Rev. B*, 48:10031, 1993.

[42] M.-F. Joubert. Photon avalanche upconversion in rare earth laser materials. *Opt. Mater.*, 11:181–203, 1999.

[43] D. B. Gatch, W. M. Dennis, and W. M. Yen. Infrared detection scheme with the photon avalanche effect. *Appl. Optics*, 42:615–620, 2003.

[44] P. Antonini, S. Belogurov, G. Bressi, G. Carugno, and D. Iannuzzi. Infrared scintillation of Yb (10%): YAG crystal. *Nucl. Instrum. Meth. A*, 486:799–802, 2002.

[45] W. W. Moses, M. J. Weber, S. E. Derenzo, D. Perry, P. Berdahl, and L. A. Boatner. Prospects for dense, infrared emitting scintillators. *IEEE Trans. Nucl. Sci.*, 45:462–466, 1998.

[46] L. Barcellan, E. Berto, G. Carugno, G. Galet, G. Galeazzi, and A. F. Borghesani. A battery-operated, stabilized, high-energy pulsed electron gun for the production of rare gas excimers. *Review of Scientific Instruments*, 82:095103, 2011.

[47] A. F. Borghesani, G. Bressi, G. Carugno, E. Conti, and D. Iannuzzi. Infrared fluorescence of Xe2 molecules in electron/proton beam excited pure Xe gas and in an Ar/Xe gas mixture. *J. Chem. Phys.*, 115:6042–6050, 2001.

[48] J. Dong, A. Rapaport, M. Bass, F. Szipocs, and K. Ueda. Temperature-dependent stimulated emission cross section and concentration quenching in highly doped Nd3+: YAG crystals. *Phys. Status Solidi A*, 202:2565–2573, 2005.

[49] G. E. Venikouas, G. J. Quarles, J. P. King, and R. C. Powell. Spectroscopy of Y 3 Al 5 O 12: Nd 3+ under high-power, picosecond-pulse excitation. *Phys. Rev. B*, 30:2401, 1984.

[50] J. B. Gruber, J. R. Quagliano, M. F. Reid, F. S. Richardson, M. E. Hills, M. D. Seltzer, S. B. Stevens, C. A. Morrison, and T. H. Allik. Energy levels and correlation crystal-field effects in Er 3+-doped garnets. *Phys. Rev. B*, 48:15561, 1993.

[51] H. G. Danielmeyer, M. Blắtte, and P. Balmer. Fluorescence quenching in Nd: YAG. *Appl. Phys.*, 1:269–274, 1973.

[52] K. N. Gulyaeva, A. N. Trofimov, and M. V. Zamoryanskaya. A study of cathodoluminescent characteristics of YAG: Nd3+. *Opt. Spectrosc.*, 114:709–712, 2013.

[53] E. A. Seregina and A. A. Seregin. Radioluminescence of solid neodymium-doped laser materials excited by α-particles and fission fragments. *Quantum Electron.*, 43:150, 2013.

[54] T. Yanagida, K. Kamada, Y. Fujimoto, Y. Yokota, A. Yoshikawa, H. Yagi, and T. Yanagitani. Scintillation properties of transparent ceramic and single crystalline Nd: YAG scintillators. *Nucl. Instrum. Meth. A*, 631:54–57, 2011.

[55] L. Ning, P. A. Tanner, V. V. Harutunyan, E. Aleksanyan, V. N. Makhov, and M. Kirm. Luminescence and excitation spectra of YAG: Nd 3+ excited by synchrotron radiation. *J. Lumin.*, 127:397–403, 2007.

[56] N. Barnes and B. M. Walsh. Quantum efficiency measurements of Nd:YAG, Yb:YAG, and Tm:YAG. In M. Fermann and L. Marshall, editors, *Advanced Solid-State Lasers*, volume 68 of *Trends and Photonics Series*. OSA, New York, 2002.

[57] J. Th. Thomas, M. Tonelli, S. Veronesi, E. Cavalli, X. Mateos, V. Petrov, U. Griebner, J. Li, Y. Pan, and J. Guo. Optical spectroscopy of Tm3+: YAG transparent ceramics. *J. Phys D: Appl. Phys.*, 46(37):375301, 2013.

[58] Winicjusz Drozdowski, Kamil Brylew, Andrzej J Wojtowicz, Jarosław Kisielewski, Marek Świrkowicz, Tadeusz Łukasiewicz, Johan TM de Haas, and Pieter Dorenbos. 33000 photons per mev from mixed (lu 0.75 y 0.25) 3 al 5 o 12: Pr scintillator crystals. *Optical Materials Express*, 4(6):1207–1212, 2014.

[59] A. F. Borghesani, C. Braggio, G. Carugno, F. Chiossi, A. Di Lieto, M. Guarise, G. Ruoso, and M. Tonelli. Particle detection through the quantum counter concept in YAG:Er^{3+}. *Appl. Phys. Lett.*, 107:193501, 2015.

[60] MA Couto Dos Santos, E Antic-Fidancev, JY Gesland, JC Krupa, M Lemaıtre-Blaise, and P Porcher. Absorption and fluorescence of Er 3+-doped LiYF 4: measurements and simulation. *J. Alloy. Compd.*, 275:435–441, 1998.

[61] AM Tkachuk, IK Razumova, AA Mirzaeva, AV Malyshev, and VP Gapontsev. Up-conversion and population of excited erbium levels in LiY1- x ErxF4 (x= 0.003–1) crystals under CW InGaAs laser-diode pumping. *Opt. Spectrosc.*, 92:67–82, 2002.

[62] M Pollnau, Th Graf, JE Balmer, W Lüthy, and HP Weber. Explanation of the cw operation of the er 3+ 3-μm crystal laser. *Physical Review A*, 49(5):3990, 1994.

[63] A Toncelli, M Tonelli, A Cassanho, and HP Jenssen. Spectroscopy and dynamic measurements of a Tm, Dy: BaY 2 F 8 crystal. *J. Lumin.*, 82:291–298, 1999.

[64] L Van Pieterson, M Heeroma, E De Heer, and A Meijerink. Charge transfer luminescence of Yb 3+. *J. Lumin.*, 91:177–193, 2000.

[65] S. R. Hastings-Simon, B. Lauritzen, Matthias U. Staudt, J. L. M. van Mechelen, Ch. Simon, H. De Riedmatten, Mi. Afzelius, and N. Gisin. Zeeman-level lifetimes in er 3+: Y 2 sio 5. *Phys. Rev. B*, 78:085410, 2008.